STUDIES ON SPACE GRADE NANO-IONIC RADIATION SENSORS USING ADDITIVE MANUFACTURING TECHNOLOGY

by

Shah Mohammad Rahmot Ullah

A thesis

submitted in partial fulfillment

of the requirements for the degree of

Master of Science in Electrical and Computer Engineering

Boise State University

August 2020

BOISE STATE UNIVERSITY GRADUATE COLLEGE

DEFENSE COMMITTEE AND FINAL READING APPROVALS

of the thesis submitted by

Shah Mohammad Rahmot Ullah

Thesis Title: Studies on Space Grade Nano-ionic Radiation Sensors Using Additive Manufacturing Technology

Date of Final Oral Examination: 04 June 2020

The following individuals read and discussed the thesis submitted by student Shah Mohammad Rahmot Ullah, and they evaluated their presentation and response to questions during the final oral examination. They found that the student passed the final oral examination.

Maria I. Mitkova, Ph.D.	Chair, Supervisory Committee
Harish Subbaraman, Ph.D.	Member, Supervisory Committee
David Estrada, Ph.D.	Member, Supervisory Committee

The final reading approval of the thesis was granted by Maria I. Mitkova, Ph.D., Chair of the Supervisory Committee. The thesis was approved by the Graduate College.

DEDICATION

To My Wife

ACKNOWLEDGMENTS

This work has been funded by the NASA established program to stimulate the Competitive Research (EPSCoR) project. Grant No. 80NSSC17M0029.

First, I would like to thank my advisor, Dr. Maria Mitkova, for her constant support and for giving me numerous opportunities to gain experience and knowledge working in her research groups. She has repeatedly proven her dedication to our research group and the growth of each of us individually by always making herself available to our needs, sharing her knowledge, and pushing each of us to succeed.

I would like to thank PI Dr. David Estrada for his guidance, motivation, expertise encouragement throughout the project work. I would also like to thank Dr. Harish Subbaraman for taking time to be part of my thesis committee, and for providing his support and knowledge regarding my research work.

To the members of our research group who shared their knowledge, time, and Specially thank my Lab mates Al-Amin Ahmed Simon (Ph.D. Candidate), Layel Jones (MS graduate), Henri Kunold (BS graduate) for their extraordinary support, sharing their knowledge and time.

I would like to thank the University of Michigan for allowing me to use their Xe^{+} ion irradiation facilities to studies of radiation-induced effects in printed Chalcogenide glass.

I would also like to acknowledge advanced nano-materials and manufacturing laboratory (ANML) at Boise State University for ink characterization support and help. I

would also like to acknowledge the Surface Science laboratory at Boise State University and Dr. Paul Davis for assistance in performing AFM. I would also like to acknowledge Dr. Don Plumlee allow me to Ceramic MEMS (C-MEMS) laboratory to perform screen printing and Tyler Webb to train me on that screen-printer. I am grateful to Idaho Microfabrication Laboratory (IML)'s director Mr. Peter Miranda and lab tech support engineer, Mr. Travis Gabel, Boise State Center For Materials Characterization lab's Senior Research Engineer, Dr. Karthik Chinnathambi, SEM/EPMA Research Engineer, Dr. Nick Bulloss, for training me on printers, sintering, and characterization equipment and their tremendous efforts to make this project successful.

To everyone who helped me achieve my goals, your time and efforts are appreciated. Thank you.

ABSTRACT

Though additive manufacturing technology has been developing for 30 years, in recent years, it gets researchers' and industries' attention for new expansion in fabricated electronics devices, especially on a flexible substrate. This technology allows fabricating complex design of electronics devices with multi-functionality. Its application has been significantly expanded to different fields such as sensors and other device prototypes for nuclear facilities, aerospace manufacturing, bio-medical, solar energy, etc. due to its low-cost efficiency and sustainable manufacturing. It has a huge advantage over traditional methods such as lower materials waste during production, avoiding complex etching system and harmful chemicals, simplified assembly system eliminating lithography, etching, and packaging process.

This work is focused on developing a fabrication process of Ge_xSe_{100-x} (x=20, 30, 40) based Chalcogenide glass (ChG) printed space-grade radiation sensing device for NASA space exploration application using additive manufacturing technology. By following this fabrication process, astronauts can fabricate a radiation sensor in the international space station to reduce high transport cost and payload. The function of this radiation sensing device depends on triggered by irradiation Ag^+ ions migration into a Ge-Se based ChG printed films, as a result of which conductivity increases several orders of magnitude. These studied devices were printed on different substrates, including lightweight flexible substrates at room temperature.

The research work presented in this thesis is divided into four major parts; these are: (i) Ge-Se based ChG ink formation, (ii) printing of the ChG ink on the substrate and sintering process, (iii) printed films analysis, and (iv) device fabrication & testing. Although two types of inks were produced, such as dissolution based ChG inks and nanoparticles based ChG inks, this work mainly focuses on the dissolution based ChG inks fabricated devices, because of the complexity of ink formation and the important correlated effects of the interaction of the ChG and solvents.

The inks were characterized by different methods such as tensiometer measurement of the contact angle of ink with the substrate, the dynamic light scattering (DLS) to check the particles' size, and viscometer to measure the viscosity of inks. The inks can be modified for use in different types of printers by varying their viscosity, particle size, and solvents. Different kinds of printing methods were used for printing on the substrates with ChG inks, such as screen printing and inkjet printing. The printer's parameters were optimized for obtaining a good printing pattern. The sintering process also was optimized to evaporate solvents and create a solid film. The effects of different UV light radiation doses and Xe^{+} irradiation on the ChG printed film devices were studied and analyzed in order to give proof of concept of the printed radiation sensor operation. Different kinds of materials and structural characterization methods such as energy dispersive x-ray spectroscopy (EDS), scanning electron microscopy (SEM), atomic force microscopy (AFM), x-ray diffraction spectroscopy (XRD) and Raman spectroscopy have been used to study and analyze the printed ChG compositions, and verify the occurrence of oxidation, topography, surface roughness and structural changes at different radiation doses. These studies help to understand the origin of printed

materials characteristics, which is a vital part of establishing a bridge between materials' parameters and device performance. The last part of this work is fabrication of the radiation sensing devices and their testing under different irradiation doses. The ChG printed radiation sensing devices based on all studied compositions and applied solvents were tested using a semiconductor parameter analyzer and probe station. The conductivity change results were presented as a function of radiation doses. The radiation-induced Ag diffusion process was studied to identify the perfect working device. The Ag diffusion was investigated by EDS and XRD spectroscopy to determine the Ag diffusion by-products forming, their crystal sizes, and compositional changes of the hosting ChG after Ag diffusion. Reversible dissolution based screen printed devices were also fabricated and tested using the same conditions. Along with that, these devices have also been tested under different energy of Xe^{+} ions irradiation. All the results of dissolution based inks and devices, including ink characterizations, printed film analysis, and device performance were compared with the nanoparticles based inks and devices. The performance of devices strongly depends on the composition of ChG.

TABLE OF CONTENTS

LIST OF TABLES

LIST OF FIGURES

LIST OF ABBREVIATIONS

ChG	Chalcogenide Glass
DLS	Dynamic Light Scattering
UV	Ultra violate
EDS	Energy Dispersive X-ray Spectroscopy
SEM	Scanning Electron Microscopy
AFM	Atomic Force Microscopy
XRD	X-ray Power Diffraction
PLD	Pulsed Laser Deposition
CVD	Chemical Vapor Deposition
AM	Additive Manufacturing
CAD	Computer-Aided Design
CRN	Continuous Random Networks
CB	Conduction Band
VB	Valance Band
ES	Edge-Shared
IR	Infra-Ray
EDA	Ethylenediamine
BA	n-Butylamine
PA	n-Propylamine
QC	Quantum Cascade

RFID	Radio Frequency Identification
IML	Idaho Micro-fabrication Lab
EC	Ethyl-cellulose
DOD	Drop-on-Demand
FESEM	Field Emission Scanning Electron Microscope
PSPD	Position-Sensitive Photo-detec

CHAPTER 1: INTRODUCTION

Research Motivation

In modern technology, amorphous materials like the Chalcogenide Glasses (ChG) play a vital role in fabricating numerous types of devices such as gas sensors, temperature sensors, chemical sensors, infrared detectors, radiation sensors, non-volatile memory, solar cells, etc. [1-9]. These devices are widely used in different fields, including semiconductor industry, biomedical, military, nuclear facilities, etc. [1-9]. The function of some of these devices is based on Ag diffusion in ChG, which is one of the most significant effects that can change the conductivity of ChG films [3-8].

Previous studies reported that ChG thin films could be fabricated by different deposition methods like sputtering, pulsed laser deposition (PLD), chemical vapor deposition (CVD), and thermal evaporation for a variety of applications, including the radiation sensor [1-9]. These processes associated with high energy, high vacuum, high temperature, include a high cost. They also require heavy equipment, which makes these processes inapplicable in space missions. Here, the additive manufacturing (AM) technology would be an alternative film deposition method. AM is a process by which materials can be deposited on the substrate by printing layer upon layer very precisely by following the computer-aided design (CAD) file. One option of the AM technology is screen printing, which requires a screen for transferring the desired printed pattern instead of the CAD file.

The AM or printing technology allows depositing materials on a lightweight substrate at room temperature, normal pressure even at zero gravity. Nowadays, the National Aeronautics and Space Administration (NASA) progresses to AM technology innovation of nanomaterial-based sensors for future space exploration [10]. This initiative will open a low-cost path, low waste, as well as large scale manufacturing for the fabrication of the necessary sensors and other devices in the space. Until now, there is no literature about the printing of ChG films and the fabrication of radiation sensing devices with this technology. There is some literature about a solution based ChG film deposition technique like spin coating for preparation of ChG thin films [11-17]. This method, however, does not allow the formation of devices with specific dimensions without application of expensive and robust in shape and weight photolithography systems. To solve this problem, we developed two types of inks, such as dissolution based inks and nanoparticles based inks, which made possible the fabrication of different kind of devices using the AM technology. It is possible to modify the ink parameters so that they can fit the particular printer requirements and print any types of printed patterns. Our proposed fabrication method needs a very small area and simple set up. In this thesis, we describe the formation of dissolution based ChG inks and nanoparticles inks and the fabrication process of radiation sensing devices with these inks using the AM technology and compare and analyze both types of ink fabricated device performance. The Ge-Se based ChGs were used to fabricate the radiation sensing devices because, from previous studies, it was found out that Ag has high diffusivity in them; they have a very wide glass-forming region and high-temperature stability [3].

The results presented in this thesis will open a new research area about printed ChG thin films and their application for different kinds of device fabrication, such as non-volatile memory devices, temperature sensors, gas sensors, and others. With this work, we will be able to answer many existing questions about the application of additive technologies for device fabrication.

Research Objectives

The purpose of this research work is to fabricate space-grade printed radiation sensing devices. A detailed investigation focuses on various compositions of Ge-Se based ChG ink formulation, printing with ChG inks & sintering, printed film analysis, and fabrication of the printed radiation sensors and their testing and analysis under different doses of radiation. This thesis work aims to:

- Describe the formulation of different compositions of Ge-Se based ChG ink & the characterization results of the ink.
- Explain the printing process with these ChG inks on a variety of substrates.
- Interpret the effect of various doses of UV light, as well as Xe^{+} ions-irradiation on the studied compositions of printed ChG films.
- Design the fabrication process of the printed radiation sensing devices.
- Test diverse compositions of the ChG printed radiation sensing devices to analyze and identify the best composition for the desired radiation sensing devices.
- Define how the reversible printed ChG radiation sensing devices work.
- Analyze and compare the performance of the dissolution based printed film devices with nanoparticles based printed film devices.

In the next chapter, the basic properties of ChG, the applications of ChG, the Ag diffusion mechanism in ChG, and the dissolution mechanism of the Ge-Se based ChG in Amine will be discussed. The ink formulation process, the characterization results, printing on a substrate, and the sintering process are described in chapter 3. In chapter 4, the effect of different radiation doses on a variety of compositions of the ChG printed films is presented. These results are used as a reference to correlate the efficacy of the printed devices. The test results of the dissolution based printed devices under different radiation doses are presented in chapter 5. The comparison of both types of printed devices and the performance of the reversible printed devices are also shown at the end of chapter 5. Finally, a summary and some remarks about future works are presented.

CHAPTER 2: CHALCOGENIDE GLASSES

Chalcogenide Glasses

The word "Chalcogen" comes from the Greek word "*khalkós genēs"* where "*khalkós"* stands for Copper and "*genēs"* stands for born or produced. In 1932 Wilhelm Blitz, a German chemist from the University of Hannover and his colleague Werner Fisher named the group 16 of the Periodic Table as the 'chalcogen' [18].

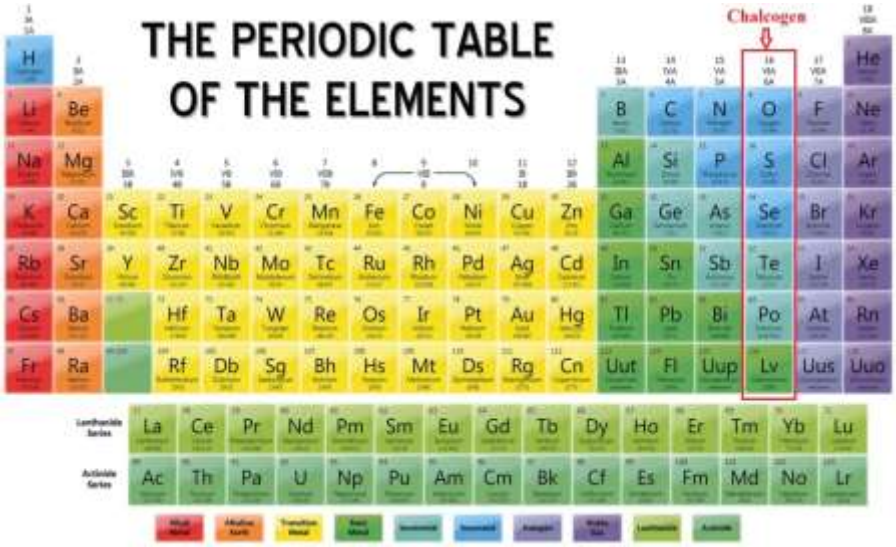

Figure 2.1 Group 16 in the Periodic Table [19].

The chalcogen elements of group 16 of the Periodic Table are Oxygen (O), Sulfur (S), Selenium (Se), and Tellurium (Te) and the radioactive element Polonium (Po). An increase in the atomic number of the elements of this group leads to a metallic character in their chemical interaction.

Thereby, Oxygen (atomic number 8) and Sulfur (atomic number 16) are considered as non-metals. Here, Oxygen is gas, and it has a wider bandgap, which

contributes to very dissimilar optical and electrical properties compared to the other elements of this group. Selenium and Tellurium (both are semiconductors) are known as metalloids, a mixture of metals and non-metals. Their physical and chemical properties are intermediate in nature; they have a metallic appearance and conduct electricity [20]. But chemically, they behave like non-metals. These elements are perfect for forming glass. Polonium is a metal with high radioactive properties. It cannot form glass.

All Chalcogens have similar patterns in electron configuration, especially in the outermost shells, where they all have the same number of valence electrons, resulting in similar trends in chemical behavior:

Table 2.1 Electron Configuration of the Chalcogens [3]

Atomic Number	Element	Number of electrons
8	Oxygen (O)	$1s^2$, $2s^2$,$2p^4$
16	Sulfur (S)	$1s^2$, $2s^2$, $2p^6$, $3s^2$, $3p^4$
34	Selenium (Se)	$1s^2$, $2s^2$, $2p^6$, $3s^2$, $3p^6$, $3d^{10}$, $4s^2$,$4p^4$
52	Tellurium (Te)	$1s^2$, $2s^2$, $2p^6$, $3s^2$, $3p^6$, $3d^{10}$, $4s^2$, $4p^6$,$4d^{10}$, $5s^2$, $5p^4$
84	Polonium (Po)	$1s^2$, $2s^2$, $2p^6$, $3s^2$, $3p^6$, $3d^{10}$, $4s^2$, $4p^6$, $4d^{10}$, $5s^2$, $5p^6$, $5d^{10}$, $6s^2$,$6p^4$

From this electron configuration, it is clear that the Tellurium atom is bigger in size than Selenium and Sulfur. In terms of bond strength, Sulfur has a greater bond strength than Selenium and Tellurium.

Bond strength: Sulfur > Selenium > Tellurium

Atom size : Tellurium > Selenium > Sulfur

The electron configuration of the Chalcogen atoms shows that their outermost shells contain two electrons in the *s* shell and four in the *p* shell. The *s* shells are usually distributed in the depth of the electron cloud of the elements, and they do not participate in a chemical bonding. Regarding the *p* shell electrons, two of them participate in a covalent bonding of the Chalcogen elements with other elements, and the other two form a pair among themselves, the so-called lone pair. The outer shell electrons of the *p* shell of the Chalcogen atoms are significant for their electrical and optical performance.

Chalcogenide glasses contain one or more Chalcogens-S, Se, or Te. In addition, these glasses can contain elements from group IVA and VA, especially Germanium (Ge), Tin (Sn), Antimony (Sb), and Arsenic (As)[21]. These glasses can be binary, or poly-component and form covalently bonded continuous random networks (CRN). It is possible to create a variety of ChG compositions, in which the valence requirements of the elements are obeyed, but their long-range order is not satisfied. Each composition has some specific applications which depend on their electron structure and bonding between the elements.

In comparison with crystalline material, the ChGs have unique electrical and optical properties due to their disordered structure. In crystalline materials, there are two energy states or bands known as the conduction band (CB) and the valence band (VB). Electrons can move from one state to another state by acquiring or releasing sufficient energy. For example, electrons from the VB need higher energy to overcome the bandgap and occupy the CB energy state.

The Chalcogenide glasses have extra energy states called the band tail states, which are localized between the VB and CB. The localized states exist in the ChG because of the presence of the lone pair electrons [22-24]. Electrons from VB can occupy these energy states on their path towards the CB [25]. The electrons in such state can interact with photons during the photo-diffusion.

Materials change their state with changes of entropy, as well as with structural order. According to the structural order, solid materials are divided into three groups - single crystalline, polycrystalline, and amorphous. A single crystalline solid has a regular long-range order of two- or three-dimensional organization of their atoms or molecules, which are held together and repeated periodically throughout the entire solid area, such as a single crystalline Si lattice. Following this, polycrystalline solids consist of multiple different types of single-crystalline areas. The structure of amorphous materials is characterized by short-range order, in which the valence requirements of all participating elements are satisfied, but there is not a long-range order among them. The three chalcogen elements forming the ChG (S, Se, and Te) have quite similar structural organization. Examples of these structural organizations are shown in Figure 2.2.

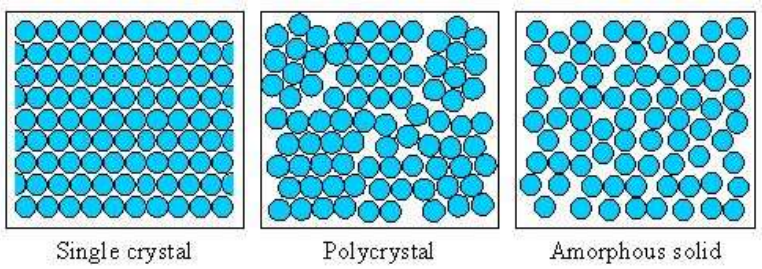

Figure 2.2 Different structural order of solid [26].

If the ChG contains S, each S atom is sharing two of its *p* electrons with other Sulfur atoms, and so a chain is created. In many cases, instead of an open chain, the S

atoms form rings with two configurations in terms of the S atoms location, which are eclipsed (cis) and staggered (trans) [27]. Crystalline Sulfur forms orthorhombic chain-rings with eight elements in it. This orthorhombic chain forms the trans configuration, and the angle between the bonded S atoms is 105°, as shown in figure 2.3. The S_8 molecule is stable and exists in all three physical states. Sulfur-containing glass is different from Se and Te containing glass because Sulfur has significantly higher partial pressure, and Sulfur can phase-separate from the main glass composition due to the formation of the ring structures.

Similar to S, the Se atoms, building the ChG is sharing two of their *p* electrons with the other Se atoms and create a hexagonal chain in which the atoms are connected by covalent bonding. The bond angle of these chains is approximately103.1°. The hexagonal chains are held together by Van der Waals forces [28-29]. An example of such chain is shown in figure 2.4.

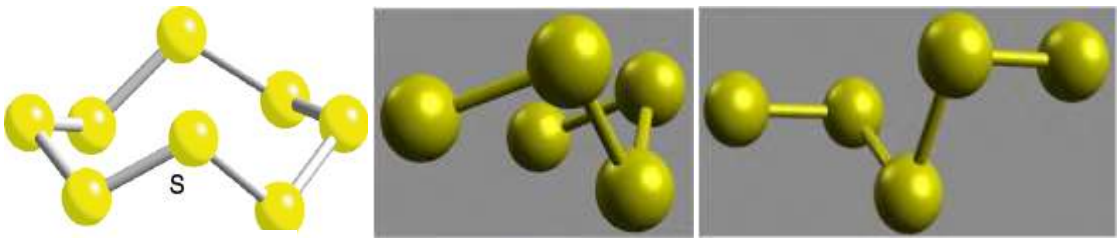

(a) **(b)**

Figure 2.3 Sulfur atoms within a Sulfur ring a) cis and b) trans [28]

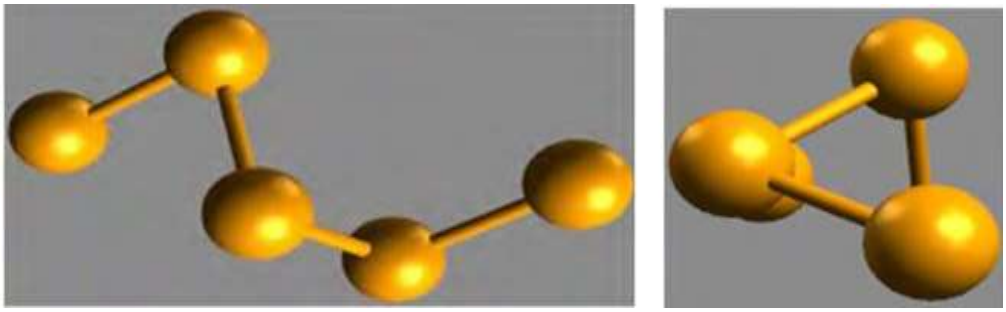

(a) **(b)**

Figure 2.4 Hexagonal Selenium chains a) configuration of the chains and b) top view of the chains [29].

Te also forms long spiraling hexagonal chains connected by Van der Waals forces as Se does. Te has a narrow bandgap, a high conductivity like a metal, and for this reason, it is known as a semi-metal [29].

Structure of the Chalcogenide Glasses

Arsenic and Germanium containing ChG have unique properties. When they are irradiated with the UV light or gamma radiation, electron-hole pairs form, which usually recombines rapidly due to the proximity of a high number of charged defects in the glass, and the material keeps its properties. Because of this, the ChG is considered radiation-hard [30].

When Ge is participating in the formation of a ChG, due to the sp^3 hybridization, it is four-fold coordinated with four equally long covalent bonds formed by its outer shell electrons of the *s* and *p* shell, which are distributed under an angle of 105°.

In a tetrahedral structure, Ge is situated at the center of the unit structure and surrounded by four Chalcogen atoms, as presented in Figure 2.5.

(a) **(b)**

Figure 2.5 Basic structural unit, a) bonding between Ge and Chalcogenide atom, and b) single tetrahedral unit [3].

The tetrahedral shape structures connect with each other in three ways. They can connect with their corners, forming the corner-sharing (CS) structure shown in Figure 2.6.

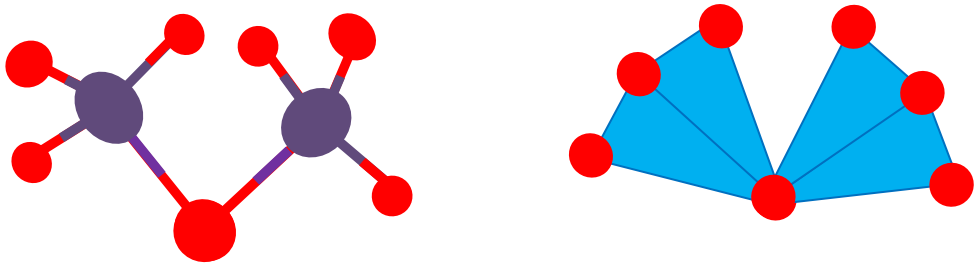

(a) **(b)**

Figure 2.6 a) Bonding between Ge and Chalcogenide atom in the corner-sharing, b) corner-shared tetrahedrals [3].

Another way of connection between the tetrahedral structures is by sharing a common edge. This structure is known as an edge-shared (ES) structure [3,30]. If there is a lack of chalcogenide atoms in the current vicinity to form four heteropolar bonds, then the edge-shared structure will be formed. Since this structural unit requires only six chalcogenide atoms, i.e., one atom less than the corner-sharing structure – Figure 2.7.

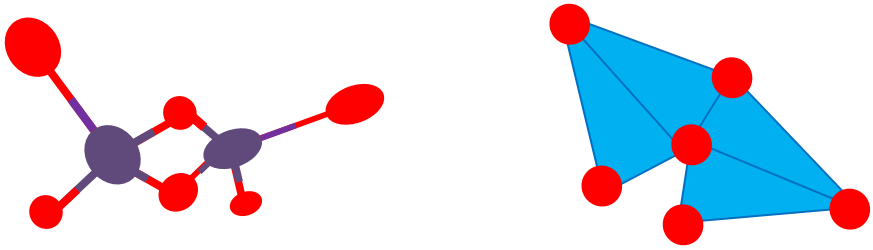

(a) **(b)**

Figure 2.7 a) Bonding between Ge and Chalcogenide atom in edge-sharing structure, b) edge-shared tetrahedrals [3].

In very Ge rich glasses, when the concentration of Ge atoms is more than 30 at.% formation of the so-called ethane-like structure is possible in which a bond between two Ge atoms, belonging to two neighboring tetrahedral structure occurs – Figure 2.8 [3].

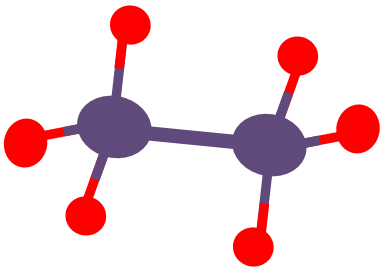

Figure 2.8 Bonding between Ge and Chalcogenide atom in the Ethane-like bonding [3].

Silver Diffusion Mechanism in the Chalcogenide Glass

More than 70 years ago, Kostyshin et al. revealed a new effect of Ag photodiffusion into the ChG field of amorphous semiconductor properties [31]. In essence, the photodiffusion process follows the laws governing each diffusion process, i.e., it occurs when there is a concentration gradient and develops as long as this gradient exists, and the material in which the diffused atoms are introduced is saturated with them.

Due to the interaction of light with the ChG, the amount of introduced Ag atoms in the ChG is higher, and the rate of this reaction is higher compared to the common diffusion process. This changes the optical, electrical, and mechanical properties of the ChG, which leads to various applications like sensors, batteries, optical recordings, and memory devices [31-35]. In general, the diffusion occurs in steps, saturating the host material with Ag. From figure 2.9, it can be seen that for 80 min and 100 min of exposure, there is a sudden change in the Ag diffusion profile. There are three significant stages of Silver diffusion into ChG [36]. It starts with an induction period, followed by effective photo-dissolution, and finishing with an exhaustion process.

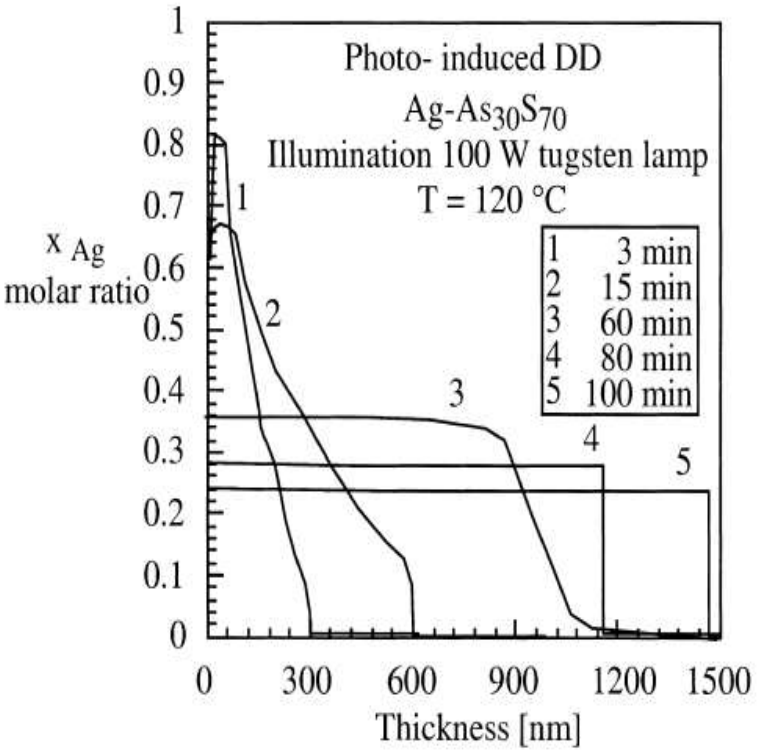

Figure 2.9 Step-like diffusion profile of Ag in $As_{30}S_{70}$[37].

There is a low Ag diffusion rate in the induction period, and the highest diffusion rate is found in the effective region, whereas in the exhaustion stage, the rate of diffusion

decreases due to the exhaustion of the Ag source. In the exhaustion stage, the Ag diffusion rate decreases until the concentration is uniform throughout the ChG.

There are reports that the induction period can be absent [38-39]. Ishikawa [38] found the reason for this and related it to the sequence of deposition of the layers. If the Ag layer is evaporated first, then there is an induction period. If the Ag film is deposited on top of the Chalcogenide film, later, the formation of a thin diffused film on the interface of the ChG /Silver forms, which accelerates the Ag diffusion and eliminates the induction period. So, the presence or absence of the induction period is determined by the preparation procedure.

Three main factors affect Ag diffusion. These are temperature, electromagnetic energy or light intensity, and an electric field.

Ag diffusion could occur without any influence of external energy sources, mainly due to the concentration gradient and the high affinity of the chalcogen elements towards Ag. However, this process is very slow and usually does not affect the performance of the devices based on Ag diffusion in ChG. When Ag is exposed to light illumination, then the diffusion rate increases significantly [36,38, 40].

Figure 2.10 shows the interplay of the influence of temperature and light intensity over the diffusion process. With increasing the temperature and light intensity, the time required for saturation of the Ag diffused film decreases. So, an increased temperature and light intensity can give rise to the Ag diffusion rate in the ChG.

However, The temperature influence is minor among the two, as has been established in [41] - Figure 2.11.

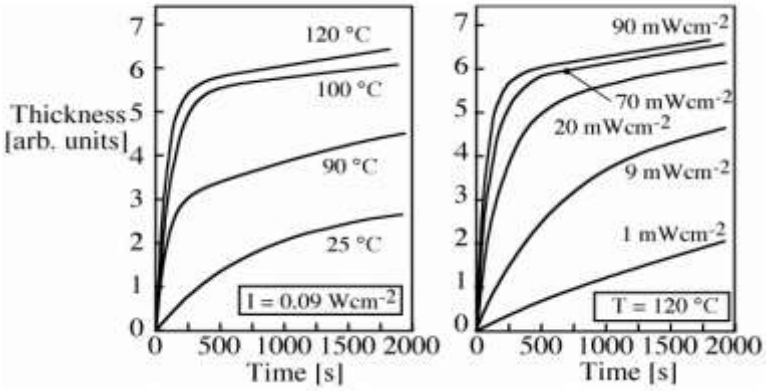

(a) **(b)**

Figure 2.10 a) Temperature and b) light intensity effect on Ag diffusionin $As_{30}S_{70}$ glass [40].

The reason for this is that the photon incident on the ChG creates electron-hole pairs. It also interacts with the Ag and generates Ag^{+} ions, which are mobile and diffuse into the glass. The diffused silver ions usually recombine to silver atoms with some of the negatively charged defects [3,30] or react with the chalcogen atoms.

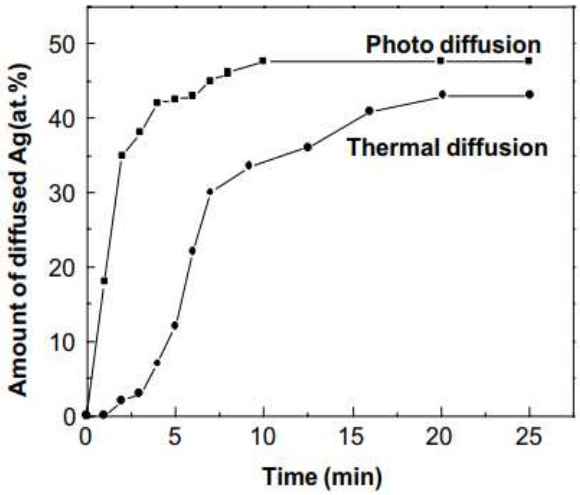

Figure 2.11 Comparison of thermally and photo-induced Ag diffusion on $Ge_{20}Se_{80}$ [41].

Another factor influencing the Ag diffusion is the availability of an external electrical field. For better effectivity, the electrical field should be greater than 10 Vm^{-1},

because there is a minimum threshold value for the applied voltage to affect the movement of Ag^{+}. If the electric field is greater than $10Vm^{-1}$, then it creates Ag^{+}, and these ions diffuse into the ChG [42]. For the radiation sensing device, which is the focus of this investigation, the Ag photo-diffusion in the ChGs, caused by electromagnetic or ion irradiation, is the main mechanism on which the device's performance is based.

When Ag^{+} ions are created during the Ag diffusion ionization process, then they move randomly throughout the structure. However, their movement depends mainly on the free volume of the amorphous film and its structure. The free volume of the ChG creates a localized network [43]. There are two types of regions in the ChG within exclusive densities. One region has a highly dense ChG network separated by Van der Waals force [44]. The other region is outside of highly dense clusters. This region is the preferred region for ion conduction [44]. This type of model is known as Cluster Bypass Model. This model is important because it describes the visualization of the free volume in the ChG. It also explores the possible region of the Ag diffusion. Other models describing the Ag diffusion in the ChG are the Anderson-Stuart Model and the Percolation Model [45-47].

According to the Cluster Bypass Model, there are pathways for the Ag diffusion, and when there is enough large force for attracting the ionized Ag particle, then Ag^{+} ions can completely diffuse from one end of the pathway to the other. In figure 2.12, the areas with the diagonal lines represent the ChG network. The region named "doped salt" defines the pathways of diffusing Ag in the ChG.

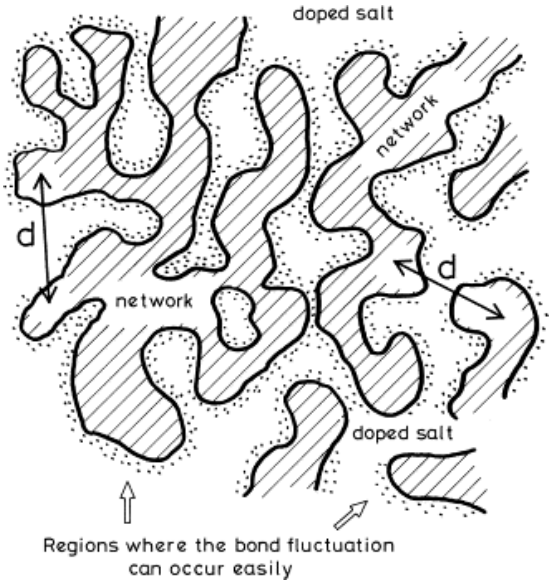

Figure 2.12 The Cluster Bypass Model [47].

When light or gamma electromagnetic waves irradiated the dual structure of ChG and Ag, then the Ag^+ ions diffuse through the available pathways in the ChG and combine with negatively charge defects and eventually form a new molecule. This is a reason for a newly formed medium to have significantly different conductivity [48], since the electron-hole pairs and Ag^+ generated by the illumination create localized states within the bandgap. These localized states behave like donor levels in it. As a result, the bandgap of glass effectively decreases, which raises the conductivity of the Ag-diffused material. This effect develops well up to a specific for each material illumination dose, after which the influence of the illumination dose diminishes due to the creation of a high number of electron-hole pairs. These charged defects are then in very close proximity and recombine very fast, so limiting the driving force for Ag diffusion. As a result, the conductivity of the Ag photo diffused material decreases, compared with the material illuminated with lower doses [49].

If the concentration of the Ag is incrementally increased, then the conductivity of the glass also increases [50]. M. Ribes et al. found that by adding 5% of Ag concentration in the glass matrix at room temperature, this contributes to 6 orders of magnitude increase of the conductivity of the Ge-S based ChG [51] as presented in Figure 2.13. Ureña *et al.* reported higher conductivity increase – up to seven orders of magnitude by adding 10% of silver in the Ge-Se system [52].

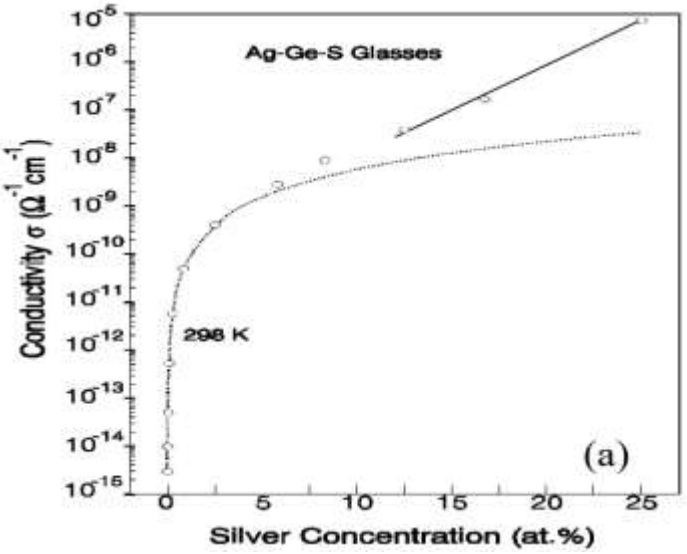

Figure 2.13 Change of conductivity as a function of Ag Concentration in Ag-Ge-S glasses [51].

The interaction of Ag with the chalcogenide matrix can also result in the formation of binary chalcogenides. They contain two Ag atoms and a chalcogenide atom - Ag_2X (X=S, Se, or Te). The binary chalcogenides usually exist in two polymorphic forms. For the Se containing binary, the two polymorph forms are β phase with orthorhombic structure, which is stable at room temperature and α phase with body-centered cubic structure, which is stable at a temperature above 133°C [44].

When Ag diffuses in ChG containing Ge, there is a possibility of formation of ternary compounds contain in all three elements- Ag_2GeSe_3 and Ag_8GeSe_6. They usually form at the terminal defects in the $Ge_{33}Se_{67}$ matrix or within the volume of a Ge richer host, for example, $Ge_{40}Se_{60}$ [50].

Table 2.2 Conductivity of Binary Ag_2X (X=S, Se or Te)

Binary Ag- Chalcogenide	The conductivity of α phase ($\Omega^{-1}cm^{-1}$)	The conductivity of β phase ($\Omega^{-1}cm^{-1}$)
Ag_2S	4.1 [44]	$6x10^{-3}$ [32]
Ag_2Se	3.1 [44]	$9.8x10^{6}$ [51]
Ag_2Te	1.0 [44]	$4.3x10^{3}$ [34]

The reaction between Ag and Se is easily occurring because the energy for the formation of an Ag-Se bond (48.4 kcal/mol) is about three times lower than the energy of the Ge-Se bond (113 kcal/mol) [53]. It consumes Se from the Se chains, or Ag is attached at the edges of the Ge-Se clusters, which leads to a very interesting effect – a serious change in the structure of the chalcogenide matrix. Even if before the beginning of the diffusion process, it has been chalcogenide rich, after the process finishes, the Raman spectra is the proof formation of Ge-rich matrix [38, 50]. It is expected this matrix will be quite stressed since the atom volume of Ag is much bigger than the atom volumes for the ChG matrix participants, which inevitably creates pressure on the surrounding atoms since Ag diffuses in the already formed network structure. Because of the lack of free volume for the formation of the diffusion products, at typical phases form – as reported in [50], the high-temperature polymorph form of Ag_2Se has been manifested by XRD studies even though the process has been conducted at room temperature. The reason is that the high-temperature polymorph form of Ag_2Se has a cubic structure which has a closer packaging than the low-temperature orthorhombic polymorph form. This space restriction and kind of application of pressure over the diffusion products are also due to the fact that the stiffness of the network increases drastically and becomes very rigid after reaction of Se with Ag.

The devices based on the Ag diffusion can have two types of structure – lateral and vertical. The mechanism for both types of diffusion is the same. In earlier researches, vertically stacked films were used. In these structures, it is hard to identify an induction period of diffusion. On the other hand, in lateral devices, the Ag layer is deposited as a strip on the top of the ChG, and Ag first dissolves due to the direct contact, and the lateral diffusion begins. It can be followed with analytical methods, which makes documenting the Ag motion monitoring easy. The rate of lateral diffusion depends on the composition of the glass [36].

There are a lot of applications based on Ag photodiffusion in ChG, such as batteries, sensors, photo-resists, memory, etc. [3,5,7,8,40,54,55]. One example is the radiation sensor fabricated by P. Dandamundi et al. [5]. They demonstrated increased conductivity in the ChG by irradiation with up to 5.13 Mrad gamma rays. The conductivity depends on the Ag interaction with the negative defects of the ChG during the irradiation and the particular compositions of the ChG [3,4-8,54-56].

The ChG host films where Ag diffusion can be achieved can be deposited by different methods. For the needs of the research on which this thesis is based, the films are deposited from ChG dissolved in basic solutions, data for which are given in the next chapter.

Dissolution of the ChalcogenideGlasses

In 1981, Chern et al. suggested a solution-based deposition technique for the ChG [11-13]. Since that time, solution-based deposition techniques such as spin coating, dip-coating, and spiral bar coating have gained popularity to achieve good quality Chalcogenide thin films. These films have been produced by dissolving the ChG in basic

solvents. Chern et al. observed that organic Alkaline Aliphatic Amines were able to dissolve the ChG [11-13] and used this process to fabricate thin films of ChG for photo-sensitive applications. Examples of their experiments include the dissolution of Arsenic Sulfide in different Amine solvents like Ethylenediamine (EDA), n-Butylamine (BA), and n-Propylamine (PA). The solutions were mixed by using magnetic stirrers applied for a few days. The authors reported that 0.4 g Arsenic- Sulfide was dissolved in 1ml n-Propylamine [14]. The dissolution mechanism of the Arsenic- Sulfide Chalcogenide glass in PA is given below:

Arsenic Sulfide has a layer like structure, and an organic solvent like PA attacks mainly the defect site of layer ChG and breaks it into small flat clusters [14].

The Alkylammonium group (RNH_2) from the solvent has a Nitrogen atom, including lone-pair electrons. The presence of these lone pair electrons makes it a nucleophilic. A nucleophile tends to donate electrons and reacts with other atoms. When this Alkylammonium group reacts with As_2S_3 atom, it substitutes one of its S atoms. Consequently, it produces an Alkylammonium group. The terminated Sulfur then reacts with excess Hydrogen, which had split off from the Arsenic Alkylammonium group and created Hydrogen Sulfide groups. This terminated Hydrogen Sulfide then reacts with another Alkylammonium group (RNH_2) and forms RNH^{3+}. This RNH^{3+} then connects with the dangling Sulfur bond (S^-). As a result, the Arsenic atom from the Alkylammonium group exhibits a lower electron density and the negative electron Nitrogen pulling away electron from Arsenic, which reduces its electron density and makes it much more reactive [11-14].

By repeating this substitution two times, finally, they got the Alkylamino-Arsenicand Hydrogen-terminated Sulfide group. In this stage, the solvent molecules, Alkylammonium Salt with the Sulfide groups, are in chemical equilibrium. The smaller Arsenic-Sulfide fragments precipitate, terminated by the excess Sulfide dangling bonds and charge compensating Alkylammonium ions, along with an insoluble Alkyl-Amino Arsenic compound.

Kohoutek et al. reported the dissolution mechanism of the Arsenic-Sulfide and n-Butylamine (BA), which follows the same kinetics of previously discussed mechanisms [15]. They found the smaller Arsenic-Sulfide fragments were surrounded by the polar Alkylammonium-Sulfide shell, which is more soluble in the solvent because of its polarity nature. The Alkylamino-Arsenic compounds were found as a precipitated compound. A schematic of this process is presented in Figure 2.14, and the chemical reactions at which it occurs are shown in Figure 2.15.

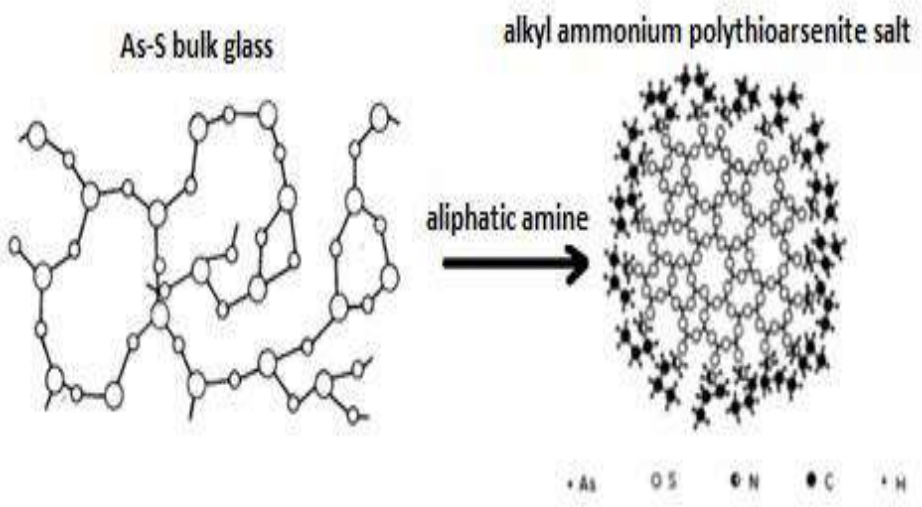

Figure 2.14 The dissolution mechanism of the As-S ChGs in Aliphatic Amines [13,14].

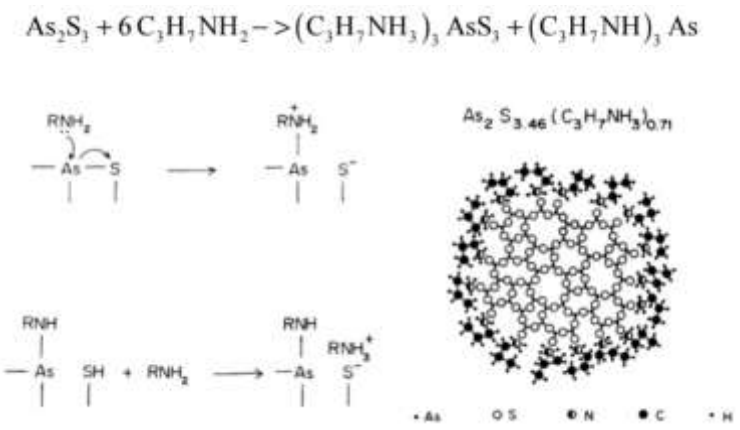

Figure 2.15 a) Chemical equations and cluster image, b) Electrophilic substitution reaction proposed for the Arsenic-Sulfide dissolution process [13,57].

The dissolution mechanism of the Arsenic-Sulfide with the EDA was investigated by Guiton and Pantano in the late 1980s [16-17]. They claimed that they had found polymers like a chain of As_4S_4 rings, which were interlinked by the bridging Sulfur atom instead of the Alkylammonium salts or Hydrogen-Sulfide (claimed by Chern et al.). Thus the glass broke into a polymer-like chain. They had figured out that the diamine solvent has a chelating nature.

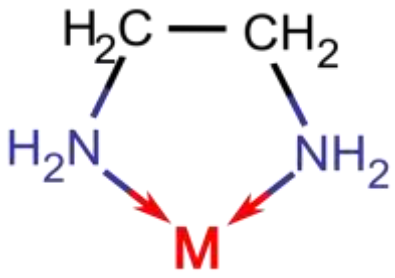

Figure 2.16 Ethylenediamine ligand chelating to a metal with two bonds [58].

Chelating is a chemical process where two or more coordinated bonds are connected with the metal ion or molecules and form a ring-like center, as shown in figure 2.17. Guiton and Pantano dried the solution and claimed that the materials have loosed

solvent and condensed like a sol-gel process of silicate glass [17]. In the sol-gel process, a metal oxide solid layer is formed by evaporating the solvent and condensing of materials by heating.

In the 1990s, Mamedov and Michailov reported the dissolution of Arsenic-Sulfide in Alkaline water solutions [59-60]. This dissolution mechanism is similar to the previously discussed Arsenic-Sulfide dissolution mechanism in n-Butylamine. This dissolution occurs in two steps. In the first step, the adsorption of nucleophiles (Hydroxyl Anions or Amine groups) occurs at the surface of the glass. In the second step, the Sulfur atom is substituted by the nucleophile. The rate of dissolution depends on the homopolar bonds of solvent. Homopolar bonds decrease the electrophilicity of glass networks. As a result, the lone pair from the N atom will be reduced, and the dissolution rate will be slower. However, in the Arsenic Sulfide glass, both homopolar (S-S chains, S rings) and heteropolar bonds (As_xS_{100-x}) exist [59-60].

In summary, even though the above experiment was done by using Arsenic Sulfide, other Sulfur or Selenium-based ChG would follow the same mechanism. The similarity of this mechanism is that the solvents tend to be electron-rich, and as a result, dissolution starts with nucleophilic attacks.

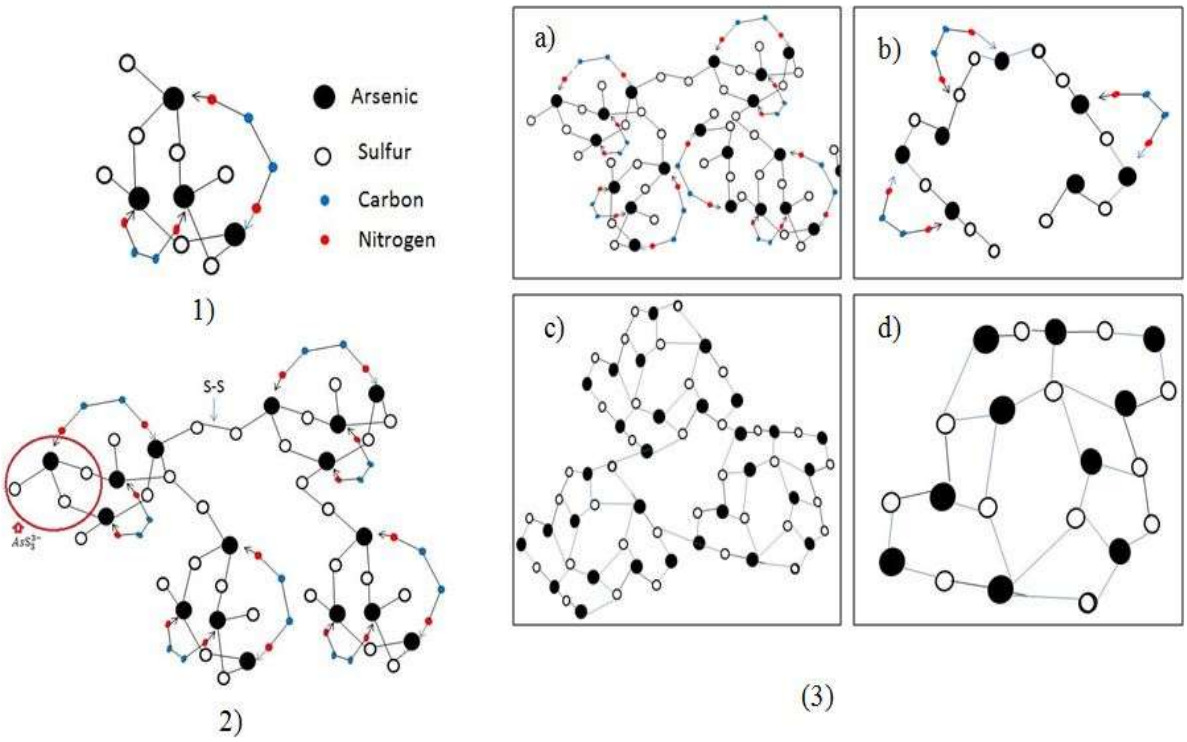

Figure 2.17 Proposed As_2S_3/EDA solution species and gel-to-glass transition. (1) Lewis acid-base chelation model, (2) Branched chains (3)(A) Solution species; (B) Amine loss; (C) Elimination of As-S-S-As; (D) Amorphous network. Reprinted with permission from Chem. Mater. 1(5),558-563(1989) [16-17,60].

The main difference between the two mechanisms (where solvents were EDA and n-Propylamine) was that the EDA breaks the glass into a polymer-like chain, while the Propyl-amine breaks the glass into small fragments in the form of small clusters.

Song et al. dissolved bulk As_2S_3 (99.9% pure) with Butyl-amine. First, they made a powder of As_2S_3. Then, they mixed 2.50 g of As_2S_3 powder with 10 ml of Butyl-amine. However, they continued this dissolution process for four days. The authors used this solution to make As_2S_3 cladding for the quantum cascade (QC) laser [61].

Another study by Slang et al. examined ternary $As_{20}Ge_{12.5}S_{67.5}$ composition for analyzing photoinduced effects in spin-coated $As_{20}Ge_{12.5}S_{67.5}$ thin films. They dissolved

0.075g ternary ChG with 1 ml n-Butylamine (BA) solvent for that purpose and prepared $As_{20}Ge_{12.5}S_{67.5}$ thin films by the spin-coating method using this dissolution [62].

Zha et al. reported that they dissolved amorphous As_2Se_3 with the Ethylenediamine (EDA) solvent at a concentration of 0.8mol/L. They fabricated a thick (>10μm) Chalcogenide multilayer structure by the spin-coating method for studying the photo-induced Ag dissolution [63].

Slang et al. described that they had prepared thin films using a spin coating technique with the $Ge_{25}S_{75}$ ChG and studied photoluminescence of $CdS_{0.9}Se_{0.1}$ quantum dots embedded in the spin-coated $Ge_{25}S_{75}$ thin films. Therefore, they had dissolved pure 0.804g $Ge_{25}S_{75}$ ChG with 1 ml of BA [64].

The dissolution based ink formulation, characterization, and printing process will be discussed in the next chapter.

CHAPTER 3: INK FORMATION, PRINTING AND SINTERING PROCESS

Nowadays, additive manufacturing (AM) has become a popular and low-cost method over conventional methods for fabricating electronic devices. The reason behind the low production cost of AM technology is that in conventional electronics, circuits need separate components for function. Printing is additive with an associated low waste of materials because subtractive processes such as lithography, etching, etc. are not included in this technology. Different kinds of sensors, antenna, coils, capacitors, memory components, and their integration can be printed using combinations of different inks to give the desired properties [65]. AM has attracted manufacturing industries because of the low fabrication cost of large-area electronic devices such as flexible display devices, printed sensors, memory devices, and radio frequency identification (RFID) tags [66-67].

In this project, a nano-ionic radiation sensor was fabricated using the AM process. Several steps were followed for the fabrication process.

1. Synthesis of GeSe based ChG,
2. Ink formation from the ChG,
3. Creation of device architecture with CAD,
4. Transport of CAD data to the printer,
5. Printing on substrate using of the ChG ink,
6. Sintering process of the films,

7. Printing additional films necessary for the device, following the technological steps given above.

One overview of all steps and their interrelation are presented in the flow chart of this technology in Figure 3.1.

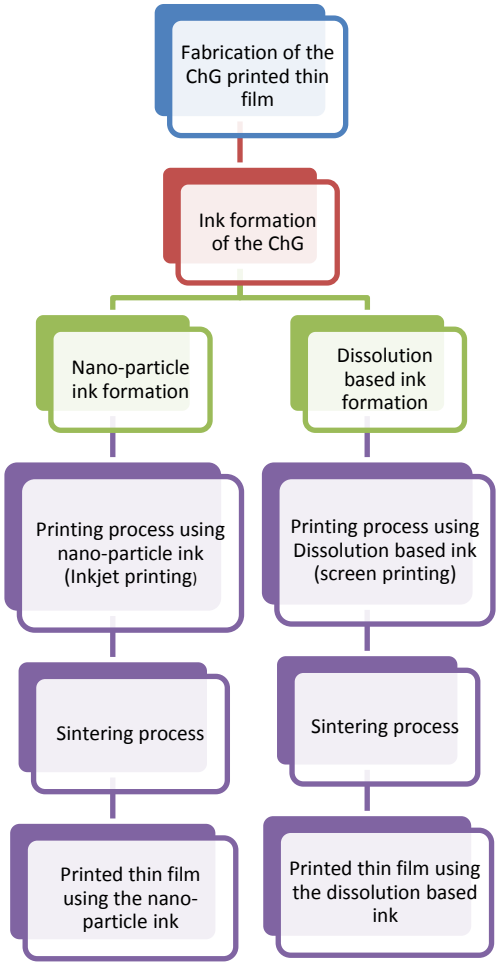

Figure 3.1 Flow chart of fabrication of Chalcogenide Glass printed thin films.

Details of each of the technological steps are given in the following chapters.

Synthesis of Ge-Se Based Chalcogenide Glasses

The ChG ink preparation starts with the synthesis of the ChG. In this project, Ge-Se based ChG was used for fabricating the printed radiation sensor. Ge-Se based ChG is

thermally stable and has a tendency to form a wide range of glass compositions; this type of glass is not as toxic as As based ChG [3].

The melt-quenching technique was followed for preparing Ge – based ChG. First, the weight of 5N pure Ge and Se elements was measured according to atomic percentage participation. All the measurements were taken under ambient temperature.

The measured elements were loaded in 10 mm diameter and 10 cm long fused silica ampoules. After that, the ampoules were sealed at a 10^{-4} Tor vacuum. Then, the fused silica ampoules were placed into a programmable tube furnace programmed at different temperatures for different durations of time, in accordance with the ChG glass phase diagram [3].

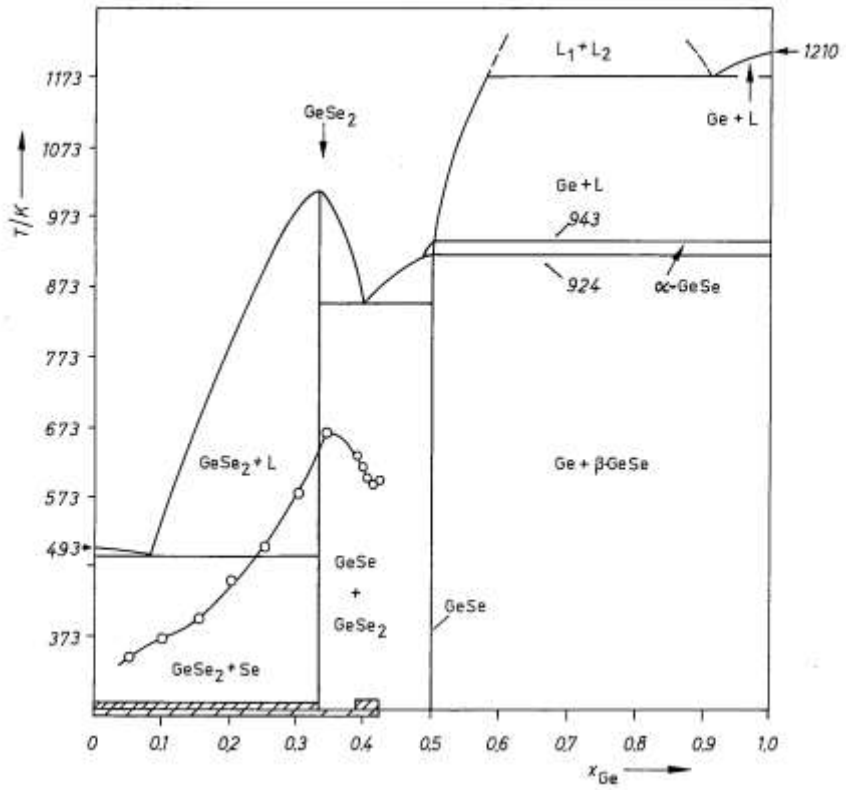

Figure 3.2 Phase diagram and glass-forming range in the system Ge_xSe_{1-X}, showing T_g values (O) as functions of mole fraction x [68].

The temperature duration highly depends on the melting temperature of the glass component and its partial vapor pressure [3]. One example is given in Table 3.1.

Table 3.1 Ge-Se based ChalcogndeGlassesproduction temperature at a different phase

Phase	Temperature	Duration
1st phase (the element with the lowest melting temperature (Se) is liquid, and a liquid-solid reaction occurs in the ampoule)	350°C	5 hours
2nd phase (the mixture is in a liquid phase accordingly to the phase diagram)	450°C	5 hours
3rd phase (the highest melting temperature, Ge could be melted at this temperature if there are not melted traces of this element)	950°C	5 hours
Last phase (all elements of the particular mixture melted and a good homogenization can occur)	750°C	96 hours (This long time is necessary for a good homogenization of the melting)

After the period shown in table 3.1, the fused silica ampoule was quenched into ice-cooled water immediately after it has been taken out from the furnace. For this project work, $Ge_{20}Se_{80}$, $Ge_{30}Se_{70}$, $Ge_{33}Se_{67}$, and $Ge_{40}Se_{60}$ compositions, which represent Se rich, the stoichiometric, and Ge rich members of the Ge-Se system were prepared by this melt quenching technique, the process flow of which is shown in figure 3.3 and ChG are shown in figure 3.4.

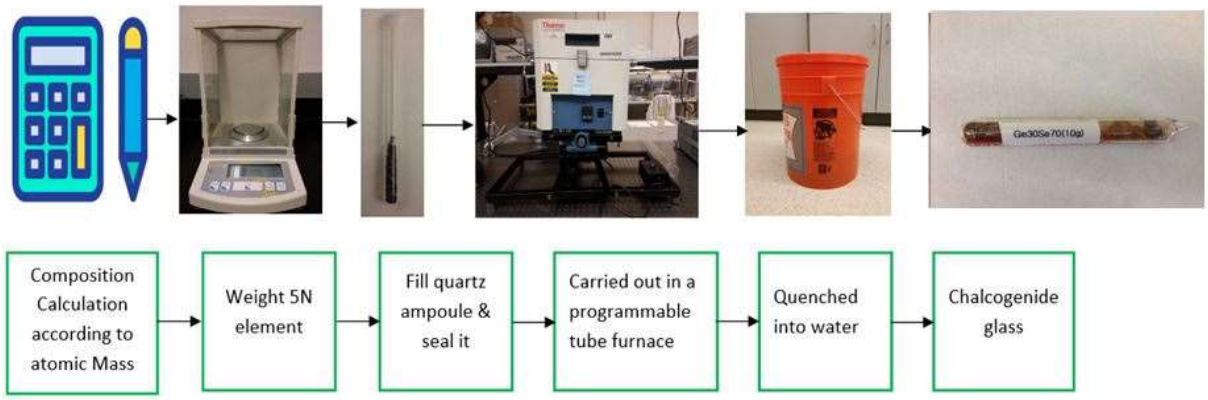

Figure 3.3 The Chalcogenide Glasses synthesis process.

Ink Formulation

Ink formulation is one of the major steps of AM technology. There is no commercially available ChG ink in the market. The ink was produced in our laboratory using two different methods. Those were the dissolution of ChG in amines ink and a nanoparticles based ChG ink.

Figure 3.4 $Ge_{20}Se_{80}$, $Ge_{30}Se_{70}$, $Ge_{40}Se_{60}$ Chalcogenide Glasses samples.

The main idea of making these types of ink was to dissolve synthesized bulk ChG into Amine and make a solution for printing. For the dissolution based ink, two different types of solvent were used; those were Ethylenediamine (EDA) and Propylamine (PA).

There are limited literature data available for the particular dissolution process of Ge containing ChG with Amine [69-71]. However, a similar dissolution mechanism (As based ChG) was described in many details as outlined in the literature review chapter 2 of this thesis [11-17].

First, a particular composition of the ChG was crushed into a fine powder using an agate mortar and pestle. Then, the powder was mixed with one of the Amines (EDA/PA) for a couple of days into a volumetric flask. The dissolution rate of Ge-Se based ChG into the solvent was 0.08g/20 ml. To speed up this dissolution process, the solution was stirred by using a magnetic stirrer at the rate of 700 rpm for 72 hours. During the whole process, the lid of the volumetric flask was kept closed by para-film to prevent evaporation. Finally, the solution was filtered through a 0.025 µm nylon filter using the vacuum filtration technique for removing the big particles. The prepared ink can be applied for printing on a substrate using a screen printer or nScrypt printer. Terpineol has been added to the solution to increase its viscosity and improve in this way the resolution of the printed films. It had been optimized that 5-10% of Terpineol is enough for achieving a good resolution of screen-printed patterns. The process flow of the formation of dissolution based ink is shown in figure 3.5, and ink examples are prested in figure 3.6.

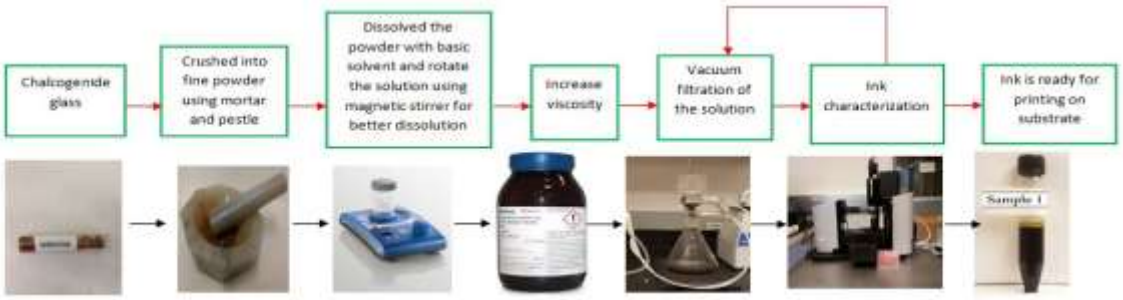

Figure 3.5 Formulation of dissolution based Chalcogenide Glass inks.

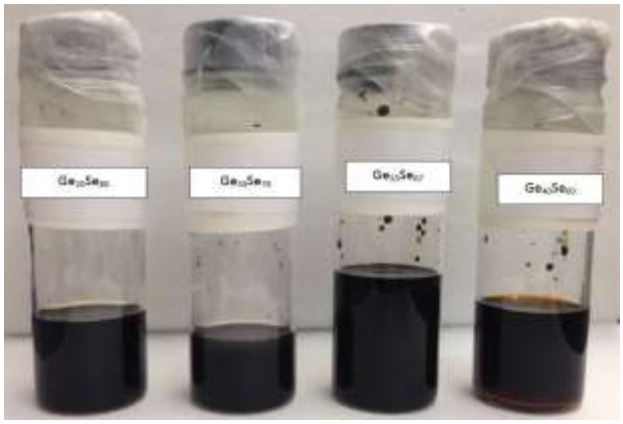

(a)

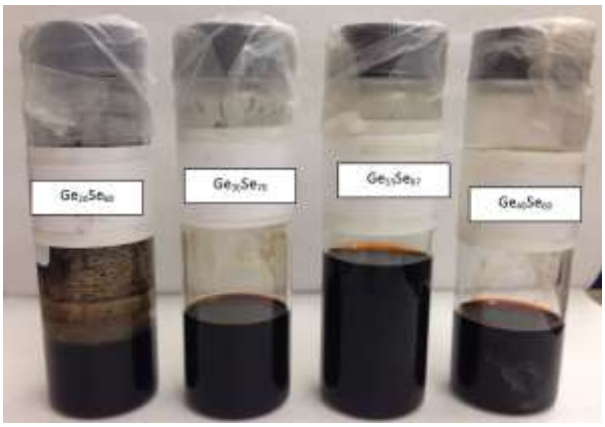

(b)

Figure 3.6 The dissolution based Chalcogenide Glass inks, a) solvent EDA, b) solvent PA.

Dissolution Based Chalcogenide Glass Inks Characterization

Before the printing process, the dissolution based ink was characterized using the tensiometer. It was used to measure the contact angle of the ink with the substrate. This is the angle between the droplet outline and the substrate. The contact angle provides information about how well an ink will spread over a substrate. It is a vital indicator during the ink formulation process. The contact angle mainly depends on the physical properties of the materials (the ink and substate)[72]. Figure 3.7 shows various types of contact angle. The left-most droplet has a large contact angle with the substrate. The larger contact angle represents a lowest in the wettability because of which the liquid

does not spread over the substrate. The right most droplet has a small contact angle with the substrate, and it spreads well over the substrate. For the best printed thin film, a low contact angle is the desired outcome, since it assures high resolution at printing.

The tensiometer measured the contact angle by following two steps: recording and analysis. First, the stage was flattened to make sure that the droplet of ink does not move during deposition. After droplet depositing on the stage, an image was recorded by a camera. Then, the image is analyzed using software to determine the contact angle- figure 3.8.

Figure 3.7 Various contact angles [72]

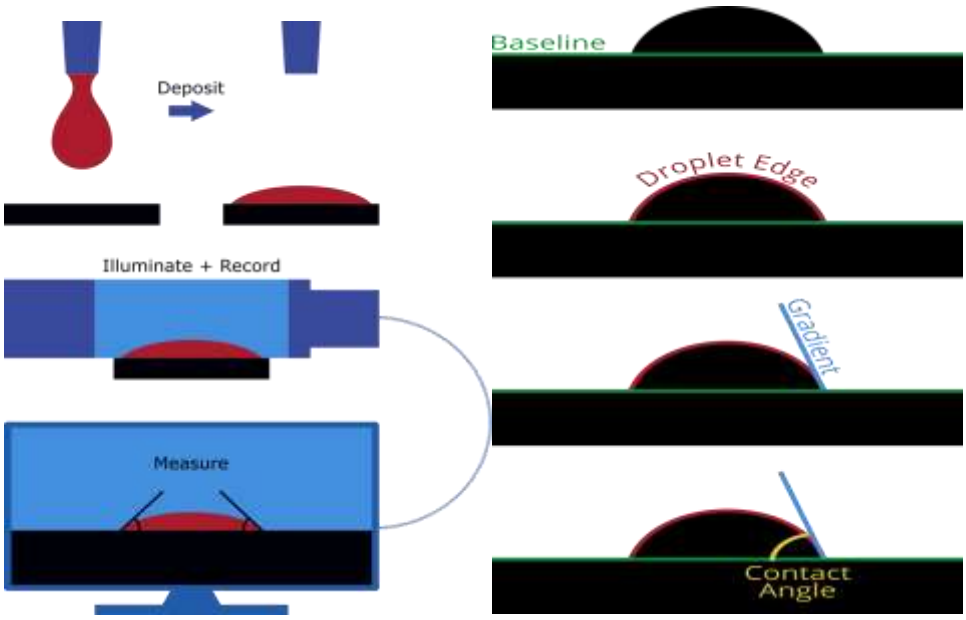

Figure 3.8 Contact angle measurement process [72].

The baseline represents the substrate on which the droplet was deposited. The software traced the droplet edge and determined the gradient of the tangent of the droplet edge with respect to the baseline. Finally, the angle was calculated by using this equation:

$\tan\theta = \text{opposite/adjacent}$.

The Printing Procedure of Chalcogenide Glass Inks (Dissolution Based Inks)

Printing Process:

The screen-printed method was used to print the ChG thin-film using dissolution based ink. This method was preferred because the amines are alkaline in character, and there are concerns that they could dissolve the plastic cartridge nozzles or other plastic parts of the printers in use at IML.

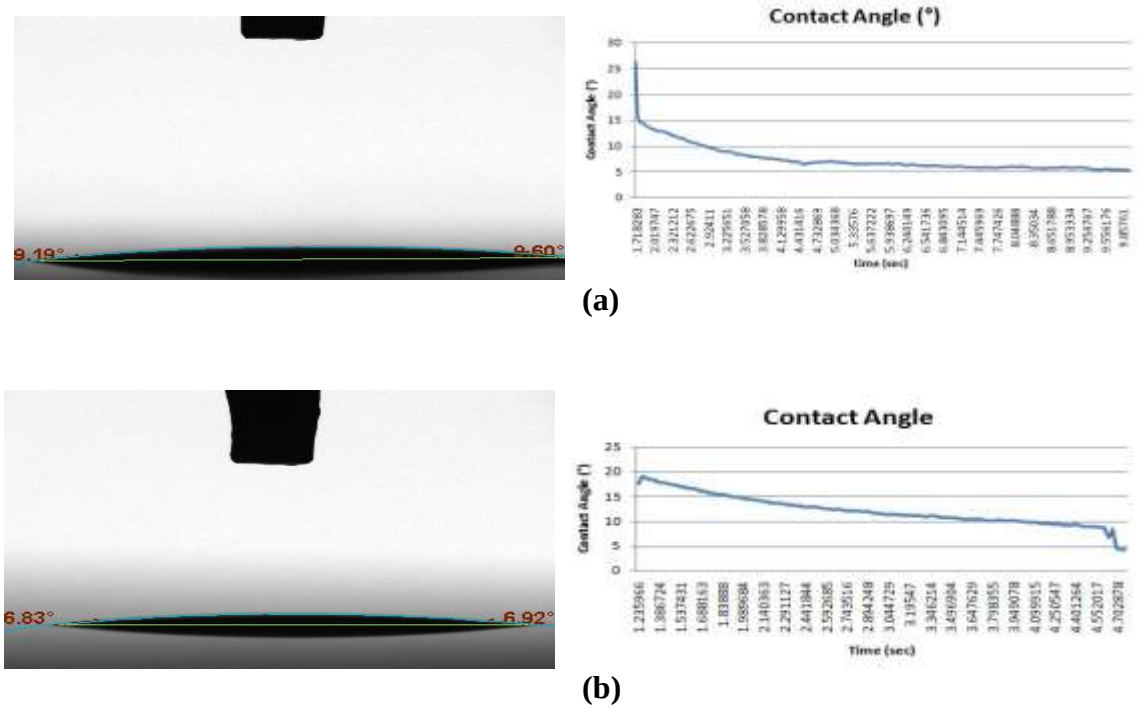

Figure 3.9 Contact angle on a) Si substrate, b) SiO_2 substrate.

Substrate preparation:

A Si wafer was used as a substrate. The thickness of the substrate was 550 nm, and the diameter was 10 cm. The substrate was initially covered with an insulating film obtained by a dry oxidation process – Figure 3.10. Without an oxide film, the device fabricated out of the ChG film would have been shorted by conducting the electrical field throughout the Si substrate. The thickness of the insulation layer (SiO_2) was 275.78 nm. One other option for the substrate used for printing of the films was the application of a Kapton film (5 mils). The Kapton substrate was preheated at the same temperature of the sintering process for 15-20 minutes to avoid shrinking during the sintering process. The oxide film thickness was measured using the ellipsometer – Figure 3.11. The data show that the oxide film thickness differs over the substrate. However, since its role is only for

insulation from the substrate, which can be satisfied at all shown thickness values, we assume that the oxide film is a good base for active film deposition on it.

After the oxidation process, the substrate was treated with Oxygen plasma at 100W for 5 min to remove the unwanted particles and obtain good adhesion of the printed layer on the substrate - Figure 3.12.

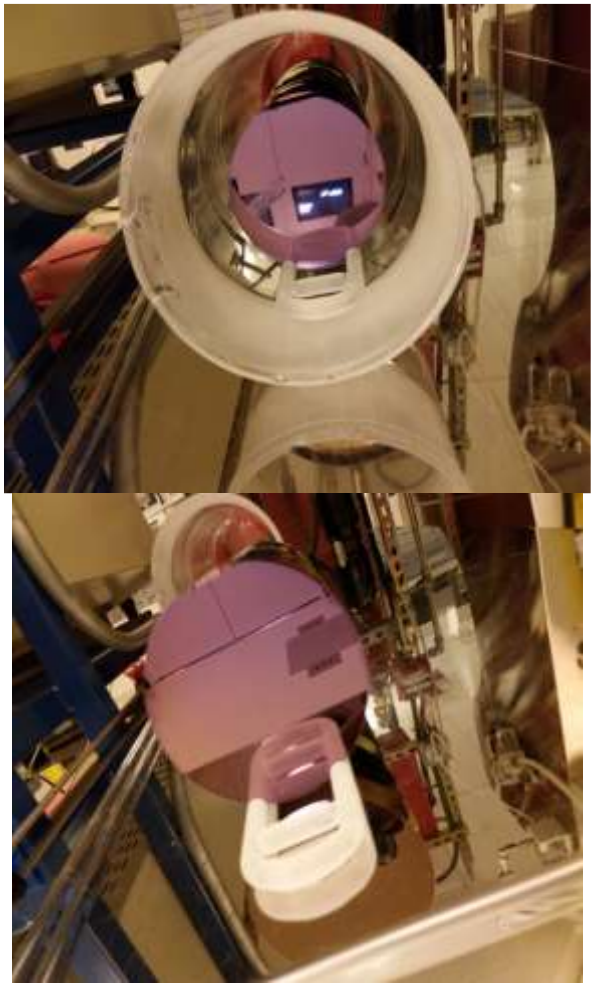

Figure 3.10 Dry Oxidized Si Wafer.

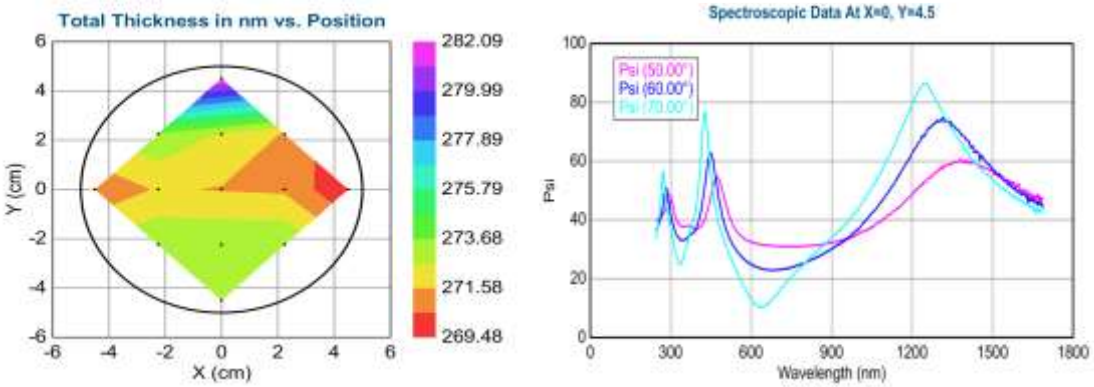

Figure 3.11 Ellipsometer data for calculating the average thickness of the silicon oxide layer.

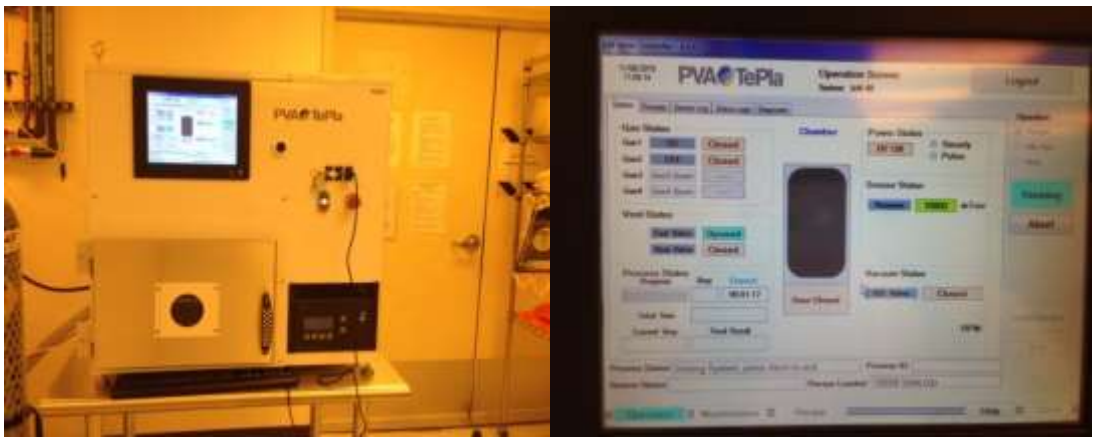

(a) **(b)**

Figure 3.12 a) Oxygen plasma system, b) recipe followed for cleaning the substrate.

Screen preparation:

The screen preparation for printing is shown in figure 3.13. First, a monofilament Polyester fabric was stretched extremely tightly on a metal frame. Then, a photosensitive emulsion was coated over the fabric, which is known as the stencil. The combination of the stencil and the metal frame form the screen. After drying the photosensitive emulsion, the desired printing design was transferred to the screen. In this process, a desired printing designed transparent sheet was laid onto the emulsion coated screen.

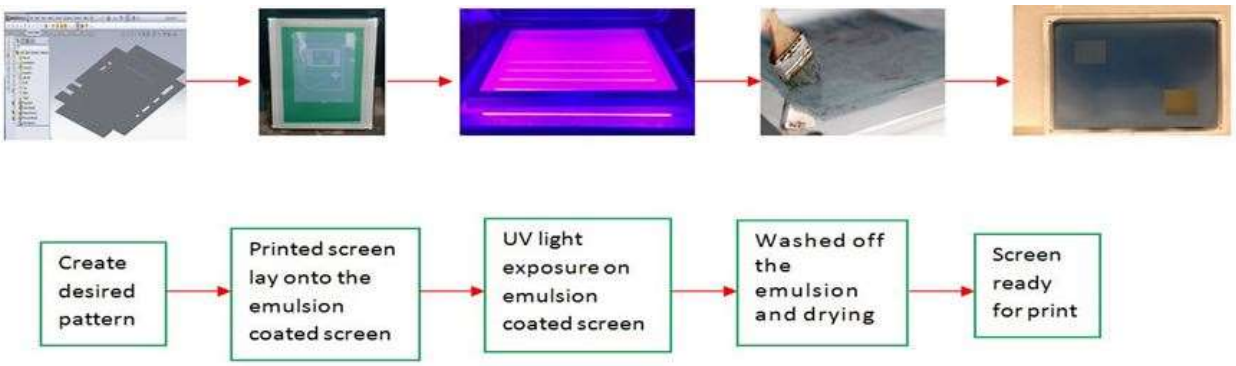

Figure 3.13 Screen preparation process.

After that, this setup was exposed to UV light. As a result, UV light went through the transparent design, and the exposed area became hardened, and cannot be washed away. On the other hand, the unexposed area was easily washed away using water. At the end, the desired printing pattern has been transferred to the screen. Finally, the screen was completely prepared for the screen printing process.

Screen printing process:

The screen printer was used for printing the ChG thin-film – Figure 3.14. First, the screen was placed on the printing press. The substrate was placed on the flat printing board, underneath the screen. Then, the screen was placed onto the printing board. The ink was added to the top end of the screen. A squeegee was used to pull the ink along the full length of the screen.

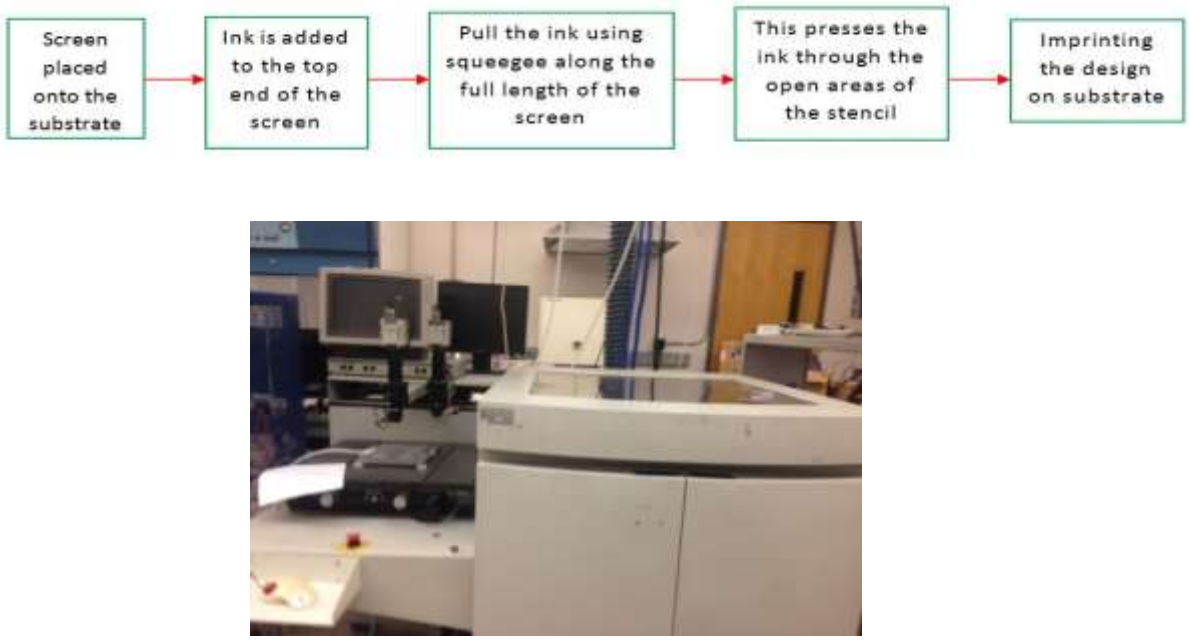

Figure 3.14 Screen printing process and screen-printer.

This squeegee press transferred the ink through the open areas of the stencil design. As a result, the desired design was imprinted on the substrate. By following these steps, a square-shaped design was printed on top of the substrate using dissolution based ink. The thickness of the printed film can be varied by changing the emulsion thickness of the screen.

Sintering Process

After the printing process, the sintering process is the next essential part of the AM process. The printed and dried film patterns are usually highly resistive due to the high inconsistency of the films, which is improper for practical applications. Sintering is a process by which the printed particles are combined to create a solid film. This helps to form a conductive printed pattern. The sintering process depends on some factors such as the composition, the particle size, the heat rate, the sintering temperature, the sintering time, the liquid phase formation, and so on [70]. The sintering process also helps the printed pattern or film to have better adhesion to the substrate. The basic sintering

process is exposing the printed film to heat, intense light, microwave radiation, plasma, or an electric field, which triggers the formation of continuous films [71]. The main challenge is to remove the solvents from the surface of the printed pattern and break down the polymer backbones. Since the ChG is a photosensitive material, the thermal sintering process has been followed in this project – Figures 3.15 - 3.17.

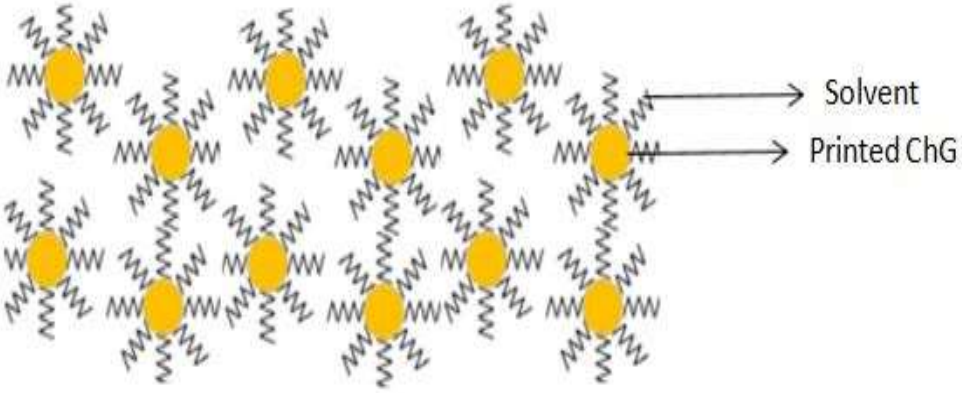

Figure 3.15 Printed film before sintering.

As mentioned before, EDA/PA was used as a solvent. The boiling point of EDA is 116°C, and of PA it is 51°C, respectively. The printed film was placed into a vacuum furnace at 100°C for 24 hours. In this phase, the solvent of the dissolution based ink was evaporated from the surface of the printed film.

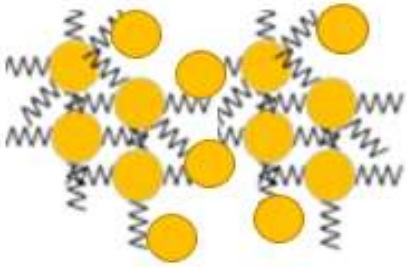

Figure 3.16 Solvent evaporation of printed film.

The second sintering phase was carried out at 130°C for 24 hours. In this phase, the particles of the printed film agglomerate close together and create a solid film.

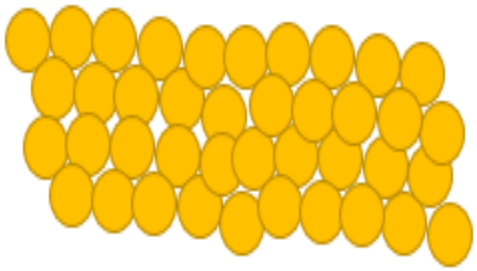

Figure 3.17 Sintered printed film.

The vacuum furnace window was covered with Aluminum foil to avoid light to avoid the occurrence of photoinduced processes in the sintering films, due to the photosensitivity properties of the ChG. The temperature was increased in increments of 20°C with a hold of 15 minutes between them starting at room temperature and reaching 100°C slowly during the first phase of the sintering process to avoid cracks formation on the printed films.

Figure 3.18 Vacuum furnace.

Images of the films before and after sintering are shown in Figures 3.19 and 3.20, along with a microscopic image of the center and the edge of the sintered film.

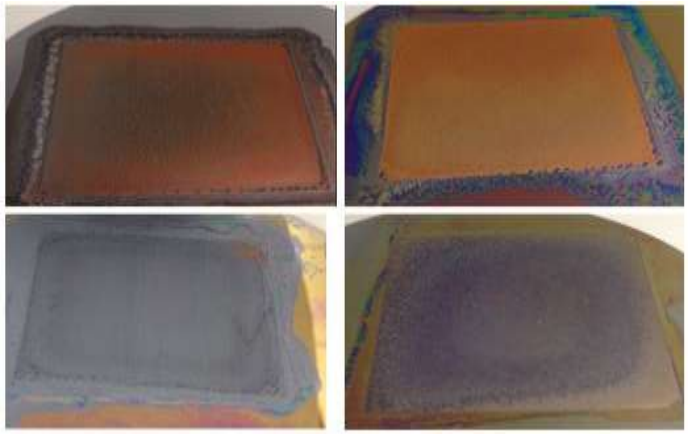

(a) **(b)**

Figure 3.19 The Chalcogenide Glass printed films with a) EDA solvent before sintering, b) after sintering.

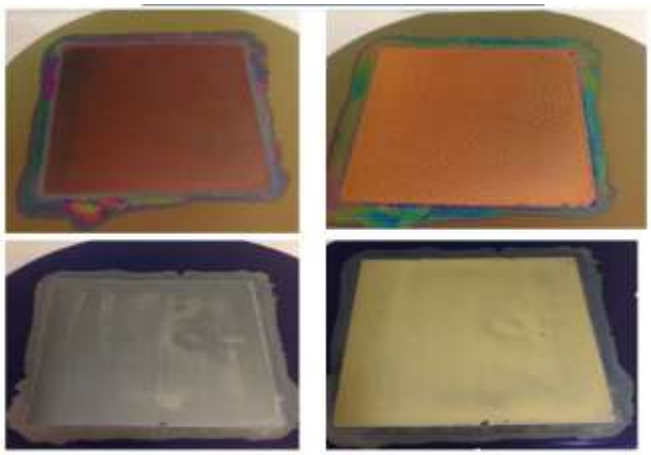

(a) **(b)**

Figure 3.20 The Chalcogenide Glass printed films with PA solvent, a) before sintering, b) after sintering.

The screen-printed films had high surface roughness–Fig. 3.22. It can be managed to some extent by increasing the ink's viscosity, which can allow the spreading of the material under the screen. However, the variation of the ink's viscosity requires strict control because, on the other hand, lower viscosity contains the shape and specifically the edges of the films. After sintering, the films changed their color, which is an indication for the occurrence of the processes, shown in Figures 3.15-3.17.

(a) **(b)**

Figure 3.21 Microscopic picture of the Ge30Se70 printed film after sintering, a) center view, b) edge view.

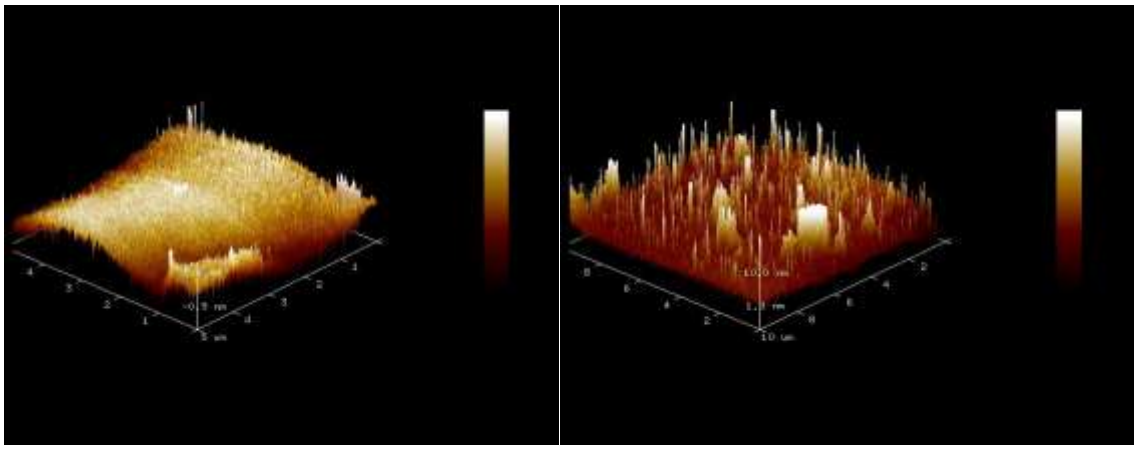

Figure 3.22 Chalcogenide Glass printed films roughness.

Nanoparticles Based Chalcogenide Glass Inks Formulation

Besides the dissolution based ChG ink, nanoparticles based ChG ink was also formulated in our laboratory– (Figure 3.23) in order to have a comparative base about the performance of devices obtained by the deposition of different types of films. The main focus of this thesis is on the dissolution based ChG ink printed film and the fabricated radiation sensor. A summary of the nanoparticles glass ink formulation, the printing process, and the sintering process are given below:

The production of nanoparticles ink started with the ChG synthesis. After the bulk glasses were synthesized, mortar and pestle were used to make a fine powder of ChG.

First, the high energy ball milling technique was used to get the nanostructure ChG powder materials. The wet milling method was followed because of less power consumption, increasing the capacity of grinding, and no dust formation. The Cyclohexanone and Ethylcellulose (EC) were mixed with the ChG powder during the wet milling process as a solvent and a stabilizing agent, respectively. Ethylcellulose was used to prevent the agglomeration of the nanoparticles. During the ball milling process, the ChG powder was squeegeed by collisions between the milling balls, as well as by collisions between the milling container and milling balls. The balls were rotated with high energy inside a container as a result of centrifugal forces and then fell on the powder. Therefore, the ChG was crushed into nanoparticles. Coolant has been used to keep the temperature in the ball mill close to room temperature in order to avoid crystalline of the milled material. After that, the stock solution was placed into an ultra-sonicator for 16 hours with high frequency (1000 Hz). The ultrasonicator transfers vibrational energy to the mixture. Then, the stock solution was centrifuged at 4500 rpm to get a uniform particle size. The 250-270 nm particle size resulting after these processes were satisfactory for printing an inkjet printer. The process flow of nanoparticles ink formation is presented in figure 3.23.

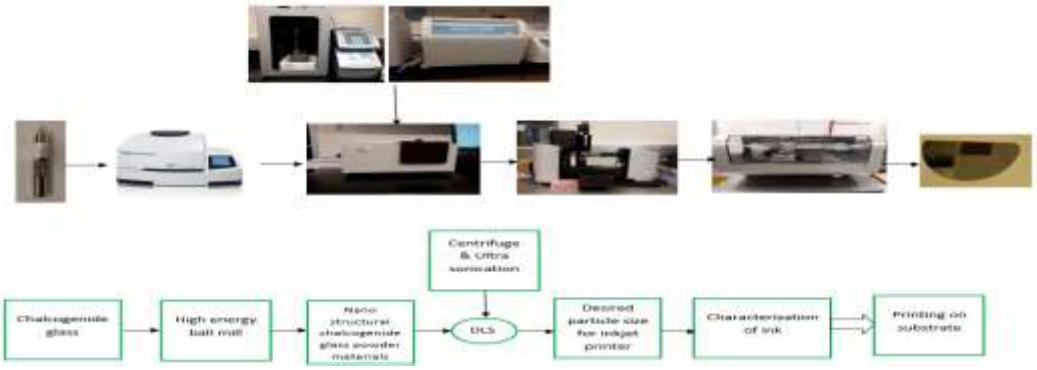

Figure 3.23 Formulation of Chalcogenide Glass nanoparticles based inks.

Nanoparticles Inks Characterization

The Dimatix printer (DMP 2800) has some parametric limitations for printing with nanoparticles ink, examples of which are presented in figure 3.24. For example, the particle size should be less than 300 nm, and the viscosity range of the ink is required to be between 2-12 cP. The particle size of the nanoparticles ink was measured by using the dynamic light scattering (DLS) system figure 3.25(a).

Figure 3.24 Different composition of nanoparticles inks.

When using the Dimatix printer (DMP 2800), viscosity is another characteristic that has to be closely controlled. It is a measurement of the resistance of a fluid to deform under shear stress or to flow. The viscosity of nanoparticles ink was measured by the viscometer–Figure 3.25(b). The nanoparticles based ChG ink has 5-12 cP viscosity at room temperature. This is within the requirements of the printer, and so the ink was compatible with it. The tensiometer measured characteristics of the nanoparticles based ink was the contact angle with the applied substrate.

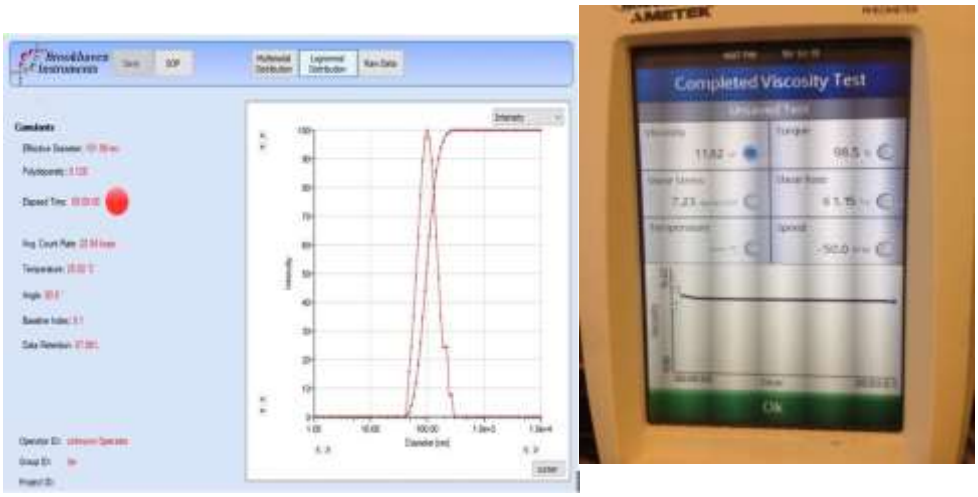

(a) **(b)**

Figure 3.25 a) Particle size measurement, b) viscosity measurement.

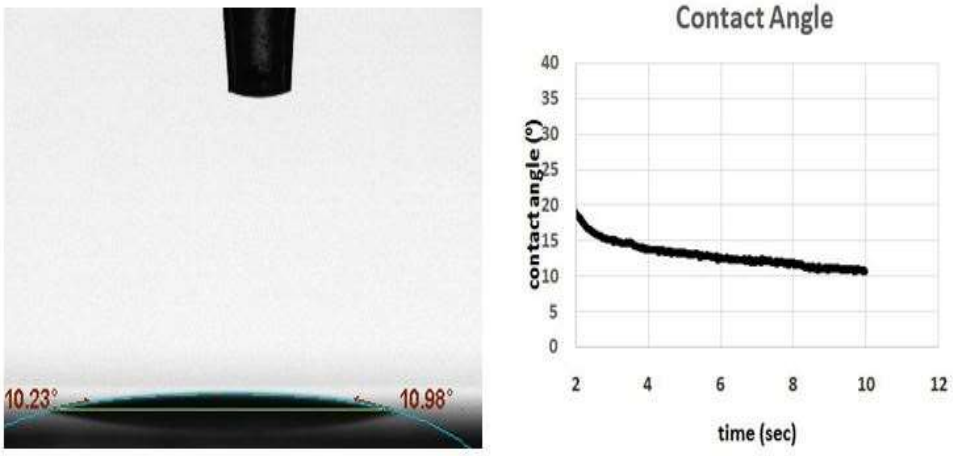

Figure 3.26 Contact angle of the nanoparticles ink.

Both the viscosity and the contact angle are of high importance for the ink performance because they form its resolution. Since the additive technologies have limited achievement on the fabrication of small devices, increasing the resolution is vital in order to produce as small as possible devices, which usually have much more stable performance.

Printing Process

The DMP 2800 model that was used for the printing of the ChG thin film on the substrate with nanoparticles based ink is shown in figure 3.26. The ChG nanoparticles ink was injected into the cartridge using a syringe. The droplets of ChG nanoparticles based ink were jetted from the print head of cartridge to the substrate. This printer follows the drop-on-demand (DOD) method. The flow of ink drops was controlled by tuning the jetting voltage of each of the individual nozzles. Generally, two or three consecutive nozzles were used, and the other nozzles were turned off. Before beginning printing, the ink cartridge, the cleaning pad, and the substrate were placed inside the printer. The print origin was set by using the camera. The drop watcher helped to monitor the performance of each nozzle individually. Finally, by using the printer operating software, the AutoCAD file of the desired printing pattern was loaded, and the number of layers for printing was selected. Then, the print option was chosen to start printing.

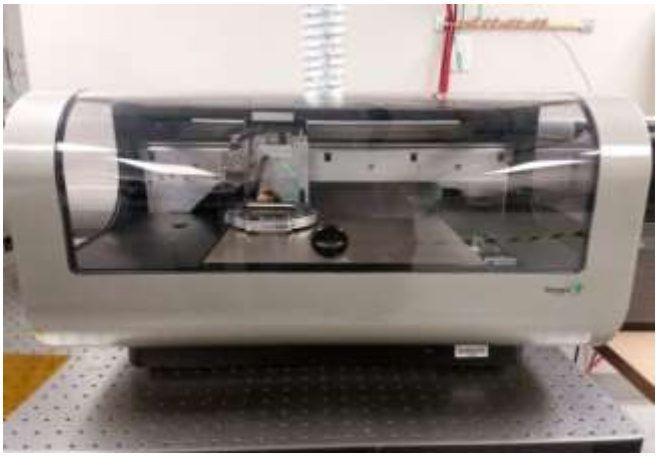

Figure 3.27 Inkjet printer (DMP 2800).

Sintering Process

The printed film was sintered in two steps. The first step was required to evaporate the solvent very slowly to prevent cracking in the thin film. The films were

annealed at 80°C for two days in a vacuum furnace. Then, the thin films were heated in an argon-filled chamber at 350-400°C for 3hours. During this step, the surfactant decomposes, and sintering starts. Examples of nanoparticles printed films are shown in figure 3.28.

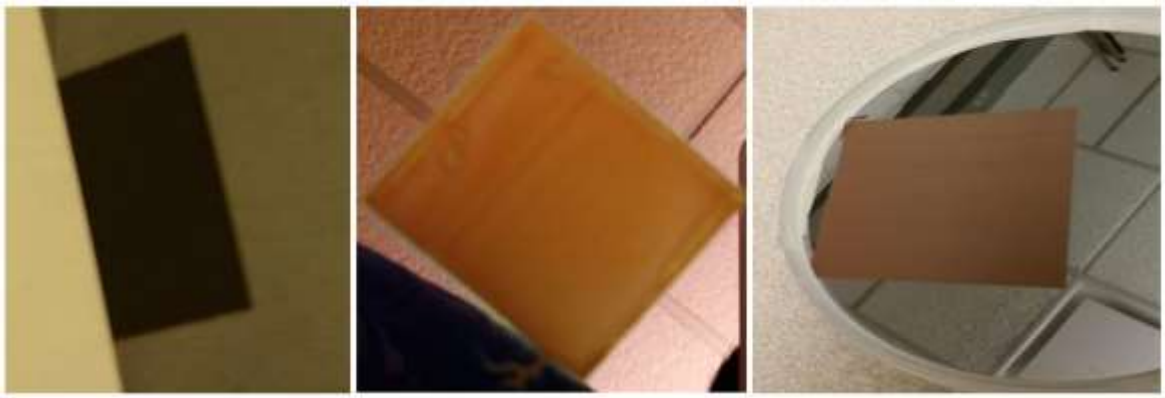

(a) **(b)** **(c)**

Figure 3.28 The a) $Ge_{20}Se_{80}$, b) $Ge_{30}Se_{70}$, c) $Ge_{40}Se_{60}$ printed film (nanoparticles based ink).

As shown in figure 3.29, the quality of the films was quite satisfactory since the SEM picture displaces homogeneity, and the edges shown on the microscopic photos promise good resolution since they are well defined. These printed films were characterized by different methods & analyzed to prove their structure and composition, as well as to understand irradiation effects in them.

The three compositions ($Ge_{20}Se_{80}$, $Ge_{30}Se_{70}$, $Ge_{40}Se_{60}$) of nanoparticles inks were printed and sintered by following the same method described in this chapter. The printed ChG layers were used to fabricate the radiation sensor. In the next chapter, the printed film analysis will be discussed.

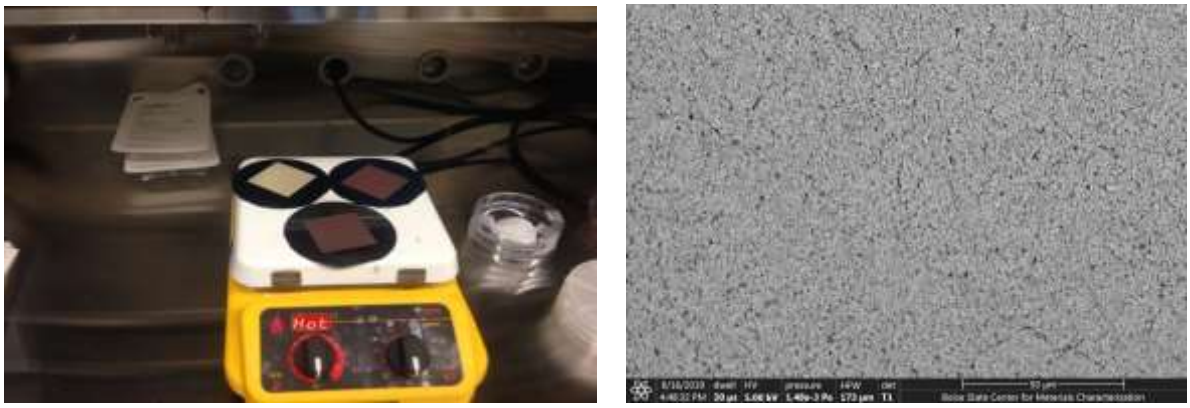

(a) **(b)**

Figure 3.29 a) SEM picture after sintering ($Ge_{30}Se_{70}$ printed film), b) sintering process in the Ar filled the chamber.

CHAPTER 4: PRINTED FILMS ANALYSIS

The printed thin films of $Ge_{20}Se_{80}$, $Ge_{30}Se_{70}$, and $Ge_{40}Se_{60}$ were characterized using Energy Dispersive X-ray Spectroscopy (EDS), Atomic Force Microscopy (AFM), and Raman Spectroscopy. The objective of this film characterization was to get an idea about the structure and composition of the film, as well as the UV light irradiation effect on them and understand the relationships between composition structure and performance of the studied films.

Energy Dispersive X-ray SpectroscopyResults

Energy Dispersive X-ray Spectroscopy (EDS) was performed using the FEI TENEO field emission scanning electron microscope (FESEM). The electron accelerated voltage was 20 kV, and the working distance was 10 mm during the measurement. The same parameters were used to maintain consistency. In this method, an electron beam was generated by applying a voltage bias across a filament. This electron beam was directed to the sample printed film through apertures and the beam aligner [73]. When the electron beam hits the sample, it knocks out the inner shell electrons from the sample. Occurred in this way, electrons are called secondary electrons [74]. At that moment, the outer shell electrons move to the inner shell. When they move, they emit energy. This energy has a specific wavelength of X-ray photon for each atom. An X-ray detector was used to detect the emitted X-ray photons. With the help of the X-ray detector, the existing elements of the film were identified. Before starting the measurement, the accelerated voltage was adjusted. The Ge-Se based Chalcogenide glass needs more than 10kV

accelerating voltage to knock out the outer shell electrons, which generates the specific X-ray wavelength for Ge and Se. In our experiments, 20 kV voltage was used to make sure that the mainstream of the generated electron beam had interacted with the sample. As a result, the accuracy of the experiment was increased. Likewise, a 10 mm distance was maintained to get the same strength of X-ray signal from each sample.

The primary purpose of performing the EDS study was to confirm the presence of the desired elements in the printed films. In the ChG ink making process, different solvents were used for two different methods. For the dissolution based ink making process, Amine was used to dissolve the ChG. On the other hand, Ethylene glycol and Cyclohexanone were used for the nanoparticles based ink formulation process.

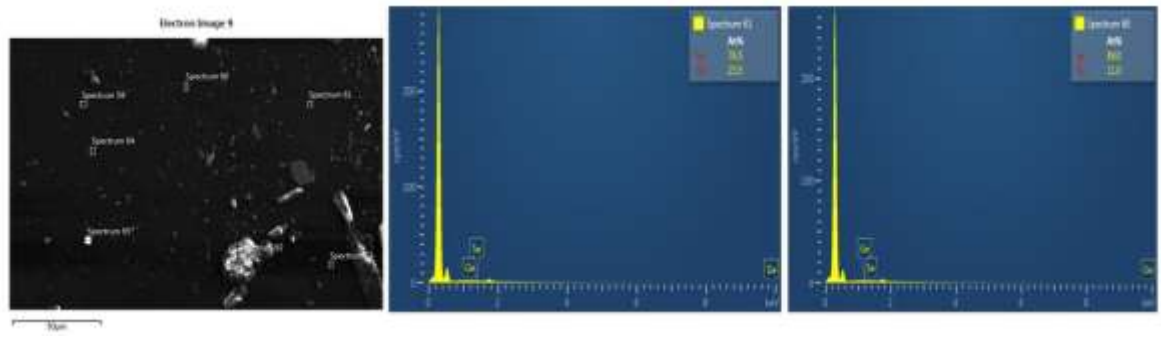

(a)

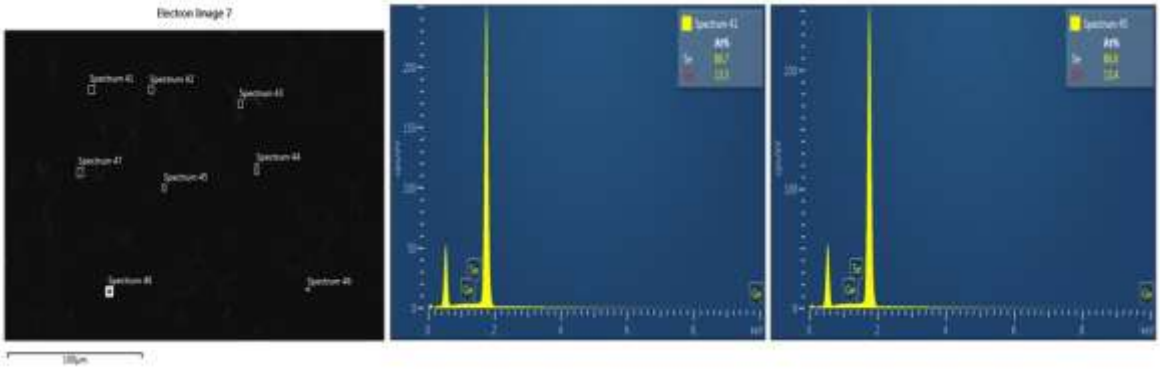

(b)

Figure 4.1 EDS for dissolution ink prepared $Ge_{20}Se_{80}$/Si printed film, a) EDA solvent,b) PA solvent.

After the sintering process, the solvent was evaporated, and only ChG remained in the film. With the help of the EDS study, the sintered printed film of ChG composition was compared with the bulk ChG composition. Several spots of the film were studied in order to get reliable compositional data, which were averaged overall measurements. Figure 4.1 presents examples of data for $Ge_{20}Se_{80}$ printed films obtained from solutions with different solvents.

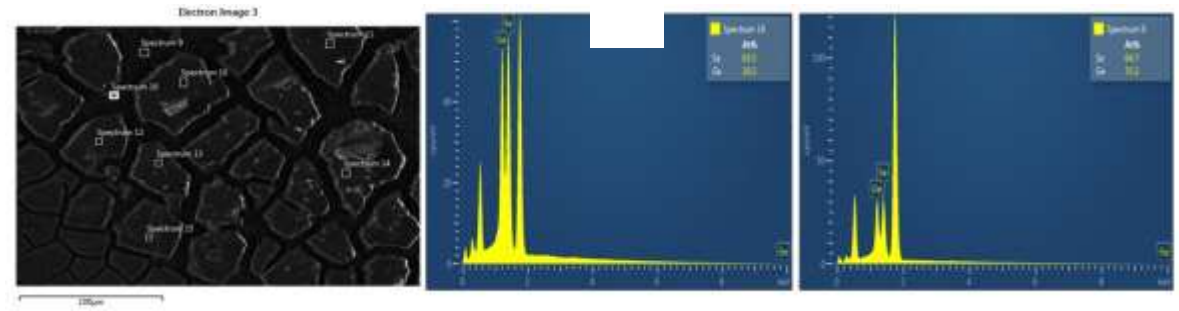

(a)

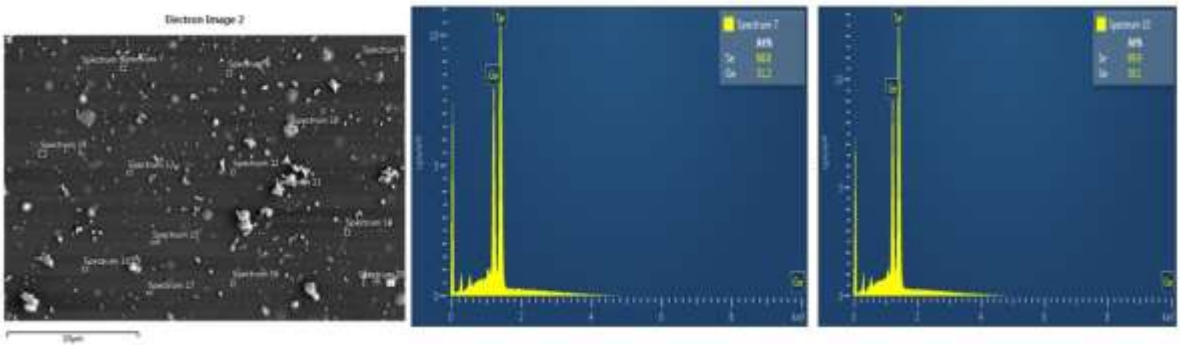

(b)

Figure 4.2 EDS for dissolution ink prepared $Ge_{30}Se_{70}$/Si printed film, a) EDA solvent, b) PA solvent.

Here, the other related elements like Si, O_2 were ignored during the EDS study in order to get an idea about the presence of the two most important elements of the films – Ge and Se. The data shows that for both dissolutions based printed films, the quantity of the elemental Ge was reduced compared to the bulk source materials. During the dissolution of the ChG in EDA and PA, a complex reaction occurs at which ionic bonding occurs between the Amine molecules and the chalcogenide glass clusters which leads for the formation of Germanium Alkile Ammonium Salts [11-15], which subsequently evaporates, but during the entire handling process of the films, it is possible to lose part of these salts, which contributes to the formation of films with reduced Ge concentration.

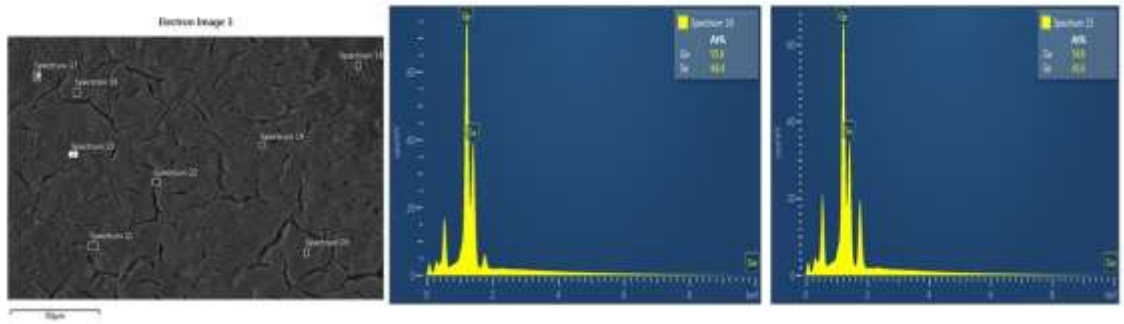

(a)

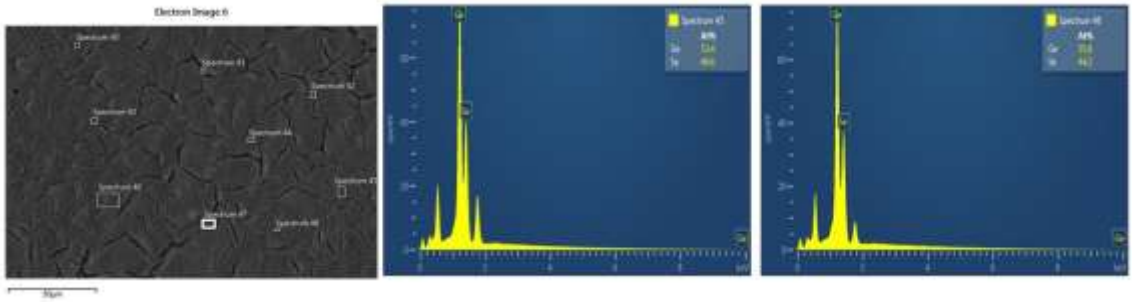

(b)

Figure 4.3 EDS for dissolution ink prepared Ge40Se60/Si printed film, a) EDA solvent, b)PA solvent.

The compositional results for the film based on $Ge_{30}Se_{70}$ films are shown in Fig 4.2. In this case, the EDA based $Ge_{30}Se_{70}$ printed film composition has ~1% variance from its bulk materials. On the other hand, the PA-based $Ge_{30}Se_{70}$ printed film distincts with 5-6% compared to the bulk material, which makes the film's compositional most close to the stoichiometric composition. Apart from this, the $Ge_{40}Se_{60}$ printed film also shows approximately 5-6% variance from the bulk source material, as presented in figure 4.3.

Table 4.1. summarizes the comparison between the bulk glass compositions and the printed film average composition. The multiple locations spectra provide sufficient data to get an average idea about the entire film composition.

Table 4.1 EDS data comparison between bulk and dissolution based printed films

Bulk composition	Average composition in the EDA solvent prepared film	Average composition in the PA solvent prepared film
$Ge_{20}Se_{80}$	$Ge_{13.9}Se_{86.1}$	$Ge_{17}Se_{83}$
$Ge_{30}Se_{70}$	$Ge_{30.7}Se_{69.30}$	$Ge_{36.8}Se_{63.2}$
$Ge_{40}Se_{60}$	$Ge_{45.4}Se_{54.6}$	$Ge_{44.8}Se_{55.2}$

Table 4.2 EDS data comparison between the bulk and nanoparticles based printed films

Bulk composition	Average composition in the nanoparticles prepared film
$Ge_{20}Se_{80}$	$Ge_{24.5}Se_{75.5}$
$Ge_{30}Se_{70}$	$Ge_{31.5}Se_{68.5}$
$Ge_{40}Se_{60}$	$Ge_{40.9}Se_{59.1}$

EDS was also used to check the composition of the nanoparticles based ChG printed thin film, an example of which are shown in Figure. 4.4.

Figure 4.4 and the summarized data on Table 2. point out that the nanoparticles based $Ge_{30}Se_{70}$ and $Ge_{40}Se_{60}$ printed films composition have only ~1% variance with its bulk counterpart, while the $Ge_{20}Se_{80}$ printed film demonstrates 8-9% different composition compared to the initial bulk material. This result is to some extend, random and needs a more detailed study, which, however, is not in the focus of this work, since it is mainly related to the study of inks formed by dissolution.

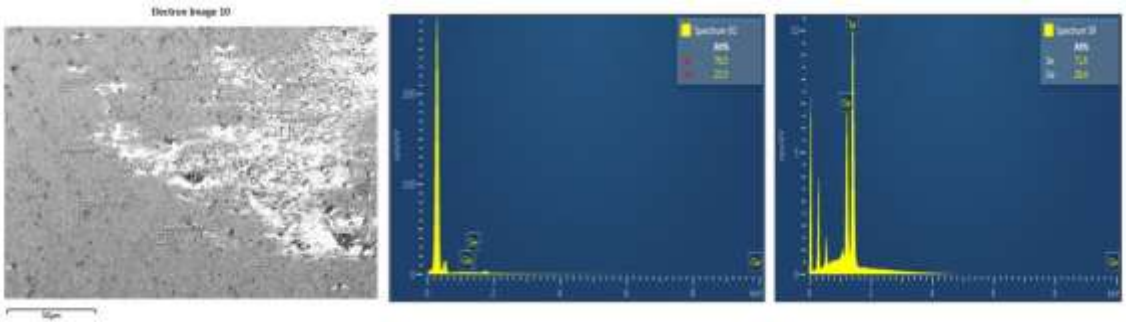

(a)

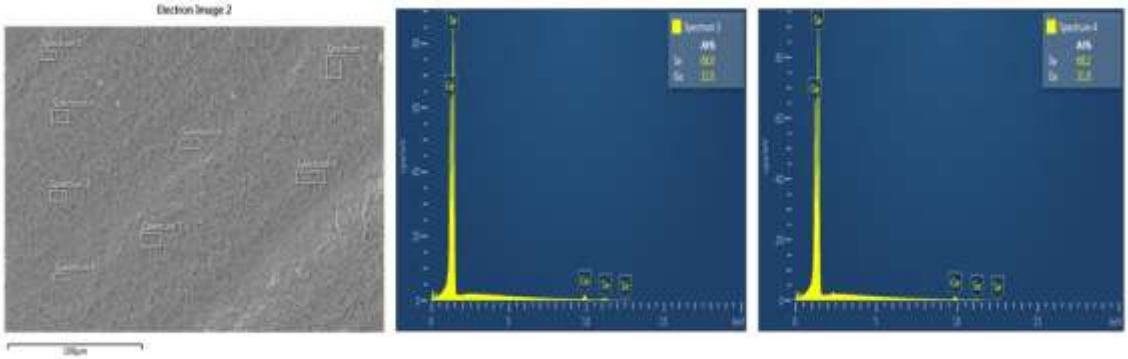

(b)

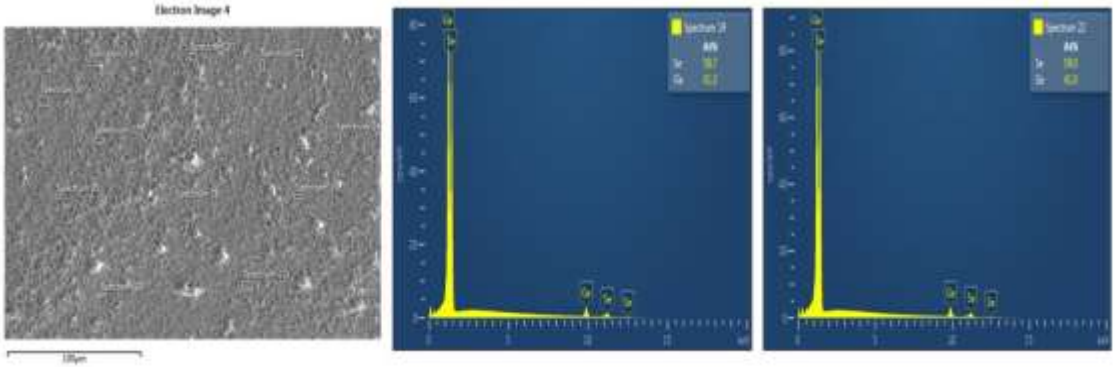

(c)

Figure 4.4 EDS for nanoparticles ink prepared a) $Ge_{20}Se_{80}$/Si, b) $Ge_{30}Se_{70}$/Si, and c) $Ge_{40}Se_{60}$/Si printed film.

EDS was also used to analyze the compositional changes in the materials of the printed film with different UV light radiation doses. The EDS data was collected from the

different areas of the same printed film, but it was not possible to take the data each time from the same spots. That's why the average compositional data was used for comparison. These results are summarized in Table 4.3.

Table 4.3 EDS data comparison between the average composition of the nanoparticles prepared films after sintering and average composition with different radiation doses.

Average composition in the nanoparticles prepared film	Radiation doses		
	40Wmincm^{-2}	80 Wmincm^{-2}	120 Wmincm^{-2}
$Ge_{24.5}Se_{75.5}$	$Ge_{23.7}Se_{76.3}$	$Ge_{23.9}Se_{76.1}$	$Ge_{24.3}Se_{75.7}$
$Ge_{31.5}Se_{68.5}$	$Ge_{30.9}Se_{69.1}$	$Ge_{30.7}Se_{69.3}$	$Ge_{30.4}Se_{69.6}$
$Ge_{40.9}Se_{59.1}$	$Ge_{40.9}Se_{58.71}$	-	-

Table 4.3 shows that, with different UV light radiation doses, the nanoparticles based ChG has very negligible changes in comparison compared to the non-irradiated printed film's composition.

During the irradiation condition, the printed film can be oxidized, as shown in Figure 4.5. The film oxidation measurement was performed to investigate this oxidation effect with different radiation doses. The main reason for the oxidation process is that during the UV light radiation, electron/hole pairs are created, which leads to the formation of dangling bonds in the printed film. They are highly reactive and can easily react with atmospheric Oxygen. Usually, the element which oxidizes is Ge [3,75-76]. There is one more detail that we can extract from the data shown in figure 4.5.

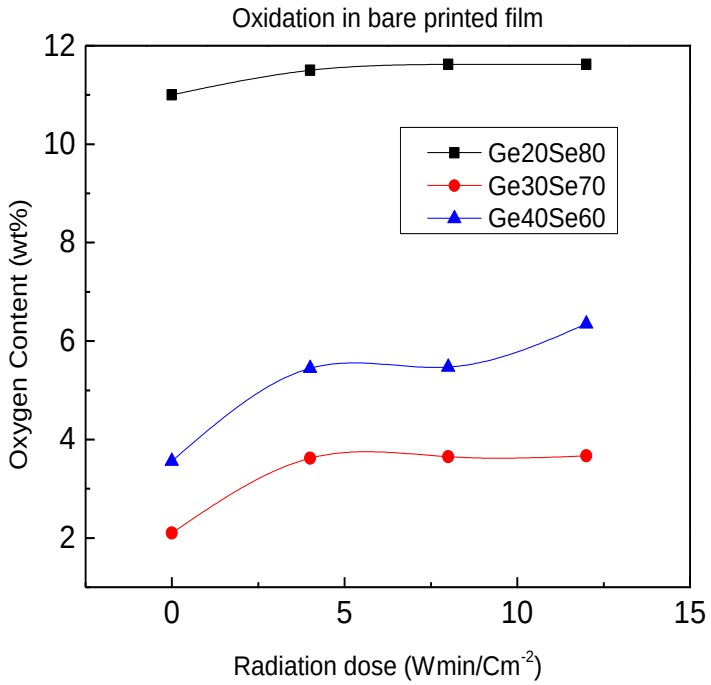

Figure 4.5 EDS study to quantifies the amount of oxidation in bare dissolution based printed films.

The less oxidizing films are those with $Ge_{20}Se_{80}$ composition. In essence, due to the high concentration of Se in them, one could expect that all Ge-Se bonds are chemically bonded, and because of this, after low initial oxidation saturation occurs and the process stops. With increasing Ge concentration formation of some wrong Ge-Ge bonds is possible, which has low bond energy and easily dissociate, due to which the oxidation process is more active but also saturate. In the $Ge_{40}Se_{60}$ composition formation of Ge-Ge bonding is naturally existing due to the formation of Ethane-like structural units, and this leads to a much more active oxidation process that does not saturate at high UV light irradiation. As reported in the Ge-S system, this oxidation process introduces serious composition transformation in the films and does not stop at their surface [77].

Atomic Force MicroscopyAnalysis

The Atomic Force Microscopy (AFM) technique is used for studying the roughness of the sample. A tip or probe is mainly interacting with the sample by following the raster scanning motion. During the scanning, the up/down and side motion of the tip is monitored by the laser beam, which is reflected from the tip. This reflected laser beam is captured by the position-sensitive photodetector (PSPD). The photodetector converts the scanning motion in terms of voltage. This work was performed in tapping mode condition to avoid the application of constant pressure, which can change the roughness of the printed sample. In the tapping mode, the tip is mounted on the shaker piezo, which provides the tip with the ability to oscillate between 100 Hz to 2MHz frequency.

All measurements were performed at the 0.5μm/sec rate with the oscillation frequency of 324 kHz using the Bruker Dimensions 3100 system with a Nanoscope IV controller. The ChG is a photo-sensitive material; that is why the AFM study was done in the dark at ambient temperature. With the help of the SPM software, the recorded AFM data is analyzed.

The AFM study of both printed films has been done to check the roughness with different UV light radiation doses. The overall trend of the roughness is an initial decrease for irradiation up to the 40 Wmin/Cm^{-2}radiation dose, after which it increases – Figure 4.6. We suggest that the reason for this effect is the fact that the printed films are quite rough, and the initial irradiation supplies the atoms with enough energy for them to adjust better in a more dense structure. Increasing the radiation dose further contributes to the processes discussed above – dangling bonds formation and oxidation, which

contributes to further increase of the surface roughness. There is an interesting effect if we compare the roughness of nanoparticles based films to dissolution based films. The first is much stronger affected by the irradiation, which we contribute to the less dens organization of the film's structure and the structural specifics of the nanoparticles films, which are formed by a combination of relatively big agglomerated structural units.

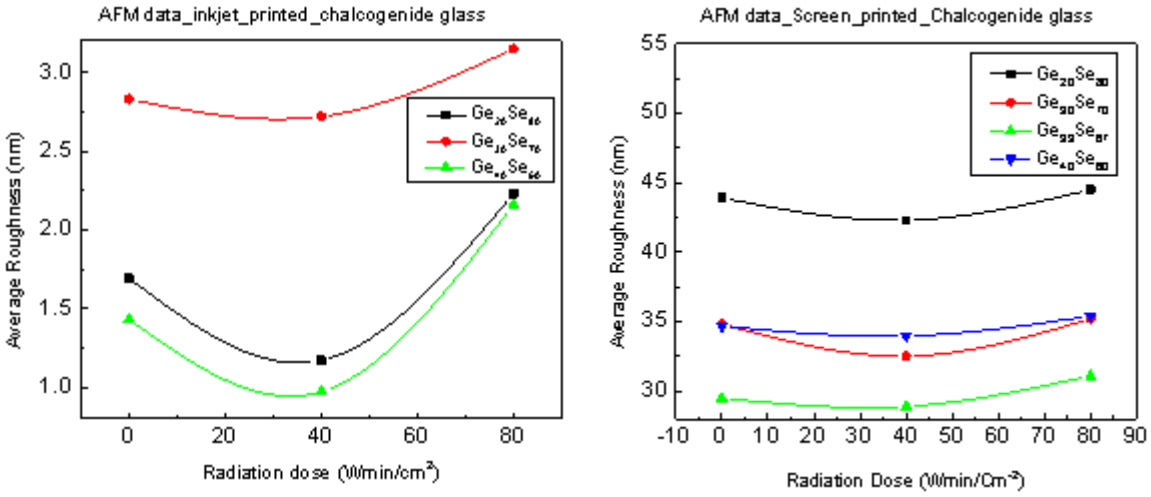

(a) **(b)**

Figure 4.6 AFM surface roughness analysis, a) dissolution based ink prepared printed film, b) nanoparticles based printed film.

Raman Spectroscopy Analysis

Raman spectroscopy was used to analyze the initial structure and the structural changes occurring in the printed material after irradiation with different doses, such as the bonding type, the physical structure, etc.

In this technique, the scattered light is used to measure the vibrational energy mode of the sample. When photon incidents onto the sample molecule, it may be reflected, absorbed, or scattered. Raman spectroscopy techniques mainly consider scattering events. During the interaction, the molecules may be elevated from the ground

vibration levels to a higher state called the virtual state. The energy of molecules does not change after interaction with the photon in most of the scattering events. In this case, the scattering photon and the incident photon have the same energy and wavelength. This is known as Rayleigh scattering [78-79]. When the energy of the molecules changes after the interaction, this type of scattering is called Raman scattering [78-79]. In the Raman scattering condition, the molecules gain the energy from the photon after the interaction; eventually, the photon loses its energy. This type of scattering is known as Stokes Raman scattering [78-79].

On the other hand, if the molecules lose the energy after the interaction with the photon, then the photon gains some energy, and its wavelength decreases. This type of scattering is known as Anti-stokes Raman scattering. Most of the molecules will be in the ground vibration state, and the Stokes scatter is the statistically more probable process. That is why Stokes Raman scatters are always more intense than Anti-Stokes. The resultant Raman spectra consist of a Gaussian peak, which corresponds to the scattering intensity of the specific structures. The intensity of each peak considers the number of each structure. The origin of the Raman scattering types is presented in Figure 4.7.

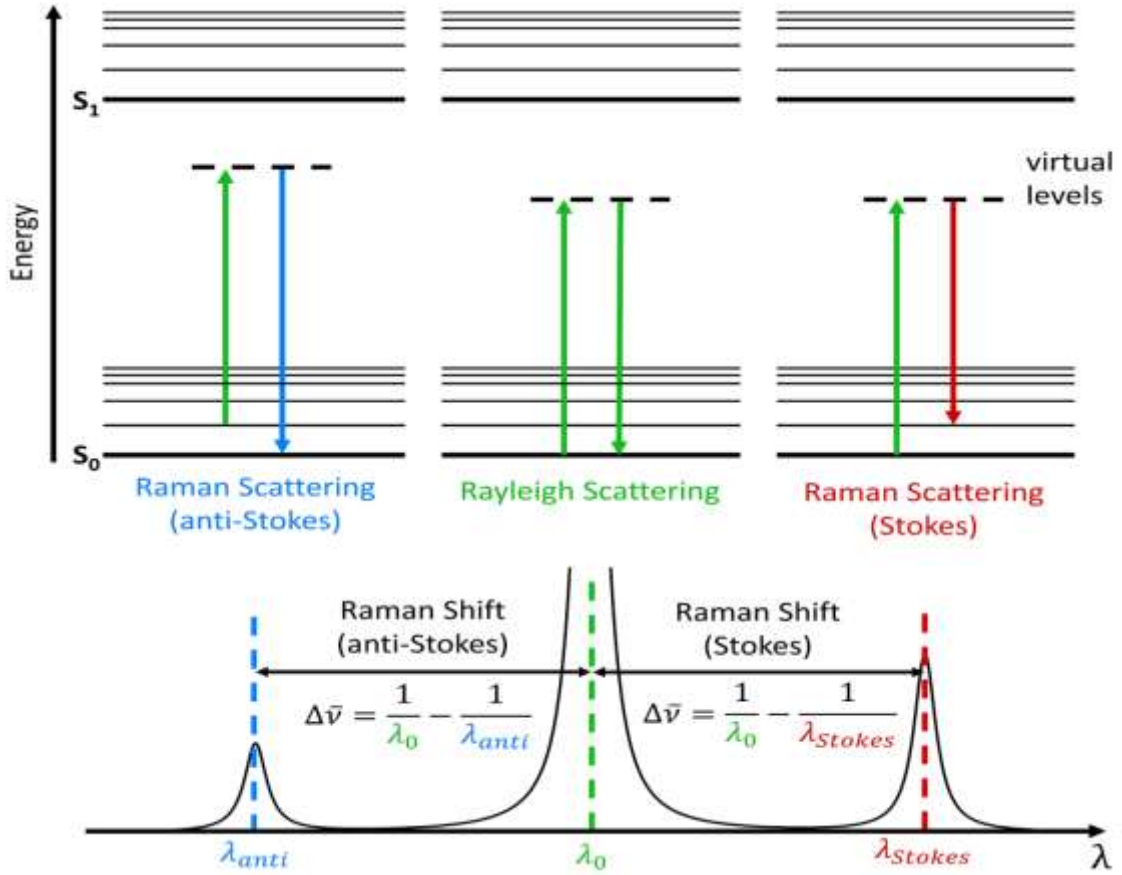

Figure 4.7 Jablonski Diagram showing the origin of Rayleigh, Stokes, and Anti-Stokes Raman Scatter [80].

Raman studies were performed using a Horiba Scientific Lab RAM HRE volution Raman Spectroscopic System in backscattering mode, using a parallel-polarized 442 nm He:Cd laser-focused to a spot of 6 μm using a 100x magnification, with a power of 120 mW. The samples were placed in an open atmosphere at the standard pressure and room temperature. To analyze the overall spectra, the baseline noise is removed by normalizing the spectra data. Three different compositions of Ge-Se based ChG nanoparticles based printed film were studied at different radiation doses using Raman spectroscopy.

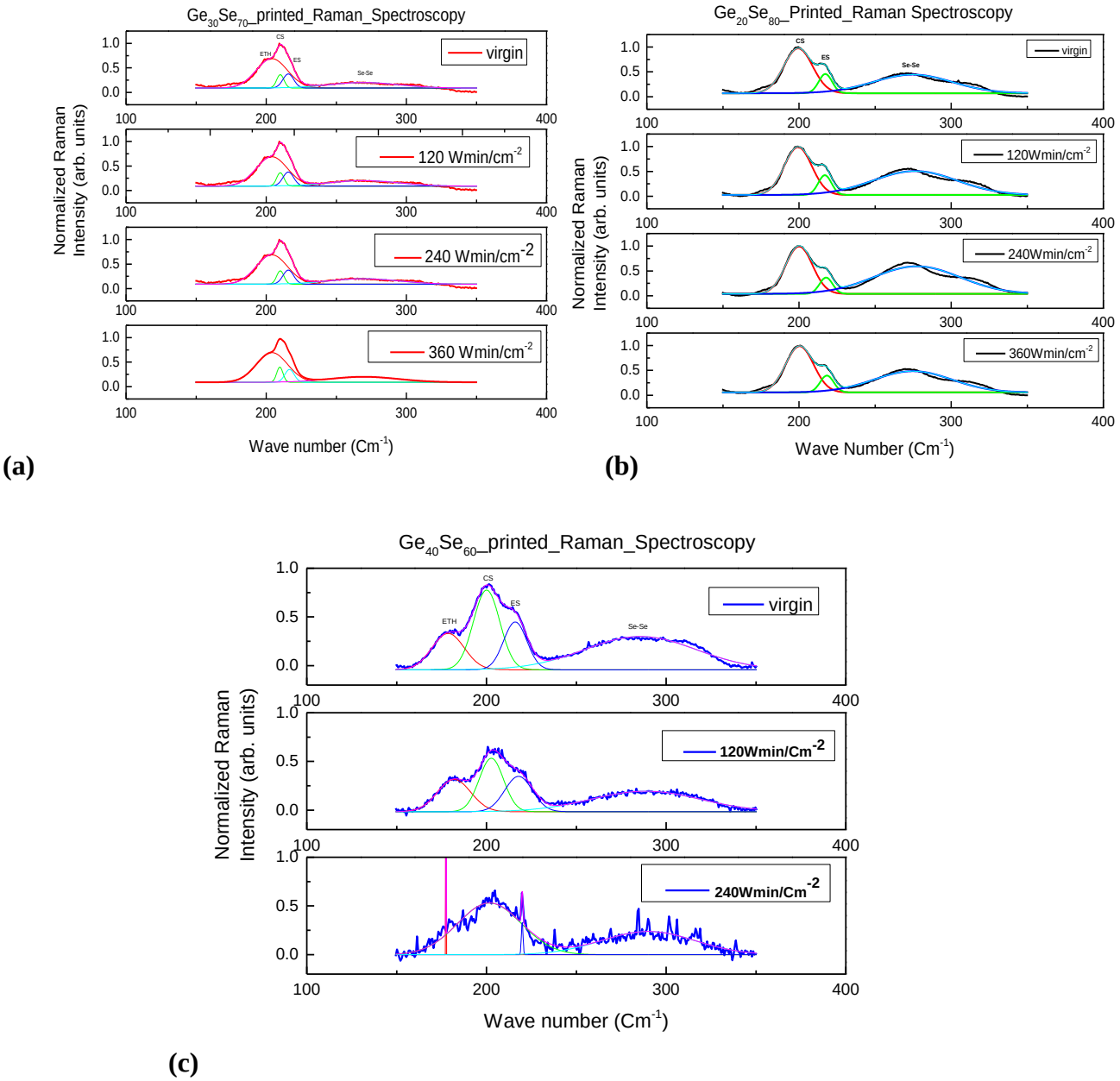

Figure 4.8 Fitted Raman spectra of virgin, and UV light irradiated Ge-Se based printed films, a)$Ge_{20}Se_{80}$,b) $Ge_{30}Se_{70}$, and c) $Ge_{40}Se_{60}$films.

The Raman spectra are presented in Figure 4.8. Raman spectra of the films of virgin and UV light irradiated with three different doses for $Ge_{20}Se_{80}$, $Ge_{30}Se_{70}$, and two different doses for $Ge_{40}Se_{60}$ films are displayed for all composition in Figure 4.8 (a)-(c). The Raman spectra demonstrate the availability of the standard tetrahedral structural

units for the chalcogenide glasses –the corner-sharing tetrahedral structures at 209 cm^{-1}, the Edge-sharing tetrahedral structures 218 cm^{-1} and the asymmetric Se-Se chain and rings are 268 cm^{-1} [74]. In Ge rich compositions ($Ge_{30}Se_{70}$, $Ge_{40}Se_{60}$) spectra, the Ethane like structure (ETH) raises with avibrational mode at 198 cm^{-1}. After calculation of the areal intensity under the specific vibrational mode, the dependence of the vibrational intensity of the most common structural units as a function of the irradiation dose has been presented in Figure. 4.9.

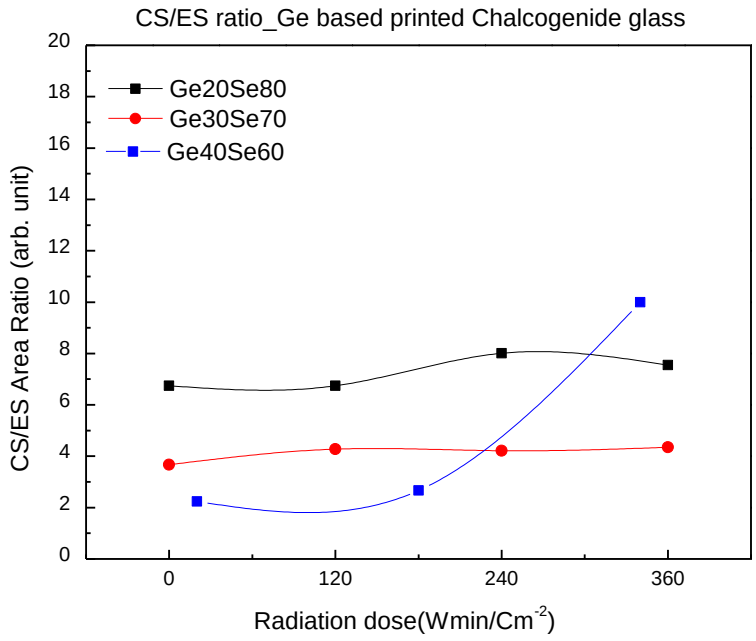

Figure 4.9 Analysis of Raman Spectra: CS/ES area ratio comparison.

Figure 4.9 shows the corner-sharing and edge-sharing ratio before and after irradiation, where the Se rich compositions did not show significant change due to different radiation doses. This is a film indication for the stability of these films towards electromagnetic irradiation and their suitability for application as a material for radiation

sensing. The only material which reacted with a relevant structural change on the irradiation was the Ge rich composition $Ge_{40}Se_{60}$.

The Raman spectra of the films obtained by the printing of films with inks based on ChG dissolution with amines are presented in figure 4.10 and figure 4.11.

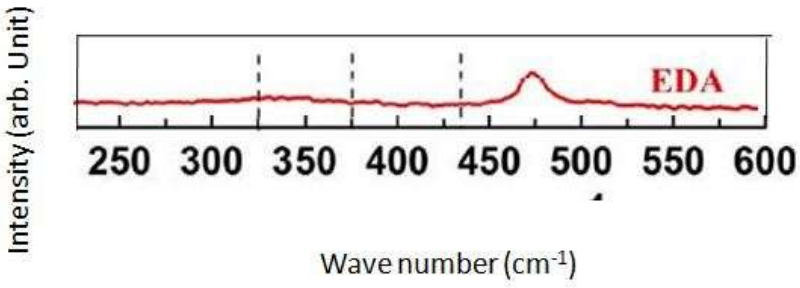

(a)

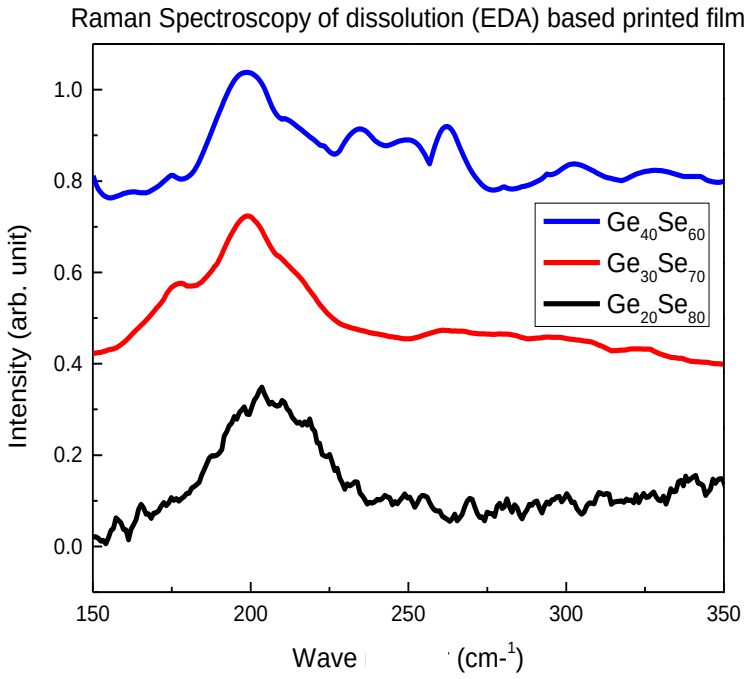

(b)

Figure 4.10 a) Fitted Raman spectra of EDA solvent[78] and b) Ge-Se based dissolution based printed films, $Ge_{20}Se_{80}$, $Ge_{30}Se_{70}$, and $Ge_{40}Se_{60}$ films.

The Raman spectra of the printed $Ge_{20}Se_{80}$, $Ge_{30}Se_{70}$, $Ge_{40}Se_{60}$ films are shown for all compositions and compared with their solvents in both figure 4.10 and 4.11. Four bands are easily distinguished by the wave number location in theses Raman spectra. Tetrahedral structural units for the ChG show corner-sharing at 200 cm^{-1}, Edge-sharing tetrahedral structures at 218 $cm^{-1,}$ and asymmetric Se-Se chain and rings are at 263 cm^{-1} [78]. Ethane like structure (ETH) shows only $Ge_{30}Se_{70}$ and $Ge_{40}Se_{60}$ composition at 190 $cm^{-1.}$

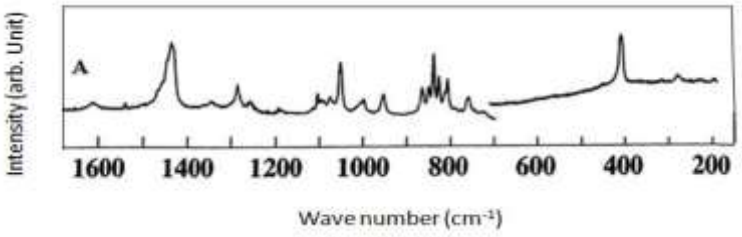

(a)

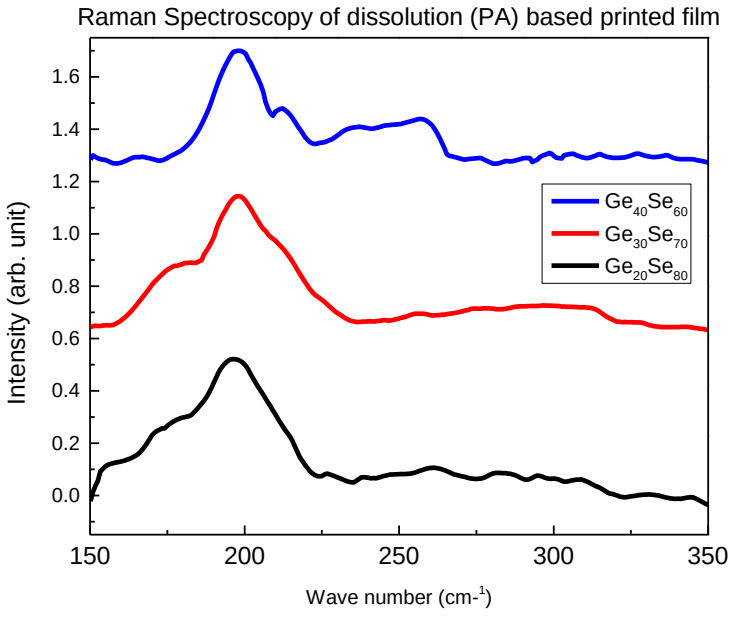

(b)

Figure 4.11 a) Fitted Raman spectra of PA solvent [92] and b) Ge-Se based dissolution based printed films, $Ge_{20}Se_{80}$, $Ge_{30}Se_{70}$, and$Ge_{40}Se_{60}$ films.

It is obvious that at the condition of the Raman study, the solvent is not completely evaporated, and its presence influences the film's structure, especially the EDA solvent. This effect is mostly expressed for the Ge rich $Ge_{40}Se_{60}$.

Discussion

The dissolution based printed films shows the compositional change in comparison with the bulk glass composition. There is a complex chemical reaction that occurs between the Chalcogenide glass composition and the Amine solvent during the dissolution process. The EDA solvent dissolved $Ge_{20}Se_{80}$ by the chelating process. In this process, two coordinate bonds are connected to the Ge molecules and form a ring-like center. As a result, the glass structure breaks and forms small structural units similar to a monomer. During the sintering process, they can be evaporated, and this is the main reason for the compositional difference between the source material and the chalcogenide film. However, the $Ge_{30}Se_{70}$ dissolution based printed film does not show any significant composition change. This composition is close to the stoichiometric composition and more stable due to the low number of wrong bonds in it.

More specifically, the PA solvent reacts with the ChG and forms the Germanium Alkylammonium group (RNH_2). The N atom from the Alkylammonium group has a nucleophile tendency because of its lone pair electrons. This group substitutes the Se atoms, and thus the dissolution process is in fact, the formation of a complex molecule with the Ge and the Se atoms residing in the solution [52,59]. At this dissolution process, some Ge atoms can be washed out by the solvent. It is for this reason that the films have a lower concentration of the Ge compared to the source material. Since the major chemical reaction at dissolution affects the Ge atoms in the films, naturally, the structure of the

$Ge_{40}Se_{60}$ films is mostly influenced by the presence of the solvent, which is clearly demonstrated on the Raman spectra, especially by dissolution with the EDA. In essence, because of the lower evaporation temperature of the PA, its concentration in the films is lower compared to the case when the EDA is used as a solvent.

For the nanoparticles based printed film, the $Ge_{30}Se_{70}$ and the $Ge_{40}Se_{60}$ do not show significant compositional differences compared to the bulk material. In the $Ge_{20}Se_{80}$ printed films, extra Se atoms create-Se chains. These Se-Se chains can evaporate during the sintering process. Because of this reason, the concentration of Se atoms in the nanoparticles printed films was reduced. The $Ge_{30}Se_{70}$ composition does not show significant changes due to the number of wrong bonds in this material.

The overall trend of the roughness increases with the radiation dose. However, in the initial radiation dose range, there is a decrease in the roughness for printed films. When UV light radiation is introduced to the nanoparticles printed film, the dangling bonds in the printed films are affected, and they break. Among these dangling bonds, Ge-Ge bonds are weaker and more reactive than the others. These Ge-Ge dangling bonds react with atmospheric Oxygen and form the Ge-O bonds [3]. These bonds are significantly shorter than the others, and the resultant film constriction will cause a decrease in roughness. After a certain point, Ge-O formation becomes saturated. However, the introduction of oxygen in the structure influence to a high extent the surface roughness due to the smaller size of the Oxygen atom, compared to the Se atom. Figure 4.6 shows that after 4 $Wmincm^{-2}$ radiation doses, the surface roughness increases. The saturation of the oxidation process during the irradiation is also indicated in Figure 4.5.

The ES/CS ratio of nanoparticles printed films shows that there are no significant changes that occur during the irradiation condition for the Se rich composition (Figure 4.9). Table 4.3 data also proved that the composition of Se rich Chalcogenide glass printed film does not change the composition with different radiation doses. Among the studied films, the $Ge_{40}Se_{60}$ composition shows the lowest stability towards electromagnetic irradiation, and we suggest that the major reason for this is the existence of Ge-Ge bonding in it. This bond is very weak, it can be easily dissociated, which results in the formation of very active Ge atoms ready to react with the surrounding chalcogenide matrix and changing the structure of the materials of forming Oxide by reaction with environmental Oxygen.

It is possible to get better quality dissolution based printed film by improving sintering conditions to evaporated solvent completely. The experiments reported in this thesis were limited by the fact that we could not use Ar purged atmosphere for conducting the sintering at a higher temperature and carried out the sintering up to the temperature available in the vacuum furnace.

CHAPTER 5: DEVICES PERFORMANCE TEST

Devices Fabrication

The ChG printed films were used to fabricate the radiation sensing device using AM technology. Ag has high diffusivity in the Ge-Se based ChG. That's why Ag electrodes were fabricated on the ChG printed film. Figure 5.1 shows the cross-sectional view of the radiation sensor. The diameter of each Ag electrode was 2mm, and the space between the two electrodes was 1 mm. The device conductivity was measured in real-time between the two electrodes on the ChG surface at the irradiation condition.

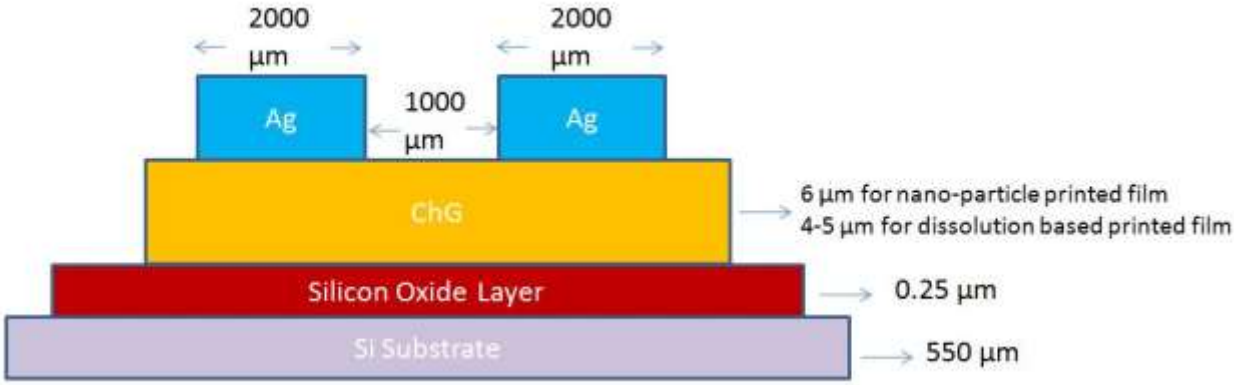

Figure 5.1 The cross-sectional view of the radiation sensor.

For device fabrication, the ChG layer was printed by ChG ink using different kinds of printers. The printing process with both types of ink was described in Chapter 4. The devices were fabricated by printing two electrodes on top of the ChG printed film. The DuPont 5000, a commercially available Ag conductive ink was used for this fabrication process. The viscosity range of the ink is 3500-16000cP. The nScrypt micro-dispense printer was used to fabricate the Ag electrodes. First, the Ag paste was filled

into the dispensing syringe under the fume hood by minimizing the amount of trapped air. It was confirmed that there was no air in the dispensing syringe. Two O-rings, a valve rod, and a tip (125 µm) were installed inside the valve body. Then, the valve body was installed into the dry pump assembly using a threaded adapter. In the end, the dispensing syringe was connected to the valve body to ensure the ink flow. Before starting printing, the printing speed, air pressure, and valve opening were optimized. The substrate was placed on the printing stage, and it was taped on before printing to keep the flatness of the surface and no movement during printing. The speed varied from 4-10 mm/sec with a 0.09 mm valve opening at 5 PSI pressure. After experimenting with different deposition speeds, a continuous line and excellent resolution were obtained at 8 mm/sec speed. The upped monitor observed the flow of the Ag paste. Then, the electrode printing pattern CAD file was loaded using the printer software. The printing pattern was verified by a dry run. After verification of the printing pattern, the status of the dry run was changed from true to false. Then, the print was initiated.

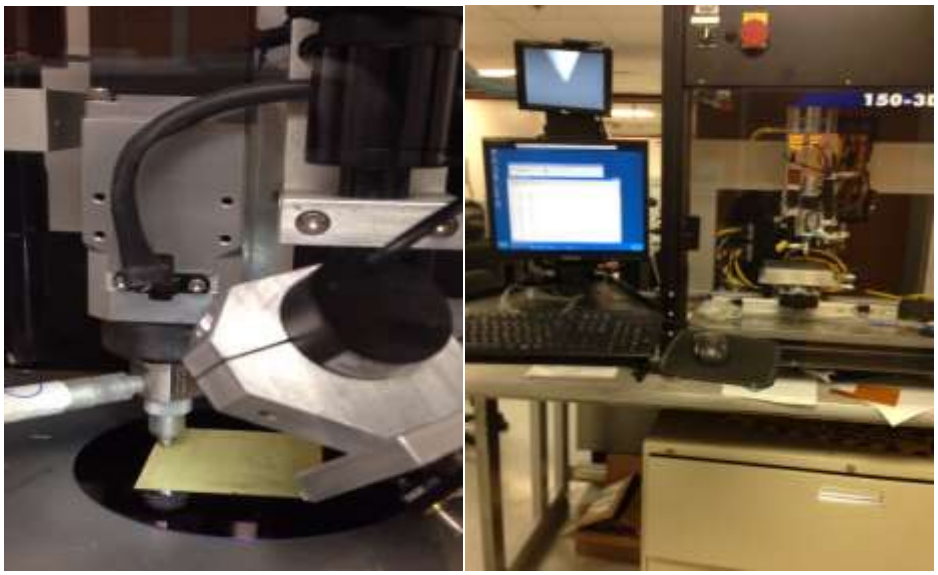

Figure 5.2 a) The parameter optimization of the nScrypt printer, b) printer in operation.

According to the vendor recommendation, the sintering of the Ag printed film had to be conducted at 100^{o}C for about 8-10 min. Although the sintering time is quite short, because of concerns that the high temperature should initiate Ag diffusion in the ChG film, this procedure was not followed, and experiments with the sintering of the films were carried out in order to optimize this process. The other option which could be utilized was to apply photonic sintering. It has been avoided as well since the wavelength at which it occurs would cause Ag photodiffusion within the ChG films. The printed electrodes on the ChG layer were self-sintered at room temperature within 48 hours in a vacuum furnace. After the sintering process finished, the conductivity of electrodes was measured using a probe station. Two probes were placed on the same electrode and were swept between 0V to 1V, where the compliance current was 50nA.

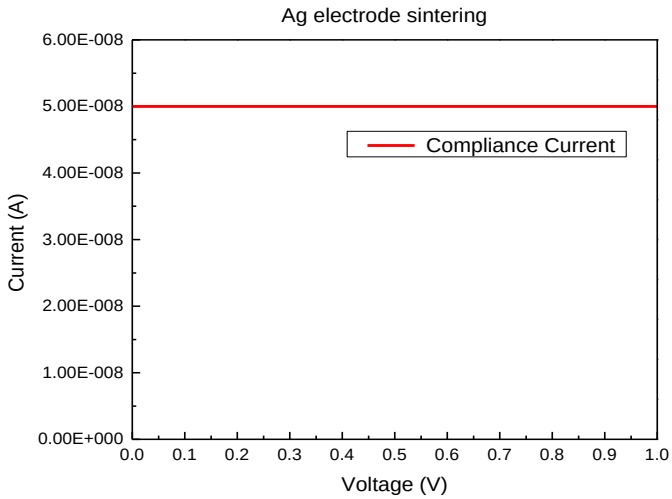

Figure 5.3 Ag electrode sintering test output.

Figure 5.3 shows that the output current was the same as the compliance current. That means that the resistance was zero for that specific electrode, and it became fully

conductive, which is a sign that the sintering process has been successful. A general view of different types of devices is shown in Figure 5.4.

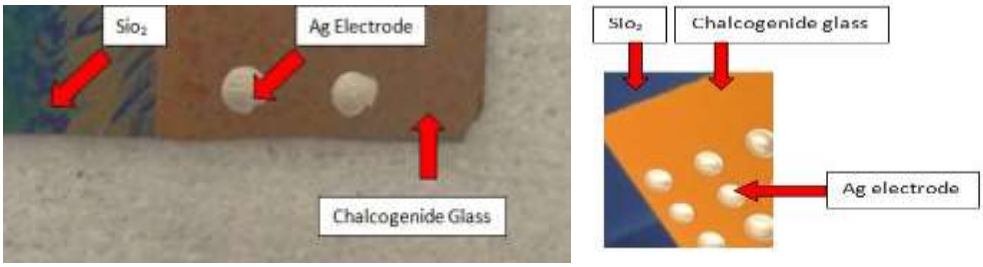

(a) **(b)**

Figure 5.4 The printed radiation sensor, a) dissolution based ink fabricated device, b) nanoparticles based ink fabricated device.

Devices Performance Testing

Since the studied devices are supposed to perform under electromagnetic irradiation, the proof of concept for their performance was achieved by irradiation with UV light. The devices were tested using a 4 Wcm^{-2} UV light irradiation source. The conductivity at different UV light radiation doses was measured using an HP 4146 semiconductor parameter analyzer applying a DC voltage sweep and the probes contacting two adjacent Ag electrodes. The entire measuring station was isolated from any external noise or light source using a Faraday cage – Figure 5.5.

Figure 5.5 Devices test setup.

The device test parameters are shown in Figure 5.6.

Figure 5.6 Devices test parameters.

Figure 5.7 shows examples of two real-time $Ge_{30}Se_{70}$ screen printed device performances, observed at 40Wmincm^{-2}-120Wmincm^{-2} radiation doses. The current of the devices increased with the rise of the radiation doses up to four orders of magnitude compared to the control device current. The control or virgin devices were not exposed to UV light radiation. Irradiation with UV light causes several processes to occur in the studied systems. On the one hand, it causes the formation of electron-hole pairs in the ChG films, which form a kind of electrical field within these films. On the other hand, the light irradiation ionizes the Ag in the electrodes, and this causes massive diffusion of the Ag^+ driven by the internal field within the ChG films. This effect is well studied and documented [4-8]. The presence of Ag^+ creates donor levels in the bandgap of the ChG films, which effectively decrease its bandgap [3,81]. Therefore the conductivity increases. As a secondary effect, because of the high affinity between Ag and Se

chemical interaction between them occurs, by which binary Ag_2Se or ternary Ag_8GeSe_6 compounds can form [5,8,81]. As much as this is the basic effect occurring at the radiation of Ge-Se films, there are fluctuations in it related to specific events occurring at particular irradiation and partial oxidation of the films. So, for example, at further increasing of the irradiation dose to 160Wmincm^{-2} the measured conductivity decreases, as shown in figure 5.7. We suggest that the reason for this is an enormous increase of the electron-hole pairs, which due to their close proximity recombine immediately, their number substantially decreases, and so the effect described above is suppressed. Simultaneously with this partial oxidation of the films occurs, which reduces their conductivity as well. Based on these two effects, both types of studied devices could be detected 0-120 Wmincm^{-2} range radiation.

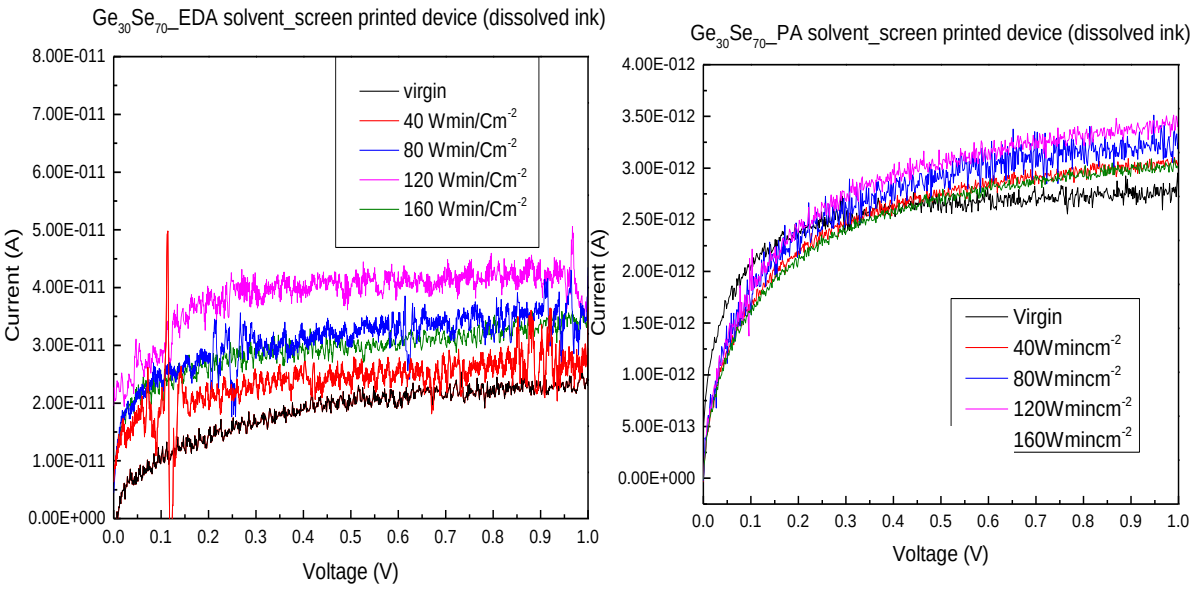

(a) **(b)**

Figure 5.7 $Ge_{30}Se_{70}$ screen printed device performance, a) EDA solvent device, b) PA solvent.

Figure 5.8 shows the performance of two $Ge_{20}Se_{80}$ screen printed devices. There is a principle difference in the performance of the devices dissolved in PA and those dissolved in EDA. For the PA solvent fabricated devices, the current increases after the initial dose of UV light exposure. At the further increase of the UV light illumination time, the current remains constant. In essence, this effect is pretty close to the one described for the $Ge_{30}Se_{70}$ base devices with the difference that the saturation occurs much faster due to the availability of excess of Se wrong bonds in the $Ge_{20}Se_{80}$ composition. Because of this, the generation of the electron-hole pairs is fast; their number is high; they are in close proximity and recombine fast. As a result, the Ag diffusion into $Ge_{20}Se_{80}$ is restricted.

On the other hand, for the EDA fabricated devices, after exposure with UV light, the current decreases. As it has been already reported in chapter 4, there are solvent residuals in the EDA dissolved films, which might be the cause of this result. No current changes occur at further exposure with UV light, and the results overlap.

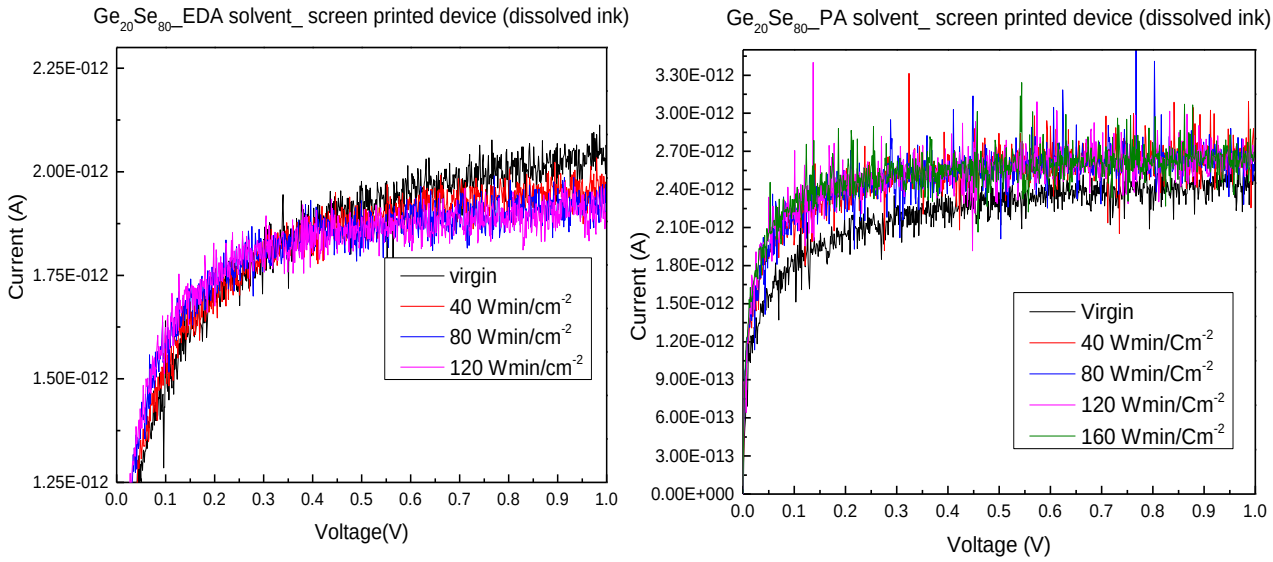

(a) **(b)**

Figure 5.8 $Ge_{20}Se_{80}$ screen printed device performance, a) EDA solvent device, b) PA solvent.

Figure 5.9 shows the performance of two $Ge_{40}Se_{60}$ printed devices. For the PA solvent fabricated device, the current remains constant after UV light exposure independently of the irradiation doses. We suggest that the main reason for this is the lack of Se wrong bonds in this composition and availability of Ge-Ge bonding in it. The Ge-Ge bonds have the lowest bonding energy and undergo dissociation at light irradiation by which immediate reaction with the environmental Oxygen and eventually existing Se wrong bonds and some regrouping of the Se tetrahedra occurs, which, however, do not contribute to increase in the devices' conductivity.

For EDA fabricated device, the current decreases after exposure of UV light due to residual materials into the printed films. Further exposures with UV light do not cause any changes in the devices' performance.

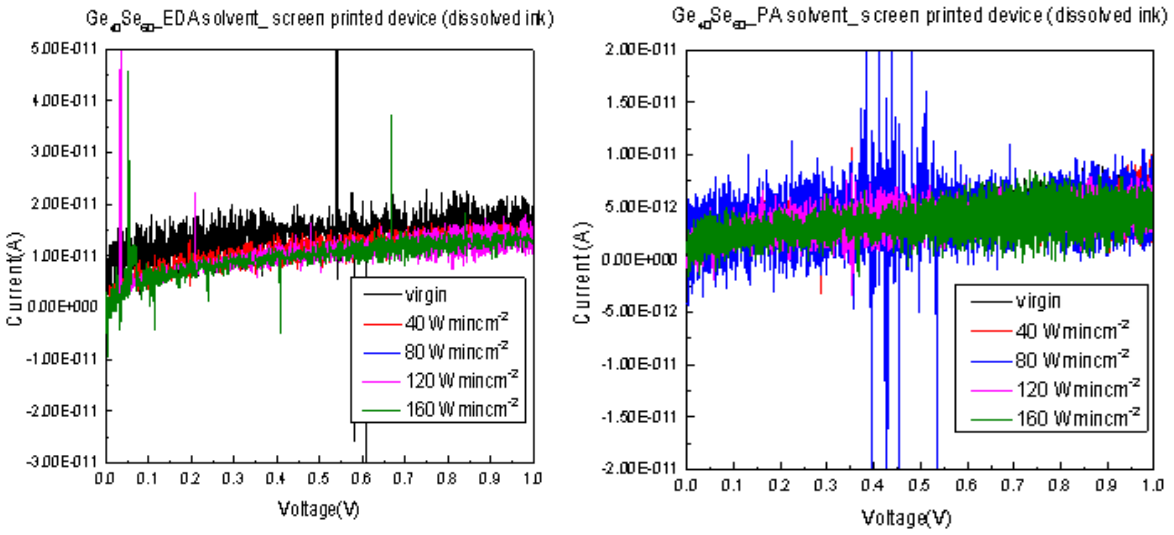

(a) **(b)**

Figure 5.9 $Ge_{40}Se_{60}$ screen printed device performance, a) EDA solvent device, b) PA solvent.

Figure 5.10 shows the nanoparticles ink fabricated devices' performances at different radiation doses. In comparison with the dissolution based ink fabricated $Ge_{20}Se_{80}$ and $Ge_{30}Se_{70}$ devices, the nanoparticles based devices of the same composition show the same characteristics. However, the nanoparticles devices have a wider range of sensing capability in comparison with the dissolution based printed devices. Though the thickness of both types of printed films is almost the same, the amount of the ChG material in the dissolution based printed devices is much less. As a result, the electron-hole pair generation due to the UV light exposure and all other supporting effects develop in a much more limited extent.

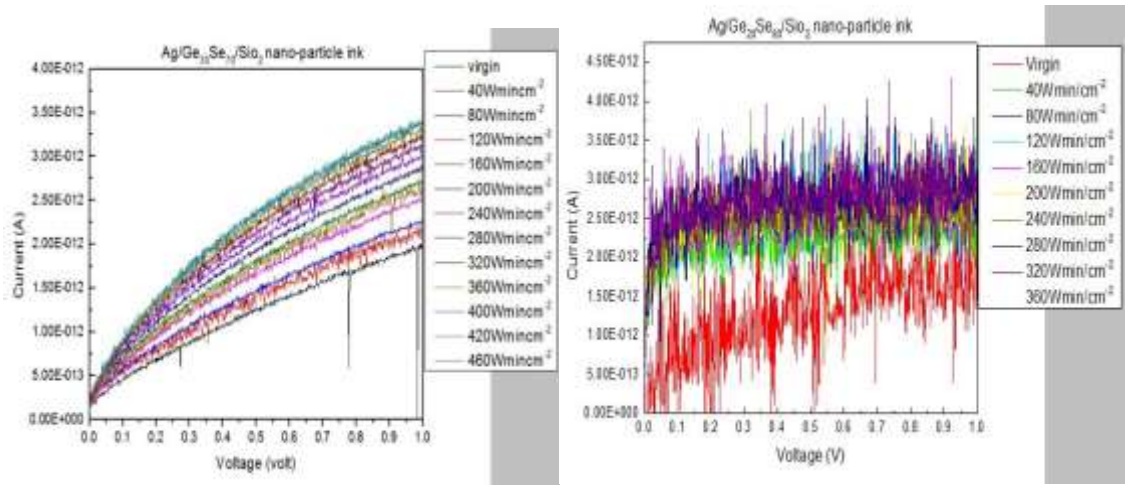

(a) **(b)**

Figure 5.10 a) $Ge_{20}Se_{80}$ inkjet printed device performance, b) $Ge_{30}Se_{70}$ inkjet printed device.

Figure 5.11 shows the $Ge_{40}Se_{60}$ nanoparticles ink fabricated devices' performance at different radiation doses. Initially, after exposure to the UV light, the current increases. Then, at further illumination with the 80Wmincm^{-2} to 120Wmincm^{-2} radiation doses, the current decreases. Which we suggest is a result of the initial electron-hole formation and a further rigidity occurring in the material.

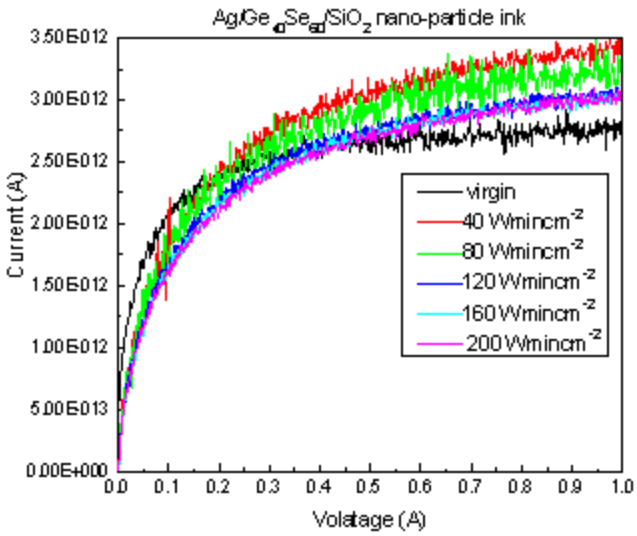

Figure 5.11 $Ge_{40}Se_{60}$ inkjet printed device performance.

The effects exhibited in the electrical performance of the devices are also confirmed by the surface observation of the devices. Figure 5.12 shows the unirradiated sample, which consisting of two Ag electrodes on the ChG on a 2 mm distance. Increasing the exposure dose to 360Wmincm^{-2} resulted in a small diffusion distance. At further irradiation to 720Wmincm^{-2} dose, the diffusion distance for each of the electrodes is 0.5 mm, and the electrodes are almost shortened.

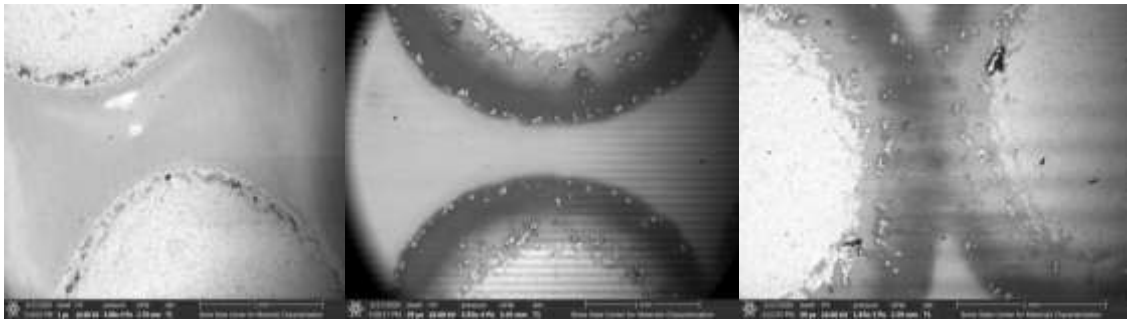

(a) (b) (c)

Figure 5.12 SEM pictures of Ag diffusion with different radiation doses, a) before radiation, b) after 360Wmincm^{-2} radiation doses, c) after 720 Wmincm^{-2} radiation doses.

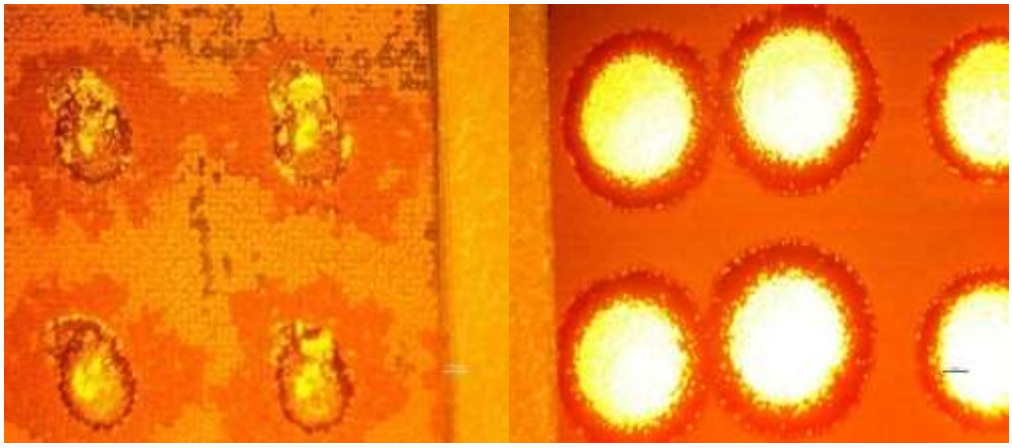

(a) **(b)**

Figure 5.13 Ag diffusion, a) dissolution based device, b) nanoparticles based device.

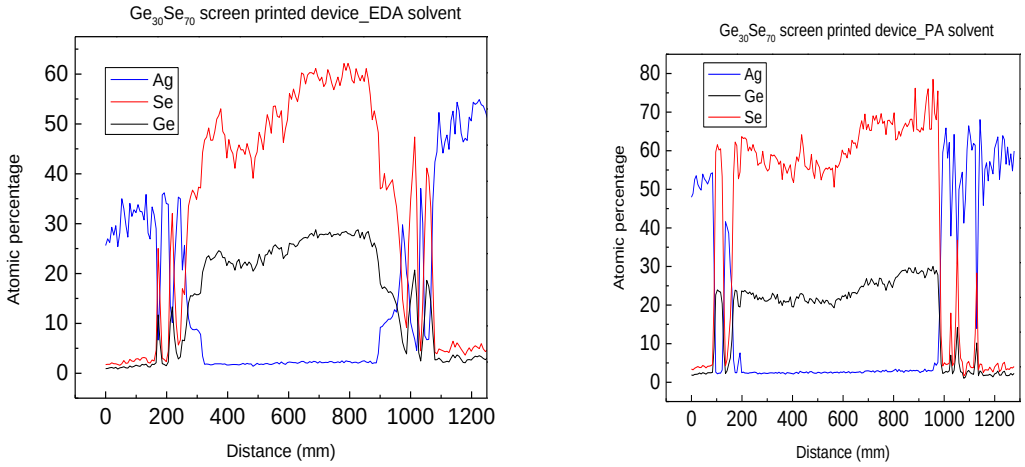

(a) **(b)**

Figure 5.14 Line scan EDS data of film composition for a)EDA solvent device, b) PA solvent device.

The EDS data confirms that the atomic percentage of Ge and Se is lower than in the bulk ChG composition. In the dissolution process, the Alkylammonium group from the solvent attracts the lower electron density Ge atoms. The nucleophilic N atom from the solvent pulled away electrons from Ge atoms, which increases their susceptibility

towards reaction with other elements or groups. During this chemical reaction, the Se atoms are substituted by the Alkylammonium group, and the terminated Se reacts with the excess Hydrogen to form a terminated Hydrogen Selenium group. After this complex chemical reaction, some of the Ge and Se atoms are evaporated during the sintering process. The atomic percentages of the elements were not stable in the printed film. In the films prepared materials by dissolution, there are clearly presented higher Ag concentrations around Se electrons after applied irradiation.

Figure 5.15 shows the EDS data for composition development between the two electrodes in the nanoparticles devices. The atomic percentages of the Ge and Se in the devices are almost the same as for the bulk ChG. This graph clearly shows some Ag diffuses between the two electrodes on a 1 mm distance at 160 $Wmincm^{-2}$ doses of irradiation. The molecular composition of the Ag diffused devices was studied by the XRD spectroscopy. Figure 5.16 shows the Ag containing binary and ternary products forming after Ag diffusion in the nanoparticles printed devices at different UV light radiation doses at room temperature.

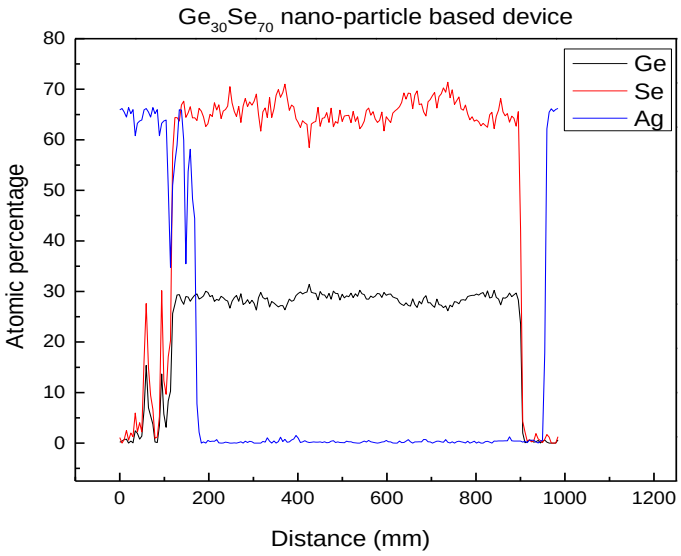

Figure 5.15 Line scan EDS data of nanoparticles based devices.

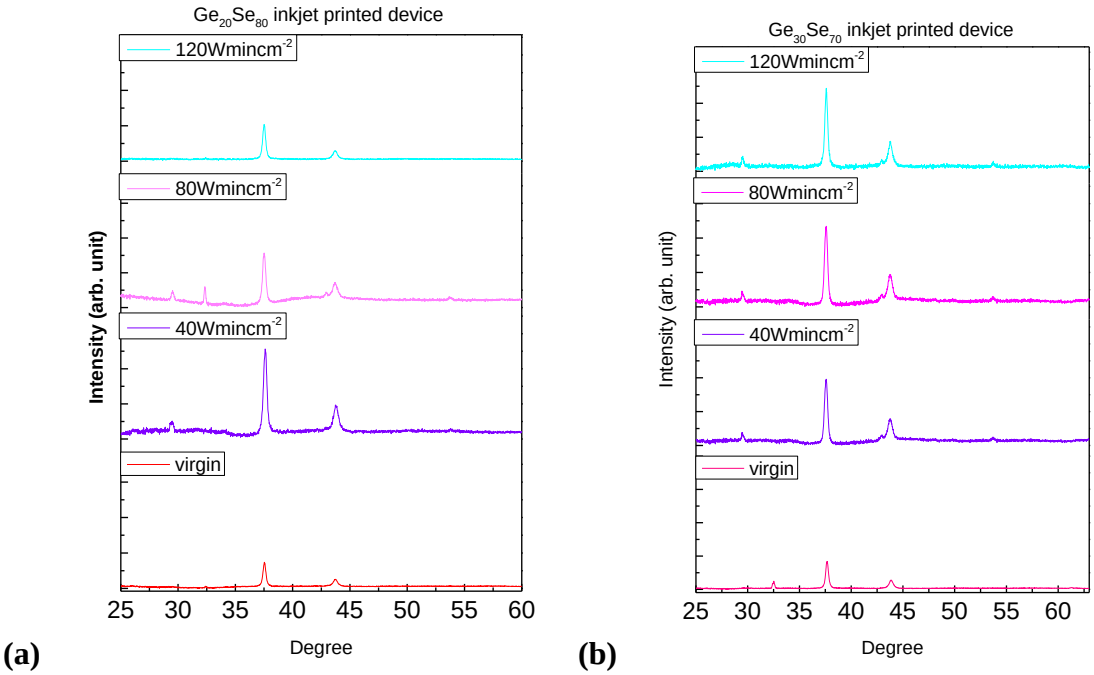

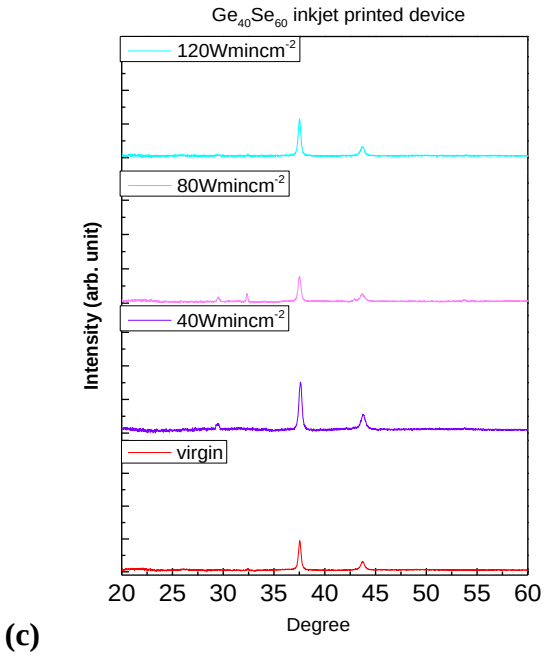

(c)

Figure 5.16 XRD spectra measured at different radiation doses for a) $Ge_{20}Se_{80}$, b) $Ge_{30}Se_{70}$, and c) $Ge_{40}Se_{60}$.

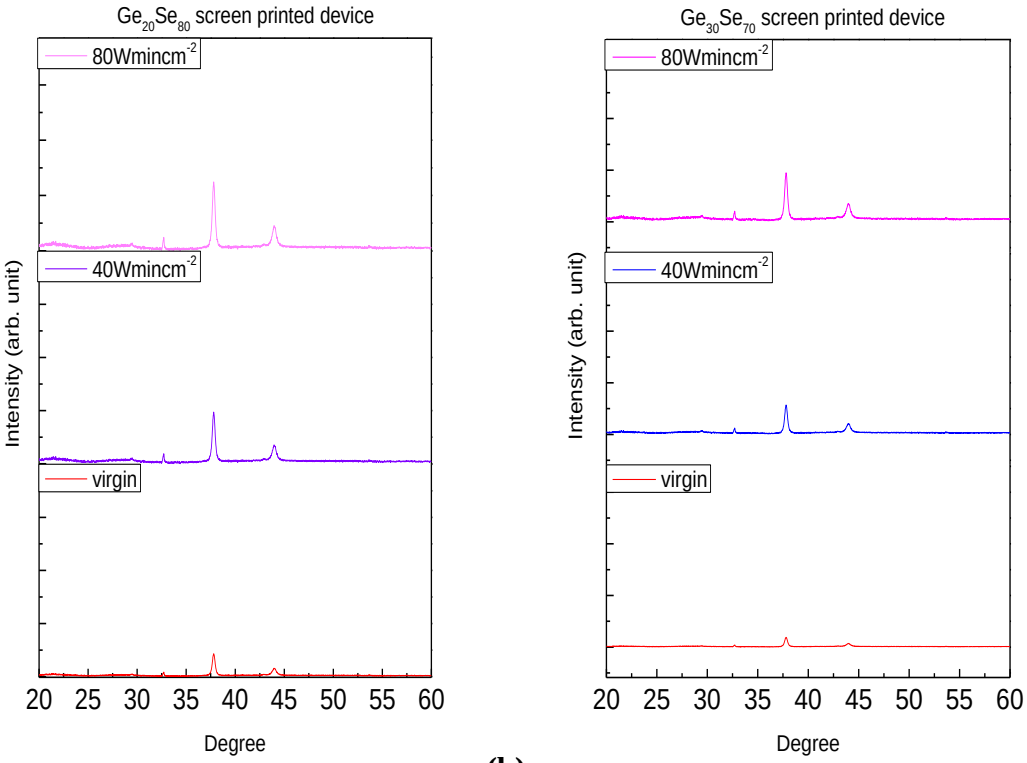

Figure 5.17 XRD spectra measured at different radiation doses for a) $Ge_{20}Se_{80}$, b) $Ge_{30}Se_{70}$, and c) $Ge_{40}Se_{60}$.

There are two specific Ag containing binary and ternary product observed at 2θ = 38° for α-Ag_2Se (JCPDS cards 27-0619) and 2θ = 45° for Ag_8GeSe_6 (JCPDS cards 71-190). These Ag containing products highly contributed to the change in conductivity of the studied devices.

Figure 5.17 shows the XRD data for the three Ag diffused screen printed devices at different radiation doses. The two specific phases - the α-Ag_2Se and Ag_8GeSe_6 products are identified in the XRD data. For both devices, there are crystal peaks of Ag_2Se and Ag_8GeSe_6 in the virgin device as well. In comparison with the inkjet-printed device XRD data, the intensity of Ag containing molecular composition in the screen-printed devices is lower. The growth rate of these specific phases depends on the composition of the film, as well as the exposure to the radiation doses, and as shown, the XRD results are in close similarity with all previously submitted data regarding the inclusion of Ag into the films.

Besides the UV light radiation source, the $Ge_{30}Se_{70}$ nanoparticles printed devices were exposed to the Xe ion radiation at different doses. Figure 5.18, shows the current development at irradiation from 200KeV to 600KeV. During this radiation exposure time, the Ag diffused into the ChG printed film and created binary and ternary products. The curves presenting the current are pretty noisy since the current is quite low. However, the tendency is pretty clear, and it follows the current development presented for the UV irradiated devices with the same origin as presented in Figure 5.10.

The devices regarded so far are non-reversible since once Ag diffusing between the two Ag electrodes cannot be collected back out of the ChG film. However, if one of the electrodes is built up by electrochemically inert material, for example, Ni, the

electrochemical reaction, and related to its movement of the Ag ions can be directed by the electrical bias applied between the two electrodes towards the Ag, or the other electrode. One additional opportunity for widening the application of these devices is to deposit them on a flexible substrate, which will give a chance the devices to be included in clothing or adhered to non-flat surfaces. To demonstrate this, the devices were printed over a Kapton substrate and contained one Ag and one Ni electrodes.

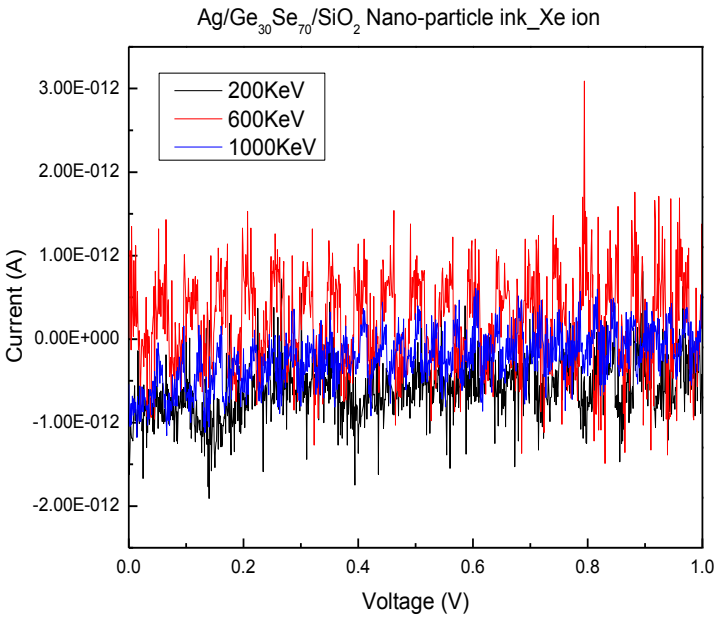

Figure 5.18 $Ge_{30}Se_{70}$ inkjet printed device performance at a different dose of the Xe ion.

Figure 5.19 shows a cross-sectional view of the reversible radiation sensor on a flexible substrate. These devices were fabricated by following the same method that was described at the beginning of this chapter. However, instead of two Ag electrodes, they were fabricated using an Ag electrode and an electrochemically inert Ni electrode at a 1 mm distance. The pyroduct 598C, commercially available Ni ink was used for printing the Ni electrode using the nScrypt printer. The pyroduct 598C Ni ink was self-sintered.

These devices were also tested using the same conditions and the same 4 Wcm^{-2} UV light radiation source at different radiation doses.

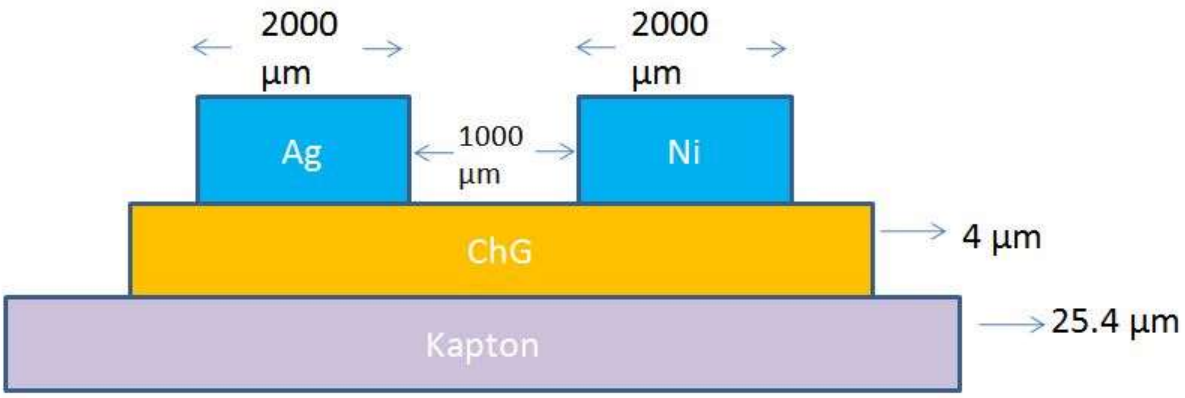

Figure 5.19 The cross-section view of the reversible radiation sensor.

A closer look at the reversible sensor is presented in Figure 5.20.

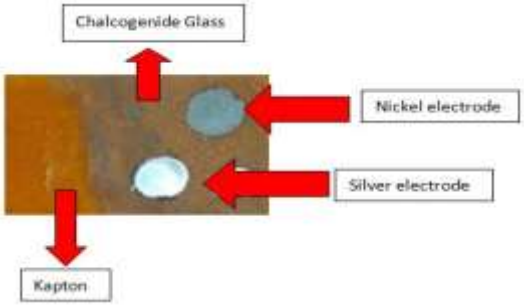

Figure 5.20 $Ge_{30}Se_{70}$ printed reversible radiation sensor.

The probes were placed on adjacent Ag and Ni electrodes, whereas the Ag electrode was positively biased, and the Ni electrode was negatively biased. Then, the current between two electrodes was measured using a semiconductor parameter analyzer using a DC voltage sweep 0 to 3 Volt.

Figure 5.21 shows that the current through the device increases after irradiation with different radiation doses, similar to the devices with two Ag electrodes. This device can be reversed by changing the polarity of the electrodes. For this again, a 3 Volts DC

was swept between the electrodes. As a result, the positively charged Ag ions were attracted by the negatively biased Ag electrode. As the data in figure 5.21 present, a full reversibility of the current flowing between the two electrodes occurs.

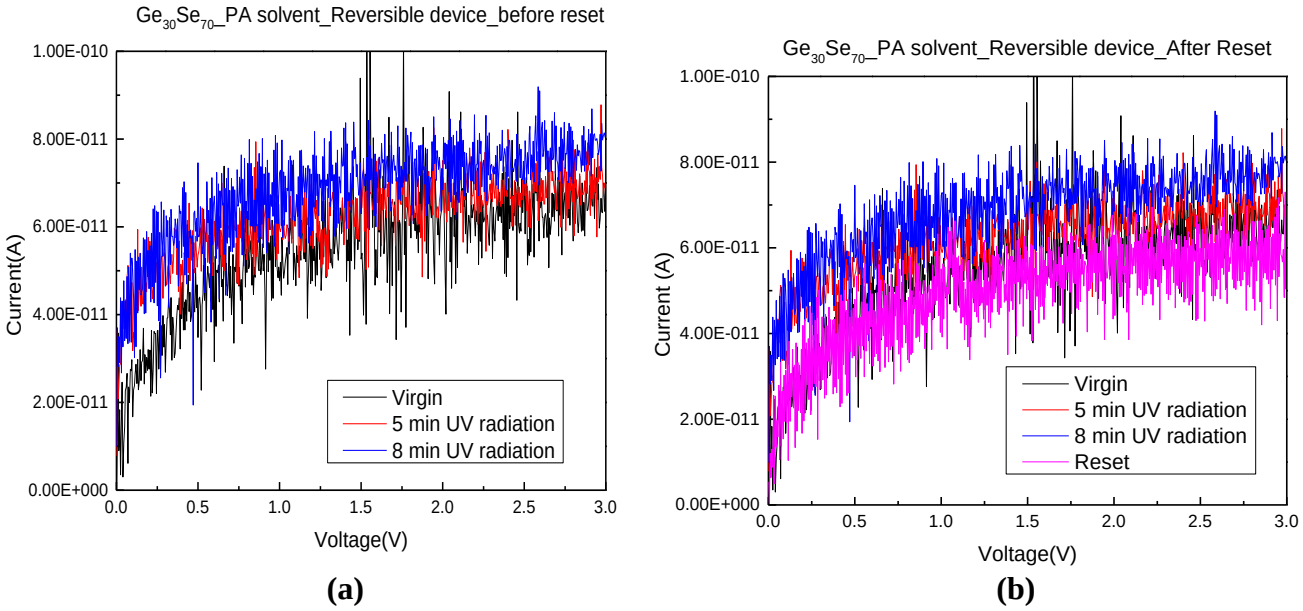

Figure 5.21 Screen printed $Ge_{30}Se_{70}$ (PA solvent) reversible device test at different radiation doses, a) before reset, and b) after reset.

The results presented in this chapter give evidence of the proof of concept for creating radiation sensors based on the electromagnetic waves initiated by Ag diffusion and the effects in the hosting ChG. Each of the individually studied compositions has specifics in their reaction to the irradiation, which was explained, having in mind their structure studied in the previous chapter. The results also give an idea as to which of the studied devices could be most suitable for the fabrication of stable and reliable devices. We recommend for these devices based on Chalcogen rich films and mainly devices based on $Ge_{30}Se_{70}$ films.

CHAPTER 6: FINAL REMARKS & FUTURE WORK

The main goal of this research work to formulate ChG ink by dissolution in Amine, design, fabricate, and test the radiation sensing device on a hard or flexible substrate using additive manufacturing technology has been successfully achieved. While there are some literature sources regarding the dissolution of ChG in different solvents to form a liquid source of Chalcogenide materials, they all were prepared for the spin-coating of the solutions [11-18]. It means that they did not have the specific properties required for ink printing, applying the additive technology. For devices, there are existing data giving proof of the concept of building radiation sensors based on ChG and applying the Ag diffusion as a driving force of device performance [4-8]. However, these devices were fabricated by vacuum deposition of the films which technology has very different specifics, compared to the additive technology, that recently triggered a great interest, due to the many benefits it offers. In view of the status quo, there is a need of research in-depth related to the formation of ink-based on the ChG, printed film analysis, fabrication of the ChG ink printed devices, including the radiation sensing devices and their characterization and testing which all were so far presented in this thesis. The particular results of this research work are summarized below:

1. Three different compositions of the Ge-Se based ChG inks were prepared and successfully printed on both the Si wafers and Kapton substrates, using AM.
    a. Ge-Se based ChG inks were prepared in two ways; such as the dissolution based ink and nanoparticles based ink. For the dissolution based ink, the ChG powder was dissolved into Amine.

b. The inks were characterized by using the viscometer to check the viscosity; the dynamic light scattering (DLS) was used for measuring the particle size, and the tensiometer was used to observe the contact angle of the ink with different substrates. At these studies, particular modifications and combinations of the ink components have been done in order to obtain a medium, which is suitable for application with the particular printers.

c. After the vacuum filtration process, the inks based on dissolution in Amines were deposited on the substrate using the screen printing method. The printed films were sintered following two steps. In the first step, the solvent was evaporated, and in the following step, due to the annealing, the printed particles agglomerated to create solid films.

d. For the nanoparticles based ink, the ChG powder was wet-milled with the solvent and surfactant using the ball milling process to get the nanostructure of the ChG. Then, the vibration energy was transferred to the stock solution using an ultrasonicator to get the desired particle size. Sometimes, the centrifuge was used to obtain uniform particle size. The DMP-2800 inkjet printer was used to print on the substrate. The parameters of the printer were optimized before printing in order to achieve a printed pattern with a good resolution. After the printing process, the printed film was sintered in the Ar filled chamber following two steps similar to the dissolution based ink printed film.

2. A comprehensive study of the Ge-Se based ChG printed film analysis was conducted. The main reason for this study was to understand the radiation effect on the printed films at room temperature. The structural and materials characterization, surface roughness, oxidation, and UV light radiation-induced effect on both types of the printed films were analyzed and studied with the aid of different characterization methods such as energy-dispersive X-ray spectroscopy (EDS), scanning electron microscopy (SEM), atomic force microscopy (AFM), and Raman spectroscopy.
    a. EDS analysis of the dissolution based printed films revealed ~5-6% compositional variance after the sintering process due to the complex chemical reactions with solvent during the dissolution process. On the other hand, the nanoparticles based printed films showed ~1% variance for the Ge rich composition. For Se rich composition, the variation was 8-9% because of the presence of Se wrong bonds, Se-Se chains, and rings, which were evaporated during the sintering process. The EDS study also revealed that irradiated printed films have very negligible compositional differences in comparison with the non-irradiated printed film. EDS study also revealed that the initial radiation dose created dangling bonds. These dangling bonds influenced the oxidation of printed films.
    b. An increase in the average surface roughness was observed of the printed films with a higher UV light radiation dose. The electron-hole pair generation rate was proportional to the higher UV light radiation

doses, which were partially responsible for increasing the surface roughness. However, for dissolution based printed films, the surface also became rough because of the screen that was used for the screen printing process.

c. The Raman spectroscopy data illustrated that there were no significant structural changes observed due to UV light radiation doses in the structure of the Se rich nanoparticles printed films. Only the Ge rich composition printed films ($Ge_{40}Se_{60}$) showed structural changes due to dissociation of the Ge-Ge bonds and following this restructuring and oxidation. On the other hand, for the dissolution based printed films, the Raman data showed significant structural changes and proved the existence of residual materials in the printed films.

3. Printed radiation sensor devices were designed, fabricated, tested under the UV light radiation using two different types of the ChG inks. All the devices were tested in the same conditions and room temperature.

    a. The screen-printed radiation sensing devices were fabricated with three different compositions of the ChG. For both solvent fabricated devices, the performance of the $Ge_{30}Se_{70}$ composition device presented a four order magnitude increase in the conductivity.

    b. For the PA solvent screen printed $Ge_{20}Se_{80}$ device, conductivity increased after an initial radiation dose of the UV light radiation. Further exposure of the UV light radiation dose did not change the current flowing through the devices due to the very fast recombination

of the electron-hole pairs, which were generated during the irradiation process. The $Ge_{20}Se_{80}$ composition has excess Se wrong bonds, which speeded up the recombination of the electron-hole pairs. This is not the case for the $Ge_{30}Se_{70}$ composition, which is very close to the stoichiometric composition and does not have excess Se wrong bonds.

c. Due to the presence of the residual materials in the EDA fabricated $Ge_{20}Se_{80}$ composition device, the current flowing through the devices decreased after the UV light exposure.

d. The conductivity of both screen-printed $Ge_{40}Se_{60}$ devices was constant due to the lack of the Se-Se wrong bonds in that particular composition.

e. In comparison with the $Ge_{30}Se_{70}$ screen-printed device, the nanoparticles devices had a wide range of sensing capabilities. They showed 11 orders of magnitude increase of conductivity due to better sintering conditions at a similar thickness of the ChG printed layers of dissolution based devices.

f. The $Ge_{30}Se_{80}$ & $Ge_{40}Se_{60}$ screen printed and nanoparticles based device showed similar characteristics and results.

g. The XRD data provedthe Ag diffusion by revealing the formation of binary (α-Ag_2Se) and ternary (Ag_8GeSe_6) in both types of printed devices. The intensity and hence crystals sizes changes of these byproducts with different radiation doses reflected the conductivity changes in the devices.

h. The EDS data also proved the Ag diffusion by showing a line scan between the two Ag electrodes of the studied devices. For screen-printed devices, the atomic percentage of the Ge and Se was lower than its bulk ChG composition due to the complex chemical reactions with Amine. On the other hand, for the nanoparticles based devices, the atomic percentage of the Ge and Se did not show any differences compared to its bulk composition.

i. The $Ge_{30}Se_{70}$ nanoparticles-based devices were also tested under the Xe^{+} ion radiation source, and their IV characteristics showed conductivity increment due to the radiation doses increase.

j. The $Ge_{30}Se_{70}$ screen-printed reversible radiation sensing device was fabricated, tested, and reset under the UV light radiation.

In summary, based on our findings, we suggest that the $Ge_{30}Se_{70}$ nanoparticles-based devices and the PA solvent $Ge_{30}Se_{70}$ screen printed devices are the best compositions for radiation sensing devices. One further development of this research could be related to the fabrication of non-volatile memory devices, temperature sensors, NO_2 gas sensors, and others, applying the nanoparticles, and dissolution based ChG inks. These inks can be modified for use with any other printers to make new devices. The performance of the dissolution based ink can be improved by suitable sintering conditions. The overall goal of this research is to fabricate radiation sensor at low cost without any expensive and heavy equipment has been achieved, and this technology for devices fabrication can be applied for example in the international space station to support the space exploration.

REFERENCES

[1] Y. Gonzalez-Velo, H.J. Barnaby, M.N. Kozicki, P. Dandamudi, A. Chandran, K.E. Holbert, M. Mitkova, M. Ailavajhala, "Total-ionizing-dose effects on the resistance switching characteristics of chalcogenide programmable metallization cells," *IEEE Transactions on Nuclear Science*, vol. 60, no. 6, pp. 4563-4569, Dec 2013.

[2] S. Kumar, V. Pavelyev, P. Mishra, N. Tripathi, "A review on 2D transition metal di-chalcogenides and metal oxide nanostructures based NO_2 gas sensors," *Materials Science in Semiconductor Processing*, vol. 107, pp. 104865-104887, Mar 2020.

[3] M. S. Ailavajhala, "Nano-ionic radiation sensor: materials engineering, device design, and testing," Ph.D. dissertation, Dept. Elect. Eng., Boise State Univ., Boise, ID, USA, 2014.

[4] Y. Gonzalez-Velo, H.J. Barnaby, A. Chandran, D.R. Oleksy, P. Dandamudi, M.N. Kozicki, K.E. Holbert, M. Mitkova, M. Ailavajhala, P. Chen, "Effects of cobalt-60 gamma-rays on Ge-Se chalcogenide glasses and Ag/Ge-Se test structures," *IEEE Transactions on Nuclear Science*, vol 59, no. 6, pp. 3093-3100, Dec 2012.

[5] P. Dandamudi, M.N. Kozicki, H.J. Barnaby, Y. Gonzalez-Velo, M. Mitkova, K. Holbert, M Ailavajhala, W. Yu, "Sensors based on radiation-induced diffusion of silver in germanium selenide glasses," *IEEE Transactions on Nuclear Science*, vol. 60, no. 6, pp. 4257-4264, Nov 2013.

[6] Y. Sakaguchi, H. Asaoka, Y. Uozumi, Y. Kawakita, T. Ito, M. Kubota, D. Yamazaki, K. Soyama, M. Ailavajhala, M.R. Latif, M. Mitkova, "Studies of silver photodiffusion dynamics in Ag/GexS1−x (x = 0.2 and 0.4) films using neutron reflectometry," *Canadian Journal of Physics*, vol. 92, no. 7/8, pp. 654-658, 2014.

[7] M.S. Ailavajhala, Y. Gonzalez-Velo, C.D. Poweleit, H.J. Barnaby, M.N. Kozicki, D.P. Butt, M. Mitkova, "New functionality of chalcogenide glasses for radiation

sensing of nuclear wastes," *Journal hazardous materials*, vol. 269, no. 3, pp. 68-73, Mar 2014.

[8] M. S. Ailavajhala, Y. Gonzalez-Velo, C. Poweleit, H. Barnaby, M. N Kozicki, K. Holbert, D. P Butt, M. Mitkova, "Gamma radiation-induced effects in floppy and rigid Ge-containing chalcogenide thin films," *Journal of Applied Physics*, vol. 115, no. 4, pp. 0435021-0435029, Jan 2014.

[9] V. Singh, "Chalcogenide glass materials for integrated infrared photonics," Ph.D. dissertation, Dept. Mat. Sci. Eng., Massachusetts Institute of tech., Boston, MA, USA, 2015.

[10] D. Estrada, "Space-Grade Flexible Hybrid Electronics," Epscor research proposal 2017, ID - 17-EPSCoRProp-0053.

[11] G. C. Chern and I. Lauks, "Spin-coated amorphous-chalcogenide films," *Journal of Applied Physics*, vol. 53, no. 10, pp. 6979-6982, Jun 1982.

[12] G. C. Chern, I. Lauks, and A. R. McGhie, "Spin coated amorphous chalcogenide films: Thermal properties," *Journal of Applied Physics*, vol. 54, no. 8, pp. 4596-4601, Aug 1983.

[13] G. C. Chern and I. Lauks, "Spin coated amorphous chalcogenide films: Structural characterization," *Journal of Applied Physics*, vol. 54, no. 5, pp. 2701-2705, May 1983.

[14] Y. Zha, M. Waldmann, and C. B. Arnold, "A review on solution processing of chalcogenide glasses for optical components," *Optical Materials Express*, vol. 3, no. 9, pp. 1259-1272, Sep 2013.

[15] T. Kohoutek, T. Wagner, M. Frumar, A. Chrissanthopoulos, O. Kostadinova, and S. N. Yannopoulos, "Effect of cluster size of chalcogenide glass nanocolloidal solutions on the surface morphology of spin-coated amorphous films," *Journal of Applied Physics*, vol. 103, no. 6, pp. 063511-063516, Mar 2008.

[16] T. A. Guiton and C. G. Pantano, "Sol-to-Gel and Gel-to-Glass Transitions in the As_2S_3-Amine system," *MRS Proceedings*, vol. 121, pp. 509–514, 1988.

[17] T. A. Guiton and C. G. Pantano, “Solution/gelation of arsenic trisulfide in amine solvents,” *Chemistry of Materials*, vol. 1, no. 5, pp. 558–563, Sep 1989.

[18] S.R. Elliot, “Physics of Amorphous Materials.” Essex: Longman,1990.

[19] Bekir KARASU, Tuğçegül İDİNAK, Eda ERKOL, Ali Ozan YANAR, “Chalcogenide Glasses,” *El-Cezerî Journal of Science and Engineering* ,vol. 6, no. 3, pp. 428-457, 2019.

[20] https://en.wikipedia.org/wiki/Metalloid

[21] M. Mitkova, “Chalcogenide Glass Radiation Sensor; Materials Development, Design and Device Testing,” technical POC, project 09-837.

[22] G. Lucovsky, “Average energy gaps in the binary glass-alloy systems: $Ge_{1-x}Se_x$ and $As_{1x}Se_x$,” *Physical Review B*, vol. 15, p. 5762, 1977.

[23] V. Kumar, S. Kr Sharma, T. Sharma, and V. Singh, “Bandgap determination in thick films from reflectance measurements,” *Optical Materials*, vol. 12, pp. 115-119, 1999.

[24] A. Lakatos and M. Abkowitz, “Electrical Properties of Amorphous Se, As_2Se_3, and As_2S_3,” *Physical Review B*, vol. 3, p. 1791, 1971.

[25] S. R. Elliott and A. Zakery, “An Introduction to Chalcogenide Glasses,” in *Optical Nonlinearities in Chalcogenide Glasses and their Applications*, vol. 135, ed: Springer Berlin Heidelberg, 2007, pp. 1-28.

[26] https://www.doitpoms.ac.uk/tlplib/atomic-scale-structure/intro.php

[27] Y. Sakaguchi, D. A. Tenne, and M. Mitkova, “Structural development in Ge-rich Ge-S glasses,” *Journal of Non-Crystalline Solids* vol. 355, pp. 1792-1796, 2009.

[28] https://en.wikipedia.org/wiki/Allotropes_of_sulfur

[29] K. Gupta and S. Das, “X-ray study of selenium in the liquid and colloidal state,” *Indian Journal of Physics*, vol. 15, pp. 401-409, 1941.

[30] J. Stuke, “Review of optical and electrical properties of amorphous semiconductors,” *Journal of Non-Crystalline Solids*, vol. 4, pp. 1-26, 1970.

[31] M.T. Kostyshin, E.V. Mikhailovskaya and P.F. Romanenko, "Photographic sensitivity effect in thin semiconducting films on metal substrates," *Sov. Phys. Solid State*, vol. 8, pp. 451–452, 1966.

[32] M.N. Kozicki, M. Park, M. Mitkova, "Nanoscale Memory Elements Based on Solid-State Electrolytes," *IEEE Transaction on Nanotechnology*, vol. 4,p. 331-338, 2005.

[33] M. Mitkova, I. Iliev, V. Boev, T. Petkova, "Influence of an Electrical Field on Optical Recording in Chalco-halide Glasses," *J. Non-Cryst. Sol.*, vol. 227, p. 748-75*1*, 1998.

[34] M. Mitkova, T.Petkova, V.Mateev, Pl.Markovsky, " Photoinduced changes in the Se-Ag-I system," *J. Phys. Chem.*, vol. 96,p. 8998-9001, *July* 1992.

[35] M. Frumar, T.Wagner, "Ag-doped chalcogenide glasses and their applications," *Current Opinion in Solid State and Materials Science*, vol. 7, pp. 117–126, 2003.

[36] R. E. Ghrandi, J. Calas, G. Galibe, "Ag dissolution kinetics in amorphous $GeSe_{5.5}$ thin films from In-situ resistance measurements versus time," *Physica Solidi*, vol. 123, pp. 451-460, 1991.

[37] J.C.Phillips"Microscopic origin of anomalously narrow Raman lines in network glasses," Journal of Non-Crystalline Solids, vol. 63, no. 3, pp 347-355, 1984.

[38] I. Abdulhalim, M. Gelbaor, M. Klebanov, and V. Lyubin, "Photoinduced phenomena in nano-dimensional glassy As_2S_3 films," *Physica staus solidi*, vol. 356, pp.-147-152, 2010.

[39] D.Tsiulyanu and I. Stratan, "on the photodisslution kinetics of silver in glassy As_2S_3," *Journal of Non-crystalline solids*, vol. 356, pp.-147-152, 2010.

[40] T. Wagner, "Photo-And Thermally-Induced Diffusion And Dissolution of Ag In Chalcogenide Glasses Thin Films," *Journal of Optoelectronics and Advanced Materials*, Vol. 4, No. 3, pp. 717 – 727, 2002.

[41] M. Mitkova, M. Kozicki, H. Kim, and T. Alford, "Local structure resulting from photo and thermal diffusion of Ag in Ge–Se thin films," *Journal of Non-Crystalline Solids*, vol. 338, pp. 552-556, 2004.

[42] T. W. Kang, C. Y. Hong, C. S. Chong, and T. W. Kim, "Effects of electric fields on the silver photodoping of As_2Se_3 films," *Journal of Materials Science*, vol. 27, pp. 5620-5622, 1992.

[43] V. Kornelyuk, I. Savitskii, L. Khirunenko, O. Shpotyuk, and I. Yaskovets, "Photoinduced defect formation in chalcogenide vitreous semiconductors," *Journal of Applied Spectroscopy*, vol. 50, pp. 310-313, 1989.

[44] K. Shahi, "Transport studies on superionic conductors," *Physica Status Solidi (a)*, vol. 41, pp. 11-44, 1977.

[45] S. K. Sundaram, J. S. McCloy, B. J. Riley, M. K. Murphy, H. A. Qiao, C. F. Windisch, E. D. Walter, J. V. Crum, R. Golovchak, and O. Shpotyuk, "Gamma Radiation Effects on Physical, Optical, and Structural Properties of Binary As–S Glasses," *Journal of the American Ceramic Society*, vol. 95, pp. 1048-1055, 2012.

[46] A. Kovalskiy, "Compositional trends of radiation-induced effects in ternary systems of chalcogenide glasses," *Radiation Effects and Defects in Solids*, 158, vol. 1, pp. 391-397, 2003.

[47] O. Shpotyuk, R. Y. Golovchak, T. Kavetsky, A. Kovalskiy, and M. Vakiv, "Radiation–optical effects in glassy Ge–As (Sb)–S systems," *Nuclear Instruments and Methods in Physics Research Section B: Beam Interactions with Materials and Atoms*, vol. 166, pp. 517-520, 2000.

[48] O. I. Shpotyuk, "Radiation-induced effects in chalcogenide vitreous semiconductors," *Semiconductors and Semimetals*, vol. 78, pp. 215-260, 2004.

[49] M. Mitkova, T. Petkova, P. Markovski, and V. Mateev, "Photoinduced changes by polarisation holographic recording in $Se_{70}Ag_{15}I_{15}$ thin films," *Journal of noncrystallinesolids*, vol. 164, pp. 1203-1206, 1993.

[50] M. Mitkova, M.N. Kozick, "Ag-photodoping in Ge-chalcogenide amorphous thin films—Reaction products and their characterization," *Journal of Physics and Chemistry of Solids*, vol. 68, pp.866–872, 2007.

[51] M. Ribes, E. Bychkov, and A. Pradel, "Ion transport in chalcogenide glasses: Dynamics and structural studies," *Journal of Optoelectronics and Advanced Materials*, vol. 3, no. 3, pp. 665-674, Sep 2001.

[52] M. Ureña, A. Piarristeguy, M. Fontana, and B. Arcondo, "Ionic conductivity (Ag^+) in AgGeSe glasses," *Solid State Ionics,* vol. 176, pp. 505-512, 2005.

[53] Y.R. Luo and J.A. Kerr, "Bond dissociation energies," in *CRC Handbook of Chemistry and Physics*, Boca Raton, FL, USA: CRC Press, pp. 65-98, 2012.

[54] A.V. Kolobov, K.Tanaka, "Photoinduced phenomena in amorphous chalcogenides: from phenomenology to nanoscale," in *Handbook of Advanced Electronic and Photonic Materials and Devices*, H.S. Nalwa, Newyork, USA: Academic Press, 2001, vol. 5, pp. 47-90.

[55] T. Kawaguchi, K. Tanaka, SR Elliott, "Photoinduced and electron beam phenomena in Ag-rich amorphous chalcogenide semiconductors," in *Handbook of Advanced Electronic and Photonic Materials and Devices,* H.S. Nalwa, Newyork, USA: Academic Press, 2001, vol. 5, pp. 91-117.

[56] M.A. Popescu, "Non-crystalline chalcogenides," Newyork, USA: Kluwer academic publishers, 2002.

[57] Y. Zha, "Solution-processing of Chalcogenide Materials for Device Applications," Ph.D. dissertation, Dept. Elect. Eng., Princeton Univ., Princeton, NJ, USA, 2014.

[58] https://en.wikipedia.org/wiki/Chelation

[59] S. Mamedov, "On the macromolecular mechanism of dissolution of As_2S_3 films in organic solutions," *Thin Solid Films***,** vol.226, no. 2, pp. 215–218, 1993.

[60] S. A. Zenkin, S. B. Mamedov, M. D. Mikhailov, E. Y. Turkina, and I. Y. Yusupov, "Mechanism for interaction of amine solutions with monolithic glasses and amorphous films in the As-S system," *Glass Phys. Chem.*, vol.23, pp. 393–399, 1997.

[61] S. Song, S. S. Howard, Z. Liu, A. O. Dirisu, C. F. Gmachl, and C. B. Arnoldb, "Mode tuning of quantum cascade lasers through optical processing of chalcogenide glass claddings," *Applied Physics Letters*, vol. 89, no. 4, pp. 115-117, Jun 2006.

[62] S. Slanga, K. Palkaa,b, M. Vlcek, "Thermal dependence of photo-induced effects in spin-coated $As_{20}Ge_{12.5}S_{67.5}$ thin films," *Journal of Non-Crystalline Solids*, vol. 471, no. 3, pp.415-420, 2017.

[63] Y. Zha and C. B. Arnold, "Solution-processing of thick chalcogenide and metal chalcogenide structures by spin-coating and multilayer lamination," *Optical Materials Express*, Vol. 3, no. 2, pp. 309-317, Feb 2013.

[64] S. Slang, L. Loghina, K. Palka, and M. Vlceka, "Exposure enhanced photoluminescence of $CdS_{0.9}Se_{0.1}$ quantum dots embedded in spin-coated $Ge_{25}S_{75}$ thin films," *RSC Adv.*, vol. 7, pp 53830-53838, Nov 2017.

[65] H.W. Tan, T. Tran, C.K. Chua, "A review of printed passive electronic components through fully additive manufacturing methods," *J. Virtual and Physical Prototyping*, vol. 11, no. 4, pp.271-288, Aug. 2016.

[66] R. Singh, E. Singh, H. S. Nalwa, "Inkjet-printed nanomaterial-based flexible radio frequency identification (RFID) tag sensors for the internet of nano things," *RSC Adv.*, vol. 7, no.77, pp. 48597-48630, Jul. 2017.

[67] W. Wu, "Inorganic nanomaterials for printed electronics: a review,"*Nanoscale*, vol. 9, no. 22, pp. 7342-7372, May 2017.

[68] A. Feltz, *Amorphous Inorganic Materials, and Glasses*. New York, USA: VCH Publishers, 1993.

[69] R. Fairman and B. Ushkov, "*Semiconducting chalcogenide glass*," Amsterdam; London, Elsevier Academic Press, 2004.

[70] P. Janicek, S. Slang, K. Palka, and M. Vlcek, "Spectroscopic ellipsometry characterization of spin-coated $Ge_{25}S_{75}$ chalcogenide thin films," *Pure Appl. Chem.*, vol. 89, no. 4, pp.437-449, Jan 2017.

[71] P. Janicek, S. Slang, K. Palka, and M. Vlcek, "Structure and properties of spin-coated $Ge_{25}S_{75}$ chalcogenide thin films," *Opt. Mater. Express*, vol. 6, no. 6, pp.1973-1985, Jan 2017.

[72] https://www.ossila.com/pages/contact-angle-theory-measurement

[73] R. F. Egerton, "*Physical principles of electron microscopy: an introduction to TEM, SEM, and AFM,*" Boston, MA, Springer, 2005.

[74] L.Reimer, "*Scanning electron microscopy: physics of image formation and microanalysis*," Newyork city, NY, Springer, 1998.

[75] K. Tanaka, Y. Kasanuki, and A. Odajima, "Physical properties and photoinduced changes of amorphous Ge-S films," *Thin Solid Films,* vol. 117, pp. 251-260,1984.

[76] M. Mitkova, A. Kovalskiy, H. Jain, Y. Sakaguchi, "Effect of photo-oxidation on the photodiffusion of silver in germanium chalcogenide glasses," *Journal of Optoelectronics and Advanced Materials,* Vol. 11, No. 12, pp. 1899-1906, Dec 2009.

[77] Y. Sakaguchi, D. Tenne, M. Mitkova, "Oxygen-assisted photoinduced structural transformation in amorphous Ge-S films," *Phys. Status Solidi* B, vol. 246, no. 8, pp. 1813-1819, 2009.

[78] C.V. Raman & K. S. Krishnan, "A New Type of Secondary Radiation," *Nature,* vol. 121, pp. 501-502, Mar 1928.

[79] Smith & G. Dent, "Modern Raman Spectroscopy: A Practical Approach," 1st ed., Wiley, Chichester, United Kingdom, 2005.

[80] https://www.edinst.com/blog/what-is-raman-spectroscopy/

[81] M. S. Ailavajhala, T. Nichol, Y. Gonzalez-Velo, C. Poweleit, H. Barnaby, M. N Kozicki, D. P Butt, and M. Mitkova, "Thin Ge–Se films as a sensing material for radiation doses," *Phys. Status Solidi B,* vol. 251, pp. 1347–1353, Dec 2013.